# Simulation of Nonadiabatic Dynamics and Time-Resolved Photoelectron Spectra in the Frame of Time-Dependent Density Functional Theory

DISSERTATION

zur Erlangung des akademischen Grades

Dr. Rer. Nat.
im Fach Chemie

eingereicht an der
Mathematisch-Naturwissenschaftlichen Fakultät I
Humboldt-Universität zu Berlin

von

**Diplom-Chemikerin Ute Werner**
geboren am 15.07.1980 in Berlin

Präsident der Humboldt-Universität zu Berlin:
Prof. Dr. Jan-Hendrik Olbertz

Dekan der Mathematisch-Naturwissenschaftlichen Fakultät I:
Prof. Dr. Andreas Herrmann

Gutachter:
1. Prof. Dr. V. Bonačić-Koutecký
2. Prof. Dr. J. Michl
3. Prof. Dr. P. Fantucci

**eingereicht am:** 17.05.2011
**Tag der mündlichen Prüfung:** 22.06.2011

# Acknowledgment

This thesis would not have been possible without the help of many people, to whom I owe my deepest gratitude.

Above all, I want to express my sincere gratitude to my supervisor Prof. Vlasta Bonačić-Koutecký for giving me the opportunity to realize this thesis in her group. I wish to thank her for her inestimable support and guidance. Moreover, I am grateful for the opportunity of interacting with many excellent scientists in the field of physical chemistry.

I appreciated the fruitful cooperation with the experimental group of Prof. Toshinori Suzuki.

I owe my deepest gratitude to Dr. Roland Mitrić, without whose assistance and scientific support this thesis would not have come into existence. I am indebted to former and current group members, in particular Christian Bürgel, Jens Petersen, Alexander Kulesza, and Melanie Nößler, for being wonderful colleagues. I also want to extend my thanks to Bernd Böttcher and Katharina Pfaff for their technical and administrative support. I particularly wish to thank Katharina Fischer, Dirk Broßke, Ramona Kositzki, and Joshua J. Melko for the proofreading of this thesis.

Financial support by the Graduiertenkolleg 1025 “Grundlagen und Funktionalität von größen- und grenzflächenbestimmten Materialien”, Deutsche Forschungsgemeinschaft (DFG) Sonderforschungsbereich 450 “Analyse und Steuerung ultraschneller photoinduzierter Reaktionen”, and the DFG priority program 1391 “Ultrafast Nanooptics” are gratefully acknowledged.

Finally, I wish to thank my friends, family, and especially Dirk Broßke for always being there when I needed them.

# Abstract

The goal of this thesis was the development of a generally applicable theoretical framework for the simulation of ultrafast processes and experimental observables in complex molecular systems. For this purpose, a combination of the time-dependent density functional theory (TDDFT) for the description of the electronic structure with the Tully's surface hopping procedure for the treatment of nonadiabatic nuclear dynamics based on classical trajectories was employed. In particular, a new approach for the calculation of nonadiabatic couplings within TDDFT was devised. The method was advanced for the description of more complex systems such as chromophores in a solvation shell by employing the tight binding approximation to TDDFT.

Since the time-resolved photoelectron spectroscopy (TRPES) represents a powerful experimental technique for real-time observation of ultrafast processes, a TDDFT based approach for the simulation of TRPES was developed. The basic idea is the approximate representation of the combined system of cation and photoelectron by excited states of the neutral species above the ionization threshold. In order to calculate these states with TDDFT, a formulation of the transition dipole moments between excited states within TDDFT was devised. Moreover, simulations employing the Stieltjes imaging (SI) procedure were carried out providing the possibility to reconstruct photoelectron spectra from spectral moments. In this work, the spectral moments were calculated from discrete TDDFT states.

The scope of the developed theoretical methods was illustrated on the photoisomerization in benzylideneaniline as well as on the ultrafast photodynamics in furan, pyrazine, and microsolvated adenine. The examples demonstrate that the nonadiabatic dynamics simulations based on TDDFT and TDDFTB are particularly suitable for the investigation and interpretation of ultrafast photoinduced processes in complex molecules.

# Zusammenfassung

Ziel dieser Arbeit war die Entwicklung einer allgemein anwendbaren Methode für die Simulation von ultraschnellen Prozessen und experimentellen Observablen. Hierfür wurden die Berechnung der elektronischen Struktur mit der zeitabhängigen Dichtefunktionaltheorie (TDDFT) und das Tully-Surface-Hopping-Verfahren für die nichtadiabatische Kerndynamik auf der Basis klassischer Trajektorien miteinander kombiniert. Insbesondere wurde eine Beschreibung der nichtadiabatischen Kopplungen für TDDFT entwickelt. Diese Methode wurde für die Simulation noch komplexerer Systeme durch die Tight-Binding-Näherung für TDDFT erweitert.

Da die zeitaufgelöste Photoelektronenspektroskopie (TRPES) ein exzellentes experimentelles Verfahren für die Echtzeitbeobachtung von ultraschnellen Prozessen darstellt, wurde eine TDDFT-basierte Methode für die Simulation von TRPES entwickelt. Der Methode liegt die Idee zu Grunde, das System aus Kation und Photoelektron näherungsweise durch angeregte Zustände des neutralen Moleküls oberhalb der Ionisierungsgrenze zu beschreiben. Um diese Zustände mit TDDFT berechnen zu können wurde eine Beschreibung der Übergangsdipolmomente zwischen angeregten TDDFT-Zuständen entwickelt. Des Weiteren wurden Simulationen im Rahmen des Stieltjes-Imaging-Verfahrens, das eine Möglichkeit der Rekonstruktion des Photoelektronenspektrums aus den spektralen Momenten bietet, durchgeführt. Diese spektralen Momente wurden aus den diskreten TDDFT-Zuständen berechnet.

Die breite Anwendbarkeit der entwickelten theoretischen Methoden für die Simulation von komplexen Systemen wurde an der Photoisomerisierung in Benzylidenanilin sowie der ultraschnellen Photodynamik in Furan, Pyrazin und mikrosolvatisiertem Adenin illustriert. Die dargestellten Beispiele demonstrieren, dass die nichtadiabatische Dynamik im Rahmen von TDDFT bzw. TDDFTB sehr gut für die Untersuchung und Interpretation der ultraschnellen photoinduzierten Prozesse in komplexen Molekülen geeignet ist.

# Contents

**List of Figures** viii

**List of Tables** x

**Introduction** 1

**I Methodology** 6

**1 Computational Methods for Structures and Electronic States** 7
- 1.1 Density Functional Theory 7
  - 1.1.1 Limitations of DFT 8
- 1.2 Time-Dependent Density Functional Theory 9
  - 1.2.1 Limitations of TDDFT 10
  - 1.2.2 Charge-Transfer Excited States in TDDFT 11
- 1.3 Density Functional Tight Binding 12
  - 1.3.1 Limitations of DFTB 14
- 1.4 Time-Dependent Density Functional Tight Binding 15
  - 1.4.1 Limitations of TDDFTB 16

**2 Simulation of Nonadiabatic Dynamics** 17
- 2.1 Introduction 17
- 2.2 Semiclassical Dynamics and Tully's Surface Hopping Procedure 17
  - 2.2.1 Born-Oppenheimer Approximation 18
  - 2.2.2 Semiclassical Dynamics 20
  - 2.2.3 Tully's Surface Hopping Procedure 20
  - 2.2.4 Electronic Structure Calculations for Semiclassical Dynamics 23
- 2.3 Development of Nonadiabatic Dynamics in the Frame of TDDFT 24
  - 2.3.1 Representation of the Wavefunction within LR-TDDFT 24
  - 2.3.2 Nonadiabatic Couplings for LR-TDDFT 26
  - 2.3.3 Nonadiabatic Couplings for TDDFTB 27
- 2.4 Details of the Implementation 28
  - 2.4.1 Initial Conditions for the Nonadiabatic Dynamics 28
  - 2.4.2 Propagation of the Classical Trajectories 29
  - 2.4.3 Hopping Procedure 29
  - 2.4.4 Implementation of Nonadiabatic Couplings 32

2.4.5 Test on the Photodynamics of $CH_2NH_2^+$ . . . . . . . . . . . . . . . 33

**3 Simulation of Ultrafast Observables: Time-Resolved Photoelectron Spectra 36**
3.1 Introduction . . . . . . . . . . . . . . . . . . . . . . . . . . . . . . . . . . . . . 36
3.2 Derivation of an Expression for the Simulation of TRPES . . . . . . . . . . 38
3.3 Approximate Description of Photoionization Probabilities . . . . . . . . . . 41
3.3.1 Discretized Description of the Electronic Continuum Based on TDDFT . . . . . . . . . . . . . . . . . . . . . . . . . . . . . . . . . 42
3.3.2 Stieltjes Imaging Procedure . . . . . . . . . . . . . . . . . . . . . . . . 43
3.3.3 Implementation and Tests of the Stieltjes Imaging Procedure . . . 45

**II Applications 48**

**Introduction 49**

**4 Ultrafast Photoisomerization in Benzylideneaniline 50**
4.1 Introduction . . . . . . . . . . . . . . . . . . . . . . . . . . . . . . . . . . . . . 50
4.2 Computational Methods . . . . . . . . . . . . . . . . . . . . . . . . . . . . . 51
4.3 Structural and Electronic Properties . . . . . . . . . . . . . . . . . . . . . . 52
4.4 Nonadiabatic Dynamics . . . . . . . . . . . . . . . . . . . . . . . . . . . . . 54
4.5 Time-Resolved Photoelectron Spectrum . . . . . . . . . . . . . . . . . . . . 59
4.6 Summary . . . . . . . . . . . . . . . . . . . . . . . . . . . . . . . . . . . . . . 62

**5 Ultrafast Photodynamics in Furan 63**
5.1 Introduction . . . . . . . . . . . . . . . . . . . . . . . . . . . . . . . . . . . . . 63
5.2 Computational and Experimental Methods . . . . . . . . . . . . . . . . . . 64
5.3 Electronic Properties . . . . . . . . . . . . . . . . . . . . . . . . . . . . . . . 65
5.4 Nonadiabatic Dynamics . . . . . . . . . . . . . . . . . . . . . . . . . . . . . 67
5.5 Time-Resolved Photoelectron Spectrum . . . . . . . . . . . . . . . . . . . . 72
5.6 Summary . . . . . . . . . . . . . . . . . . . . . . . . . . . . . . . . . . . . . . 77

**6 Internal Conversion in Pyrazine 78**
6.1 Introduction . . . . . . . . . . . . . . . . . . . . . . . . . . . . . . . . . . . . . 78
6.2 Computational and Experimental Methods . . . . . . . . . . . . . . . . . . 79
6.3 Electronic Properties . . . . . . . . . . . . . . . . . . . . . . . . . . . . . . . 81
6.4 Nonadiabatic Dynamics . . . . . . . . . . . . . . . . . . . . . . . . . . . . . 83
6.5 Time-Resolved Photoelectron Spectrum . . . . . . . . . . . . . . . . . . . . 87
6.6 Summary . . . . . . . . . . . . . . . . . . . . . . . . . . . . . . . . . . . . . . 90

**7 Nonadiabatic Dynamics of Isolated and Microsolvated Adenine 92**
7.1 Introduction . . . . . . . . . . . . . . . . . . . . . . . . . . . . . . . . . . . . . 92
7.2 Computational Methods . . . . . . . . . . . . . . . . . . . . . . . . . . . . . 93
7.3 Structural and Electronic Properties of Gas-Phase Adenine . . . . . . . . 94
7.4 Nonadiabatic Dynamics of Gas-Phase Adenine . . . . . . . . . . . . . . . 95

7.5 Microsolvated Adenine . . . . . . . . . . 98
7.6 Summary . . . . . . . . . . 100

**III Summary 102**

**8 Summary and Outlook 103**

**9 Zusammenfassung und Ausblick 106**

**IV Appendix 109**

**Bibliography 110**

**List of Abbreviations 130**

**Publikationsliste – Ute Werner 132**

**Selbständigkeitserklärung 134**

# List of Figures

2.1 Comparison of hopping probabilities for a model potential . . . . . . . . . 31
2.2 Absorption spectrum of $CH_2NH_2^+$ . . . . . . . . . . . . . . . . . . . . . . . . 33
2.3 Time-dependent couplings and $|C_K(t)|^2$ of $CH_2NH_2^+$ . . . . . . . . . . . . 34
2.4 Time-dependent populations of $CH_2NH_2^+$ . . . . . . . . . . . . . . . . . . . 34

3.1 Schematic illustration for TRPES . . . . . . . . . . . . . . . . . . . . . . . . . 37
3.2 Comparison of $f(\varepsilon)$ and $g(\varepsilon)$ for $H^-$ from model system and SI . . . . . . 46
3.3 Comparison of cross sections for benzene from SI, ADC, and experiment . 46

4.1 Equilibrium structures of trans- and cis-BAN . . . . . . . . . . . . . . . . 50
4.2 Stationary absorption spectra of trans- and cis-BAN . . . . . . . . . . . . 53
4.3 Thermally broadened stationary absorption spectrum of trans-BAN . . . 54
4.4 Time-dependent populations of BAN . . . . . . . . . . . . . . . . . . . . . . 55
4.5 Time-dependent angles N=C-$C_{Ph}$, C=N-$C_{Ph}$, and $C_{Ph}$-N=C-$C_{Ph}$ of BAN 56
4.6 Snapshots of the nonadiabatic dynamics of BAN (cis-BAN) . . . . . . . . 57
4.7 Snapshots of the nonadiabatic dynamics of BAN (no isomerization) . . . . 57
4.8 Time-dependent deviation of the normal coordinates of BAN . . . . . . . 58
4.9 Time-dependent ionization energies of BAN . . . . . . . . . . . . . . . . . . 59
4.10 Simulated TRPES spectra of BAN . . . . . . . . . . . . . . . . . . . . . . . . 60
4.11 Time evolution of the C=N, C-$C_{Ph}$, and N-$C_{Ph}$ bond lengths of BAN . . 61

5.1 Equilibrium structure of furan . . . . . . . . . . . . . . . . . . . . . . . . . . 63
5.2 Theoretical and experimental absorption spectra of furan . . . . . . . . . 66
5.3 Time-dependent populations of furan after $S_2$ excitation . . . . . . . . . . 68
5.4 Time-dependent energies of furan along one selected trajectory . . . . . . 68
5.5 Time-dependent populations of furan for two initial distributions . . . . . 69
5.6 Time-dependent C-C and C-O bond lengths of furan . . . . . . . . . . . . 70
5.7 Comparison of TDDFT and EOM-CCSD energies of furan . . . . . . . . . 71
5.8 Schematic representation of the photodynamics in furan . . . . . . . . . . 71
5.9 Time-dependent ionization energies of furan . . . . . . . . . . . . . . . . . 72
5.10 Simulated and experimental TRPES spectra of furan . . . . . . . . . . . . 73
5.11 Slices of TRPES spectra of furan for selected PKEs and selected $t_D$ . . . 74
5.12 Experimental photoelectron images of furan . . . . . . . . . . . . . . . . . 75
5.13 Time-dependent populations of furan after $S_1$ excitation . . . . . . . . . . 76
5.14 Theoretical and experimental total photoelectron signals of furan . . . . . 77

6.1 Equilibrium structure of pyrazine . . . . . . . . . . . . . . . . . . . . . . . . 78

6.2 Comparison of the absorption spectra of pyrazine for two basis sets . . . . 80
6.3 Theoretical and experimental absorption spectra of pyrazine . . . . . . . . 82
6.4 Character of the four lowest excited states of pyrazine . . . . . . . . . . . 82
6.5 Time evolution of the excited state populations of pyrazine . . . . . . . . 84
6.6 Time-dependent $S_2$ populations of pyrazine (TDDFT/QM) . . . . . . . . 84
6.7 Time-dependent energies along one selected trajectory of pyrazine . . . . 85
6.8 Time-dependent oscillator strength of pyrazine . . . . . . . . . . . . . . . . 86
6.9 Time-dependent normal mode displacements of pyrazine . . . . . . . . . . 86
6.10 Comparison of simulated and experimental TRPES spectra of pyrazine . . 87
6.11 Slices of TRPES spectra of pyrazine for selected PKE intervals . . . . . . 88
6.12 Slices of TRPES spectra of pyrazine for selected time delays . . . . . . . . 89

7.1 Structures for the 9H- and 7H-adenine tautomers . . . . . . . . . . . . . . 92
7.2 Absorption spectra of isolated adenine and character of excited states . . 94
7.3 Thermally broadened stationary absorption spectrum of isolated adenine . 96
7.4 Time-dependent populations of isolated adenine . . . . . . . . . . . . . . . 96
7.5 Analysis of one selected trajectory for isolated adenine . . . . . . . . . . . 97
7.6 Structure and spectra of microsolvated adenine . . . . . . . . . . . . . . . 99
7.7 Time-dependent populations of microsolvated adenine . . . . . . . . . . . 100

# List of Tables

4.1 Transition energies of trans-BAN . . . . . . . . . . . . . . . . . . . . . . . . . 54

5.1 Transition energies of furan . . . . . . . . . . . . . . . . . . . . . . . . . . . . 67

6.1 Transition energies of pyrazine . . . . . . . . . . . . . . . . . . . . . . . . . . 83

7.1 Transition energies of isolated adenine . . . . . . . . . . . . . . . . . . . . . . 95

# Introduction

The fate of a molecule after interaction with light is determined by relaxation processes taking place on a femtosecond (fs) timescale. These ultrafast nonradiative processes include phenomena such as internal conversion (IC), isomerization, or proton transfer, which play an important role in organic photochemistry. Moreover, the efficiency of these processes is decisive for the remarkable stability of molecular building blocks of life (such as nucleobases in DNA or aminoacids in proteins) under UV irradiation. Therefore, it represents an important prerequisite for the formation of life on our planet. An essential theoretical concept for the understanding and the description of these processes is conical intersection, whose relevance for organic chemistry was established already in the early days of quantum chemistry [1–6] and which have attracted the interest of many researchers in recent years. [3,4,7–11] The distinctive feature of conical intersections is the strong coupling of nuclear and electronic motion in their vicinity. Such nonadiabatic coupling leads to the breakdown of the Born-Oppenheimer approximation, which is a cornerstone for the application of classical molecular dynamics (MD) simulations.

The exploration of ultrafast phenomena has lead to an enormous progress in both the techniques for experimental time-resolved spectroscopy and the methods for the simulation of ultrafast molecular processes. The development of femtosecond laser techniques for optical spectroscopy, which was pioneered by Zewail [6,12–14] and awarded with the Nobel prize in chemistry in 1999, allows for the real-time observation of dynamics in molecules, clusters, and nanostructures. [15,16] The basic principle of time-resolved spectroscopy relies on a pump-probe configuration, in which a first femtosecond pulse (pump) generates a wavepacket in the electronically excited state. Its time evolution is subsequently monitored by a second time delayed pulse (probe), which induces processes such as absorption, fluorescence, ionization, etc. One of the earliest examples for the application of this technique is the experimental investigation of the photodissociation in NaI by Zewail et al. in 1990. [13] The experiment demonstrates impressively that femtosecond spectroscopy enables the direct visualization of the time evolution of a nuclear wavepacket during photoinduced breaking of a chemical bond. The development of attosecond pulses in recent years even permits the direct observation of processes on the timescale of electron dynamics. [17–20]

The rising complexity of the investigated systems and the processes occurring therein represent a major challenge from a theoretical point of view: On the one hand, methods providing an accurate description of the electronic structure for systems of increasing size are needed, while on the other hand, approaches for the simulation of dynamical processes applicable to complex systems have to be developed. Approaches including the full quantum mechanical (QM) description of the nuclear dynamics depend on precalculated potential energy surfaces (PES), which are employed for the propagation of the nuclear wavepackets and allow for the simulation in diatomics or triatomics with a remarkable accuracy. [21–26] However, due to their tremendous effort, which increases exponentially with the system size, the full QM simulations are limited to very small systems or low dimensional models.

The extremely demanding precalculation of PESs can be avoided by employing the “on the fly” approach for the dynamics simulation utilizing independent classical trajectories. Within this method, the nuclei are described by classical mechanics and the forces governing their dynamics are directly calculated in each simulation time step from the QM electronic structure calculations. This approach was developed by Car and Parrinello for MD simulations in the ground electronic state in the frame of the density functional theory (DFT).[27] A route for the extension of the MD simulations to nonadiabatic dynamics was developed 1971 by Tully and Preston.[28] The idea was to propagate classical trajectories on a single adiabatic surface, and to introduce the nonadiabatic effects by allowing trajectories to switch between the surfaces according to quantum mechanically calculated hopping probabilities. Further advancement of the method resulted in 1990 in the Tully's surface hopping (TSH) procedure,[29–31] which has become the most popular method for the simulation of time-dependent processes in complex systems. A reason for the great success of the TSH approach is the possibility of its combination with the "on the fly" dynamics utilizing the whole spectrum of quantum chemical methods.[10,32–43]

For this purpose, the time-dependent density functional theory (TDDFT) is an especially promising candidate. Despite all drawbacks of commonly employed DFT functionals such as the failure in the description of long-range charge-transfer excited states, transitions with multi-reference character, and dispersion interaction, TDDFT is currently the most generally applicable method for the description of optical properties in a huge variety of systems.[44,45] There has been a number of promising attempts for the improvement of TDDFT, mainly by developing new DFT functionals.[46–52] In particular, the description of charge-transfer excited states has been improved by introducing corrections for the wrong asymptotic behavior of DFT.[47,53–55] A promising route for the extension of the method to even more complex systems (e.g. proteins in solution) is provided by the tight binding approximation to TDDFT, called TDDFTB.[56–62]

One focus of this thesis was to combine the efficiency of the TSH procedure with the TDDFT and TDDFTB methods. For this purpose, the nonadiabatic couplings between excited states had to be derived, since they are not available in standard TDDFT(B) program packages.[39,40,63]

The capability of describing both the electronic structure and the dynamical evolution of complex systems also opens the route to the simulation of ultrafast observables and direct comparison with experiment. A particularly suitable experimental technique for the investigation of ultrafast nonadiabatic processes is the time-resolved photoelectron spectroscopy (TRPES).[16,64–69] This methods allows for observing the time evolution of the electronic configuration and the excited state vibrational dynamics simultaneously. Therefore, TRPES has gained enormous significance in recent years and was successfully applied for the investigation of ultrafast relaxation processes in numerous systems.[70–83]

In general, the interpretation of the TRPES spectra is not possible exclusively based on experimental results, thus requiring the close collaboration with theory. However, the simulation of time-dependent photoionization processes represents a serious challenge from a theoretical point of view, since in addition to electronic structure and nuclear dynamics, the ionization continuum has to be accounted for. The usual approaches employing scattering states for the representation of the free electron are extremely demanding and thus have been realized only for very small systems so far. Therefore, a method for the description of photoionization processes based on the discretized representation of the ionization continuum has been developed in this thesis.[84] The basic idea of this approach is to approximate the combined system consisting of the cation and the free electron by neutral excited states obtained from TDDFT above the ionization threshold. These discrete states can be utilized as an approximation for the photoelectron spectrum. Moreover, simulations in the frame of the Stieltjes imaging (SI) procedure have been performed. Within this method, the photoionization spectrum is reconstructed from so-called spectral moments, which can be calculated from any discrete representation of the photoelectron spectrum. In this work, discrete TDDFT states were employed. The SI procedure is particularly useful if the spectral moments can be calculated without diagonalization of the full Hamilton matrix. The TDDFT based approach for the description of the ionization can be easily combined with the TDDFT based nonadiabatic dynamics, thus allowing for the simulation of TRPES spectra in complex systems.[84,85]

The methodological development within this work was applied to a series of systems with increasing complexity, leading to new insights into the mechanisms of ultrafast nonadiabatic processes.

The thesis is structured as follows: In Part I, the development of an approach for the simulation of nonadiabatic dynamics and TRPES in the frame of TDDFT as well as the extension to TDDFTB are presented. The fundamentals of the density functional theory needed for this work are outlined in Chapter 1. The approach for the nonadiabatic dynamics both in the frame of TDDFT employing localized atomic Gaussian basis sets and based on TDDFTB are presented in Chapter 2. The approach for the simulation of the ultrafast observable TRPES, which is based on the discretized representation of the ionization continuum, is provided in Chapter 3. The combination of this method with the Stieltjes imaging procedure is presented in the same Chapter.

In Part II, the application of the methodological development is presented. The scope of the methods for the treatment of complex molecular systems is demonstrated in Chapter 4 by the example of benzylideneaniline (BAN), which represents a prototype for a molecular photoswitch.[40] These theoretical results served to stimulate recent experimental investigation of the photoinduced isomerization processes in derivatives of BAN. In Chapter 5, the time-dependent photoionization processes in furan are examined in close collaboration with the experimental group of Prof. Suzuki (Kyoto University, Kyoto, Japan).[85,86] Furan exhibits an interesting complexity of low-lying $\pi - \pi^*$ and Rydberg states that is also present in various biomolecular building blocks. The simulations reveal for the first time the mechanism for the ultrafast photorelaxation, thus allowing for the complete assignment to the time-resolved processes present in the experimental TRPES spectrum. The focus of Chapter 6 is the pyrazine molecule, which is a structural unit in various biomolecules and serves as a prototype system for the $\pi - \pi^* \rightarrow \mathrm{n} - \pi^*$ photoinduced internal conversion.[39] The excellent agreement of the theoretical TRPES including the approximated ionization probabilities with recent experimental measurements carried out in Prof. Suzuki's group demonstrates that the transition dipole moments to the ionization continuum have to be taken into account for the accurate simulation of TRPES.[84] In Chapter 7, the extension of the nonadiabatic dynamics to the approximate TDDFTB for the simulation of biomolecules in solution is illustrated on the ultrafast photodynamics of microsolvated adenine.[63]

In Part III, conclusions and an outlook are provided.

# Part I

# Methodology

# 1 Computational Methods for Structures and Electronic States

## 1.1 Density Functional Theory

Density functional theory (DFT) represents a very efficient approach for the calculation of molecular properties, which does not require the knowledge of the wavefunction. It is based on the fact that the properties of a system are unambiguously determined by its electron density. The foundation of DFT are the two Hohenberg-Kohn (HK) theorems. The first HK theorem ensures a one-to-one mapping of the exact electron density $\rho$ and the external potential, which contains the electron-nuclear attraction and any additional magnetic or electric field. As a consequence, the properties of the system, such as the ground state energy, are unique functionals of the electron density. The second HK theorem guarantees the existence of a variational principle for electron densities. Thus, if the exact functional is known, the true electron density can be obtained following the variational principle.

DFT calculations are presently almost exclusively based on a formalism developed by Kohn and Sham,[87] who introduced a non-interacting reference system, which gives rise to the same density as the real system. This density is constructed from the so-called Kohn-Sham (KS) orbitals based on a one-determinantal wavefunction. This formalism allows for the exact calculation of the kinetic energy of the non-interacting electrons, which represents a large part of the kinetic energy of the real system. The remaining part of the kinetic energy as well as the non-classical exchange and correlation contributions to the electron-electron interaction are gathered in the exchange-correlation functional $E_{XC}$.

Following the variational principle by solving the Kohn-Sham-eigenvalue equations, the formally exact energy of the system can be calculated:

$$h^{KS}\phi_i = \varepsilon_i \phi_i \, . \tag{1.1}$$

Here, $\phi_i$ are KS orbitals, $\varepsilon_i$ are eigenvalues, and $h^{KS}$ is the KS one-electron operator defined as:

$$h^{KS}(\mathbf{r}) = -\frac{1}{2}\nabla_{\mathbf{r}}^2 - \sum_K \frac{Z_K}{|\mathbf{r}-\mathbf{R}_K|} + \int \frac{\rho\left(\mathbf{r}'\right)}{|\mathbf{r}-\mathbf{r}'|} d\mathbf{r}' + \frac{\delta E_{XC}\left[\rho(\mathbf{r})\right]}{\delta\rho(\mathbf{r})} \, . \tag{1.2}$$

The first term on the right hand side is the kinetic energy operator, the second term describes the electrostatic electron-nuclear interaction, the third term describes the classical part of the electron-electron interaction, and the fourth term the derivative of $E_{XC}$ with respect to the density. In principle, the KS orbitals can be determined numerically. However, since the numerical determination is limited to very small systems due to the large computational demand, the KS orbitals are usually expanded in terms of atomic basis functions.

Depending on the ansatz, many different approximate exchange-correlation functionals are available today. Usually, the functional is divided into an exchange and a correlation part. Currently used functionals can be divided into four different classes:

**(i) Local functionals:** These functionals are based on the early "Local Spin Density Approximation" (LSDA), which treats the electron density locally as a uniform electron gas. LSDA functionals are exact for the special case of a uniform electron gas. However, in molecular systems the exchange energy is systematically underestimated, thus yielding too large dissociation energies, and the electron correlation is overestimated. Moreover, the asymptotic behavior of LSDA functionals is wrong for large distances.

**(ii) Gradient corrected functionals (GGA):** Improvements of the LSDA method mostly consider a non-uniform electron gas, which can be achieved by including the dependence of exchange and correlation energies from the gradient of the electron density. In the majority of those functionals, the derivative of the electron density is introduced as a correction which is added to an LSDA functional. The correction ameliorates the wrong asymptotic behavior of the exchange and correlation energy, thus improving significantly the description of chemical binding energies with respect to LSDA.

**(iii) Meta-GGA functionals:** The local extension of GGA-methods allows the exchange and correlation functionals to depend on higher derivatives of the density as e.g. on the Laplacian of the density or the orbital kinetic energy density. The meta-GGA functionals are, in contrast to LSDA or GGA functionals, free from self-interaction errors, since the correlation functional is constructed in such a way that the correlation energy vanishes for any one-electron density.

**(iv) Hybrid functionals:** Currently used hybrid methods as introduced by Becke [88] are based on the "Adiabatic Connection Formula", [89] which justifies the mixing of DFT exchange-correlation with a certain amount of exact Hartree-Fock (HF) exchange. The inclusion of the HF exchange leads to significant improvement of the GGA results, in particular by reducing the strong overbinding tendency from all local DFT methods, although the optimum fraction to be included depends on the specific system properties.

### 1.1.1 Limitations of DFT

The weak interactions, such as van der Waals type interactions between molecules, are poorly described by most currently used DFT functionals. Loosely bound electrons and Rydberg states also represent a problem for the major part of the functionals. The source of the problem is the wrong long-range behavior of DFT due to the missing cancellation of the long-range part of exchange and correlation energy. This can be overcome by introducing corrections to the incorrect long-range behavior of the $E_{XC}$ potential, e.g. by an "ad hoc" addition of an empirical correction. [48,51] Recent work has attempted to address this problem by separating the correlation functional into a long- and a short-range part. The short-range exchange is described by a local potential derived from LSDA or GGA, while the long-range part is treated with the exact HF exchange potential.[50,55]

DFT can only describe the lowest electronic state of each irreducible representation of the molecular spatial symmetry group. However, excited states can be described by introducing linear response theory in the frame of time-dependent DFT as presented in Section 1.2.

## 1.2 Time-Dependent Density Functional Theory

The time-dependent density functional theory (TDDFT) represents one of the most prominent and most widely used approaches for the calculation of excited state properties such as transition energies, oscillator strengths, or excited state geometries of medium-sized up to complex molecular systems. The theoretical foundation of TDDFT relies on the Runge-Gross theorem,[90] which was formulated as a time-dependent analog to the first HK theorem. The theorem states that the time-dependent electron density $\rho\left(\mathbf{r},t\right)$ determines the time-dependent external potential $V_{ext}\left(\mathbf{r},t\right)$ up to a spatially constant time-dependent function, provided that the system is in a defined electronic state $\Psi_0$ at $t=0$.

In the linear response (LR) formulation of TDDFT, the change of the density is described by first order perturbation theory under the assumption that the perturbation is turned on slowly (adiabatic approximation) and that the system initially resides in the ground state with the corresponding density $\rho_0$. This gives rise to a non-Hermitian linear response TDDFT equation:[91]

$$\begin{bmatrix} \mathbf{A} & \mathbf{B} \\ \mathbf{B}^* & \mathbf{A}^* \end{bmatrix} \begin{bmatrix} \mathbf{X} \\ \mathbf{Y} \end{bmatrix} = \varepsilon \begin{bmatrix} 1 & 0 \\ 0 & -1 \end{bmatrix} \begin{bmatrix} \mathbf{X} \\ \mathbf{Y} \end{bmatrix}, \tag{1.3}$$

where the matrices **A** and **B**, whose dimensions are the number of occupied orbitals, are defined as:

$$\begin{aligned} A_{ia,jb} &= \delta_{ij}\delta_{ab}\left(\epsilon_a - \epsilon_i\right) + \left(ia|jb\right) + \left(ia\left|f_{XC}\right|jb\right) \\ B_{ia,jb} &= \left(ia|bj\right) + \left(ia\left|f_{XC}\right|bj\right). \end{aligned} \tag{1.4}$$

Here, the two-electron integrals are given in Mulliken notation, where $i$ or $j$ denote occupied and $a$ or $b$ signify virtual KS orbitals. $f_{XC}$ is the so-called exchange-correlation kernel, which in the widely applied adiabatic local density approximation corresponds to the second functional derivative of the exchange-correlation energy:

$$f_{XC} = \frac{\delta^2 E_{XC}\left[\rho\left(\mathbf{r}\right)\right]}{\delta\rho\left(\mathbf{r}\right)\delta\rho\left(\mathbf{r}'\right)} \, . \tag{1.5}$$

The solution of Eq. 1.3 and 1.4 yields the transition energies $\varepsilon$ as eigenvalues and the eigenvectors $|\mathbf{XY}\rangle$, if the unperturbed Hamiltonian is a pure DFT functional. A general formulation for hybrid functionals including the HF exchange, which differ in the definition of $\mathbf{A}$ and $\mathbf{B}$, can also be derived: [49]

$$A_{ia,jb} = \delta_{ij}\delta_{ab}\left(\epsilon_a - \epsilon_i\right) + (ia|jb) - c_{HF}\left(ij|ab\right) + \left(1 - c_{HF}\right)\left(ia\left|f_{XC}\right|jb\right)$$

$$B_{ia,jb} = (ia|bj) - c_{HF}\left(ib|aj\right) + \left(1 - c_{HF}\right)\left(ia\left|f_{XC}\right|bj\right) . \tag{1.6}$$

It contains both the response of the HF exchange potential as well as the response of the exchange-correlation functional at a rate determined by the factor $c_{HF}$, which is defined in the hybrid $E_{XC}$.

### 1.2.1 Limitations of TDDFT

In many cases, the results obtained with TDDFT are quite sensitive to the choice of $E_{XC}$. Although approximate functionals are used, valence states are usually reasonably well described with a typical error of $0.1 - 0.5$ eV. However, TDDFT has problems in describing Rydberg states, valence states of molecules exhibiting extended $\pi$-systems, and long-range charge-transfer states (cf. Section 1.2.2 for details) due to the wrong long-range behavior of DFT (cf. Section 1.1.1). Therefore, the reliability of the TDDFT results should always be checked by comparison with experimental data or with highly accurate wavefunction based benchmark calculations, such as the multi-reference configuration interaction (MRCI) or the equation-of-motion coupled cluster (EOM-CC) methods.

The linear response implementation of TDDFT in the adiabatic local density approximation cannot inherently describe excited states with a significant contribution of double or higher electron excitations, which are of multi-reference character, since only singly excited states are contained in the response formalism. Moreover, if the ground state density is not a good approximation as a starting point for the excited state, the problem of triplet instabilities can occur. [92] Recently, also the presence of conical intersections between the ground and excited electronic states in adiabatic TDDFT was critically examined. [93] Tapavicza et al. concluded that although the intersection topologies particularly for the $S_1 \rightarrow S_0$ crossing region might not be reproduced exactly, the relaxation pathways and photodynamics of their studied examples were not substantially influenced. [93]

### 1.2.2 Charge-Transfer Excited States in TDDFT

Although recently progress has been made in improving the performance of exchange and correlation functionals, most commonly used functionals still do not allow for the accurate description of excited states with long-range charge-transfer (CT) character. The transition energies of CT states are usually drastically underestimated and the correct $1/R$ dependence of the potential energy surface due to the electrostatic attraction of the positive and the negative charge separated by a distance $R$ is not reproduced.[49] The failure of TDDFT can be understood by analyzing Eq. 1.6 for a CT state. In this case, an electron is transferred from an occupied orbital $i$ to a virtual orbital $a$ in a different part of the molecule or even intermolecularly, so that the overlap of the two orbitals becomes zero. Consequently, all terms of Eq. 1.6 involving overlaps of occupied and virtual orbitals become zero, leading to:

$$
\begin{aligned}
A_{ia,jb} &= \delta_{ij}\delta_{ab}\left(\epsilon_a - \epsilon_i\right) - c_{HF}\left(ij|ab\right) \\
B_{ia,jb} &= 0\,. \qquad (1.7)
\end{aligned}
$$

In the resulting equations, the $B$-matrix becomes zero. In the $A$-matrix, only the first term involving the difference of the orbital energies and the term involving the non-local HF exchange term survive, whereas the response of the Coulomb potential and of $E_{XC}$ become zero. Thus, for the case of a pure DFT functional ($c_{HF} = 0$), the transition energy is simply given by the difference of the orbital energies $\epsilon_a - \epsilon_i$. In contrast to e.g. the HF theory, in DFT the virtual orbitals are usually too low in energy and thus do not provide good estimates for the calculation of transition energies from the difference of orbital energies. Moreover, the transition energy is constant with respect to the charge separation instead of exhibiting $1/R$ dependence.

This failure is improved in a few TDDFT-schemes, where the exchange-correlation contribution is split into a long-range part that is calculated with HF exchange and a short-range part calculated with $E_{XC}$ from DFT.[47,53,54] An alternative approach is the time-dependent current density functional theory.[94]

A possibility to check for the long-range charge-transfer character of excited states is the calculation of the recently introduced quantity $\Lambda$,[95] which serves as an indicator for the long-range CT contribution to transitions. $\Lambda$ is defined as:

$$\Lambda = \frac{\sum_{ia} c_{ia}^2 O_{ia}}{\sum_{ia} c_{ia}^2}\,, \qquad (1.8)$$

where $O_{ia}$ is the inner product of the moduli of an occupied and a virtual orbital $O_{ia} = \langle|\phi_i|||\phi_a|\rangle$. $c_{ia} = X_{ia} + Y_{ia}$ labels the contribution of $\phi_i \rightarrow \phi_a$ to a given transition, where $X_{ia}$ and $Y_{ia}$ are elements of the eigenvectors in the LR-TDDFT eigenvalue equation 1.3. $\Lambda$ is restricted to the range between 0 and 1, where low values indicate long-range excitations, e.g. CT or Rydberg, while large values signify short-range excitations. It has been found that in general, large TDDFT errors are associated with small $\Lambda$ values and small errors with large $\Lambda$ values.[95] This tendency is more pronounced for pure DFT functionals than for hybrid functionals, which in general yield better results for long-range excitations due to the increased amount of HF long-range contribution. Therefore, the $\Lambda$ values can be used to estimate the accuracy of TDDFT for a given transition.

In spite of these known drawbacks, TDDFT is still the only ab initio method which can be efficiently applied to complex systems. The availability of analytic excited state gradients in standard programs such as Turbomole[96] allows for efficient calculation of first-order properties of excited states, as e.g. their excited state equilibrium structures, transition dipole moments between ground and excited states, or harmonic frequencies. Therefore, it is highly desirable to utilize TDDFT for ab initio nonadiabatic dynamics simulations as well as for the calculation of ultrafast time-dependent observables such as TRPES.

## 1.3 Density Functional Tight Binding

Currently, DFT can treat up to 100 atoms in routine applications, sometimes even more, and has been successfully applied to molecular dynamics simulations up to several picoseconds. In order to extend the applicability of the simulations to even more complex system such as large biochromophores, solid state physics, or molecules surrounded by solvate molecules, approximations to DFT such as the density functional tight binding (DFTB) method have been developed.[56–59] DFTB has been shown to provide a quite accurate description of ground state properties such as molecular geometries, vibrational frequencies, and reaction energies comparable in accuracy to full DFT.[58,61] It has been successfully applied to a wide range of problems in the fields of biomolecules, surfaces, interfaces, and point and extended defects in solid-state systems.[59,97,98]

The DFTB method is derived from DFT by choosing a reference density $\rho_0$ as a superposition of neutral atomic densities $\rho_0 = \sum_A \rho_A^0$ and by expanding the DFT exchange-correlation energy up to second order:[58]

$$\begin{aligned} E = & \sum_i^{occ} n_i \left\langle \phi_i \left| \hat{H}^0 \right| \phi_i \right\rangle + \frac{1}{2} \int\int \left( \frac{1}{|\mathbf{r}-\mathbf{r}'|} + \left. \frac{\delta^2 E_{XC}}{\delta\rho\,\delta\rho'} \right|_{n_0} \right) \delta\rho\,\delta\rho' d\mathbf{r} d\mathbf{r}' \\ & - \frac{1}{2} \int\int \frac{\rho_0(\mathbf{r})\,\rho_0(\mathbf{r}') d\mathbf{r} d\mathbf{r}'}{|\mathbf{r}-\mathbf{r}'|} + E_{XC}[\rho_0] - \int V_{XC}[\rho_0]\,\rho_0\,d\mathbf{r} + E_{ii}\,. \end{aligned} \tag{1.9}$$

Here, $\phi_i$ are the KS orbitals, $n_i$ are their occupation numbers, $\hat{H}^0$ is the KS-Hamiltonian evaluated at the reference density, $E_{XC}$ and $V_{XC}$ are the exchange-correlation energy and potential, and $E_{ii}$ are the core-core repulsions. Eq. 1.9 serves as a starting point for further approximations leading to the tight binding version of DFT.

The second term on the right hand side of Eq. 1.9, which describes the energy contribution due to the density fluctuation, can be decomposed in atom centered monopole contributions:

$$E^{2nd} \approx \frac{1}{2}\sum_{AB} \Delta q_A \gamma_{AB} \Delta q_B \,, \tag{1.10}$$

where the charge fluctuations $\Delta q_A$ on atom $A$ are estimated from the Mulliken charge analysis. $\gamma_{AB}$ is the so-called $\gamma$-functional defined as:

$$\gamma_{AB} = \int\int \left( \frac{1}{|\mathbf{r}-\mathbf{r}^{'}|} + \left.\frac{\delta^2 E_{XC}}{\delta\rho\,\delta\rho^{'}}\right|_{n_0} \right) F_A\left(\mathbf{r}\right) F_B(\mathbf{r}^{'}) d\mathbf{r} d\mathbf{r}^{'} . \tag{1.11}$$

Here, $F_A$ denotes the normalized spherical density distribution located on $A$, which means that the angular deformation of the charge density in second order is neglected. In the short-range limit $|\mathbf{r}-\mathbf{r}^{'}| \to 0$, $E^{2nd}$ describes the electron-electron interaction on atom $A$. In this case, $\gamma_{AB}$ can be approximated as a Hubbard-type interaction depending only on the Hubbard parameter (also known as chemical hardness) $U_A$ leading to:

$$E^{2nd} \approx \frac{1}{2} U_A \Delta q_A^2 \,. \tag{1.12}$$

The first term on the right hand side of Eq. 1.9 involves the summation over Kohn-Sham orbitals, which are expanded as linear combination of a minimal basis set in DFTB. Employing the basis functions $b_\nu$, the first order Hamiltonian terms in Eq. 1.9 can be expressed as an eigenvalue equation:

$$\left\langle \phi_i \middle| \hat{H}^0 \middle| \phi_i \right\rangle = \sum_{\mu\nu} c_\mu^i H_{\mu\nu}^0 c_\nu^i = \epsilon_i \sum_{\mu\nu} c_\mu^i S_{\mu\nu} c_\nu^i \,, \tag{1.13}$$

with the KS molecular orbital coefficients $c_\mu^i$ and the overlap matrix elements $S_{\mu\nu} = \langle b_\mu | \, b_\nu \rangle$. The Hamiltonian matrix elements have the form:

$$H_{\mu\nu}^0 = \left\langle b_\mu \middle| \hat{H}^0 \middle| b_\nu \right\rangle . \tag{1.14}$$

The diagonal elements thus correspond to atomic KS eigenvalues and the non-diagonal Hamiltonian matrix elements are calculated in a two-center approximation:

$$H_{\mu\nu}^0 = \left\langle b_\mu \middle| \hat{T} + V_{eff}\left[\rho_A^0 + \rho_B^0\right] \middle| b_\nu \right\rangle , \tag{1.15}$$

where $b_\mu$ and $b_\nu$ are centered on atoms $A$ and $B$, respectively, and $V_{eff}$ is the effective KS potential.

The four terms in the second line of Eq. 1.9 depend only on the neutral atomic densities and inter-atomic distances and are therefore collected in a repulsive potential $E_{rep}$:

$$E_{rep} = -\frac{1}{2}\int\int \frac{\rho_0\left(\mathbf{r}\right)\rho_0(\mathbf{r}')d\mathbf{r}d\mathbf{r}'}{|\mathbf{r}-\mathbf{r}'|} + E_{XC}\left[\rho_0\right] - \int V_{XC}\left[\rho_0\right]\rho_0\, d\mathbf{r} + E_{ii}\,, \tag{1.16}$$

where $E_{rep}$ can be approximated as a sum of short-range two body potentials $U_{AB}$:

$$E_{rep} = \frac{1}{2}\sum_{AB} U_{AB}\left(R_{AB}\right). \tag{1.17}$$

In practice, $U_{AB}$ is usually fitted from the difference of the total DFT energy and the electronic part of the DFTB energy with respect to the bond length $R_{AB}$ of an atom pair for an adequate set of reference systems. The determination of the pair potentials exhibits an effort of $N^2$ for $N$ sorts of atoms.

Employing the above described definitions and approximations, the total DFTB energy can be summarized as:

$$E_{tot} = \sum_{i}^{occ} n_i \sum_{\mu\nu} c_\mu^i H_{\mu\nu}^0 c_\nu^i + \frac{1}{2}\sum_{AB}\Delta q_A \gamma_{AB}\Delta q_B + E_{rep}\,. \tag{1.18}$$

Applying the variational principle leads to the KS eigenvalue problem:

$$\sum_{\nu}\left(H_{\mu\nu} - \epsilon_i S_{\mu\nu}\right) c_\nu^i = 0 \tag{1.19}$$

with the KS orbital energies $\epsilon_i$, and the Hamilton matrix elements $H_{\mu\nu}$ given as:

$$H_{\mu\nu} = H_{\mu\nu}^0 + \frac{1}{2} S_{\mu\nu}\sum_{C}\left(\gamma_{AC} + \gamma_{BC}\right)\Delta q_C\,. \tag{1.20}$$

Notice that the $H_{\mu\nu}$ are calculated only once for all possible combinations of elements with a DFT functional for a dense grid of two atomic distances and are tabulated after that. The $S_{\mu\nu}$ have to be calculated from the atomic orbitals, since the basis set is not orthogonal, but this is also only performed once. Subsequently, a tabulated form is used. Since no integral evaluation is necessary during the calculations, the remaining computational effort for the determination of the total DFTB energy is the iterative solution of the eigenvalue problem in Eq. 1.20. Thus, the computational costs are dramatically reduced compared to DFT. Therefore, DFTB allows the calculation of systems up to several hundreds of atoms.

## 1.3.1 Limitations of DFTB

The molecular geometries optimized by DFTB are comparable to those obtained from DFT, while the vibrational properties are not sufficiently accurate, especially if DFTB is not used in the self-consistent charge (SCC) version. The inaccuracy for the vibrational frequencies has been improved by applying a special parametrization of the repulsive potential which employs experimental data.[99] A further improvement of energies and frequencies seems to be possible by optimizing the strategies for the parametrization of $E_{rep}$, e.g. by a more extensive use of experimental data or by employing genetic algorithms for the fitting procedure as suggested by Knaup et al.[100]

In current DFTB, the Hubbard parameters (cf. Eq. 1.12) are assumed to be constant, thus neglecting their dependence on atomic charge. However, this dependence is important for the correct description of deprotonation energies or the total energies of ions. This deficiency might be overcome by introducing the derivative of the chemical hardness with respect to the atomic charge, as indicated by results of Elstner et al.[101] Other routes to improve the accuracy of DFTB are to advance the schemes for the evaluation of the atomic charges $\Delta q_A$ or to further optimize the $\gamma$-functional.

Since DFTB is an approximation based on GGA functionals, it also shares all of the shortcomings of current DFT-GGA functionals (cf. Section 1.1.1), such as the problem of over-polarizability in extended conjugated systems and the problem of van der Waals interactions.[101] The latter problem has been addressed in an “ad hoc” way by adding an empirical dispersion correction to the total energy.[102]

## 1.4 Time-Dependent Density Functional Tight Binding

A particularly attractive possibility to extend the applicability of the TDDFT nonadiabatic dynamics to even larger systems is to introduce the tight binding approximation to TDDFT yielding the TDDFTB method. Since analytic energy derivatives have been implemented in the frame of TDDFTB,[62] it allows for the description of the optical response and dynamics of complex molecular systems.

The route to the time-dependent density functional tight binding approach is very similar to the one used for the TDDFT approach. In order to obtain the single particle KS orbitals $\phi_i$, a self-consistent DFTB calculation is performed (cf. Section 1.3). In a second step, the transition energies $\varepsilon$ can be obtained as a solution of the eigenvalue problem as defined in Eq. 1.3. In the case of TDDFTB, the matrix elements of **A** and **B** are given by:

$$\begin{aligned} A_{ia,jb} &= \delta_{ij}\delta_{ab}\left(\epsilon_a - \epsilon_i\right) + 2K_{ia,jb} \\ B_{ia,jb} &= 2K_{ia,jb}\,, \end{aligned} \tag{1.21}$$

where $i$ and $j$ denote occupied orbitals while $a$ and $b$ are virtual orbitals with the orbital energies $\epsilon_a$ and $\epsilon_i$. The coupling matrix $K_{ia,jb}$ describes the response of the self-consistent field potential with respect to a change in the electron density. In the adiabatic approximation, the coupling matrix has the form:

$$K_{ia,jb} = \int\int \phi_i(\mathbf{r})\,\phi_a(\mathbf{r})\left(\frac{1}{|\mathbf{r}-\mathbf{r}'|} + \left.\frac{\delta^2 E_{XC}}{\delta\rho(\mathbf{r})\,\delta\rho'(\mathbf{r}')}\right|_{n_0}\right)\phi_j(\mathbf{r}')\phi_b(\mathbf{r}')d\mathbf{r}d\mathbf{r}', \tag{1.22}$$

which can be further simplified by using the generalized Mulliken approximation:

$$K_{ia,jb} = \sum_{AB} q_A^{ia}\gamma_{AB}q_B^{jb}\,, \tag{1.23}$$

where the integral $\gamma_{AB}$ is approximated exactly like in the ground state case and $q_A^{ia}$ denotes Mulliken charge atomic transition densities:

$$q_A^{ia} = \frac{1}{2}\sum_{\mu\nu}\left(c_\mu^i S_{\mu\nu} c_\nu^a + c_\nu^i S_{\nu\mu} c_\mu^a\right). \tag{1.24}$$

Since the form of the coupling matrix element is consistent with the monopole approximation for the ground state, its evaluation does not require the integral calculation, thus making the TDDFTB calculations highly efficient.

### 1.4.1 Limitations of TDDFTB

The comparison of the accuracy of the TDDFTB approach with full TDDFT yields a very good agreement for singlet electronic states, while the performance of TDDFTB for triplet states shows slightly larger systematic errors.[60,103] Moreover, excitations of $n \rightarrow \pi^*$ character exhibit substantial errors due to the monopolar approximation, since the Mulliken atomic transition energies for this kind of transition are zero, thus leading to no coupling.[103]

While TDDFTB reproduces the accuracy of the TDDFT method in a wide range, it also shares all of its deficiencies, such as the inability to describe accurately excited states with long-range charge-transfer or Rydberg character, as well as excited states with significant contribution of double or higher electron excitations (cf. 1.2.1 and 1.2.2).

Despite these drawbacks, TDDFTB represents an efficient method for the simulation of ultrafast excited state processes in very large systems and makes it possible to include the environment in the simulations. Thus, its combination with nonadiabatic dynamics “on the fly” is highly desirable and has been realized in the frame of this thesis.[63]

# 2 Simulation of Nonadiabatic Dynamics

## 2.1 Introduction

The exploration of ultrafast nonadiabatic photoinduced dynamics involving several coupled excited electronic states in large systems such as biomolecules or nanostructures still represents a major challenge from the theoretical point of view. In this context, the combination of trajectory based semiclassical dynamics with the time-dependent density functional theory (TDDFT), allowing for the efficient calculation of the electronic structure of complex molecular systems, provides a promising route. One of the methods for the description of quantum effects due to electronic transitions in the frame of the semiclassical dynamics is Tully's surface hopping (TSH) procedure.[29,30] In this approach, the classical trajectories are propagated on a single potential energy surface (PES) except for instantaneous transitions among the surfaces. Due to its efficiency and the possibility of combination with the "on the fly" dynamics without precalculation of the energy surfaces, the TSH procedure has become the most prominent method for nonadiabatic dynamics simulations of complex systems. Therefore, an approach combining the TDDFT based semiclassical dynamics with the TSH procedure has been developed in this thesis[39,40,63] and will be presented in the following sections.

This chapter is structured as follows: First, a short general introduction to semiclassical dynamics and to Tully's surface hopping procedure is given. Subsequently, an approach for the nonadiabatic dynamics in the frame of the linear response TDDFT based on localized Gaussian atomic basis sets and its extension to the approximate tight binding TDDFT is presented. Finally, the approach is validated by the example of the methaniminium cation $CH_2NH_2^+$, which was studied by employing the more accurate ab initio complete active space self-consistent field (CAS-SCF) method by Barbatti et al.[37]

## 2.2 Semiclassical Dynamics and Tully's Surface Hopping Procedure

The trajectory based semiclassical dynamics allows for treating complicated polyatomic systems in full dimensionality, since it requires drastically less computational effort than full quantum dynamics calculations. Despite the classical description of the nuclear dynamics, quantum phenomena such as optical transitions between excited states can be approximately described by means of averaging over the ensemble of classical trajectories. Additionally, the semiclassical dynamics can be combined directly with different quantum chemistry methods for the electronic structure calculations. Since the Born-

Oppenheimer approximation is the foundation of modern quantum chemistry and provides a starting point for the derivation of semiclassical dynamics, it will be outlined in the following section.

### 2.2.1 Born-Oppenheimer Approximation

A complete description of a molecular system in the absence of external fields is provided by the time-dependent Schrödinger equation:

$$i\hbar\frac{\partial\Psi\left(\mathbf{r},\mathbf{R},t\right)}{\partial t}=\hat{H}\left(\mathbf{r},\mathbf{R}\right)\Psi\left(\mathbf{r},\mathbf{R},t\right) \tag{2.1}$$

with the total non-relativistic Hamiltonian:

$$\hat{H}\left(\mathbf{r},\mathbf{R}\right)=\hat{T}_n\left(\mathbf{R}\right)+\hat{T}_e\left(\mathbf{r}\right)+\hat{V}_{nn}\left(\mathbf{R}\right)+\hat{V}_{ee}\left(\mathbf{r}\right)+\hat{V}_{ne}\left(\mathbf{r},\mathbf{R}\right), \tag{2.2}$$

where $\mathbf{R}$ and $\mathbf{r}$ are the nuclear and electronic coordinates and $\hat{T}_n\left(\mathbf{R}\right)=-\frac{1}{2}\sum_A(1/m_A)\times\nabla_A^2$ and $\hat{T}_e\left(\mathbf{r}\right)=-\frac{1}{2}\sum_i\nabla_i^2$ are the kinetic energies of the nuclei and electrons, respectively. $\hat{V}_{nn}\left(\mathbf{R}\right)=\sum_{A<B}(Z_AZ_B)\,/\,|\mathbf{R}_A-\mathbf{R}_B|$ represents the nuclear-nuclear Coulomb repulsion, while $\hat{V}_{ee}\left(\mathbf{r}\right)=\sum_{i<j}1\,/\,|\mathbf{r}_i-\mathbf{r}_j|$ is the electron-electron Coulomb repulsion and $\hat{V}_{ne}\left(\mathbf{r},\mathbf{R}\right)=\sum_{Ai}-Z_A\,/\,|\mathbf{R}_A-\mathbf{r}_i|$ the nuclear-electron Coulomb attraction.

Since the masses of the electrons are substantially smaller than the masses of the nuclei, their dynamics take place on a much shorter timescale. On the timescale of the electronic motion, the nuclei can be regarded as almost stationary, whereas on the timescale of the nuclear motion, the electrons move so fast that they can be replaced by an effective potential which governs the motion of the nuclei. This intuitive picture can be used as a starting point for the Born-Oppenheimer approximation,[104] which will be described in detail below. Due to the large difference of the nuclear and electronic masses, $m_A\to\infty$ can be assumed in a first step of the solution of the Schrödinger equation 2.1. Thus, the nuclear coordinates become fixed and the nuclear kinetic energy vanishes. The electronic states can then be obtained from the solution of the time-independent electronic Schrödinger equation:

$$\hat{H}_{el}\left(\mathbf{r};\mathbf{R}\right)\psi_I\left(\mathbf{r};\mathbf{R}\right)=E_I\left(\mathbf{r};\mathbf{R}\right)\psi_I\left(\mathbf{r};\mathbf{R}\right), \tag{2.3}$$

where the electronic Hamiltonian $\hat{H}_{el}$ becomes parametrically dependent on the nuclear coordinates. Since the electronic wavefunctions $\psi_I\left(\mathbf{r};\mathbf{R}\right)$ build a complete basis set, the total wavefunction $\Psi\left(\mathbf{r},\mathbf{R},t\right)$ can be expanded in terms of the electronic wavefunctions as:

$$\Psi\left(\mathbf{r},\mathbf{R},t\right)=\sum_I\chi_I\left(\mathbf{R},t\right)\psi_I\left(\mathbf{r};\mathbf{R}\right), \tag{2.4}$$

where the nuclear wavefunctions $\chi_I(\mathbf{R}, t)$ depend only on $\mathbf{R}$ and $t$. Insertion of this ansatz into the time-dependent Schrödinger equation yields a coupled set of equations for the $\chi_I(\mathbf{R}, t)$:

$$i\hbar \frac{\partial \chi_I(\mathbf{R}, t)}{\partial t} = \left(\hat{T}_n(\mathbf{R}, t) + E_I(\mathbf{R}, t)\right) \chi_I(\mathbf{R}, t) - \sum_K \hat{B}_{IK}\, \chi_K(\mathbf{R}, t) \,. \tag{2.5}$$

The operators $\hat{B}_{IK}$ describe the nonadiabatic couplings between nuclear and electronic degrees of freedom:

$$\hat{B}_{IK} = \sum_A \frac{1}{2m_A} \left[2 \left\langle \psi_I(\mathbf{r}; \mathbf{R}) \middle| \nabla_{\mathbf{R}_A} \middle| \psi_K(\mathbf{r}; \mathbf{R}) \right\rangle \cdot \nabla_{\mathbf{R}_A} + \left\langle \psi_I(\mathbf{r}; \mathbf{R}) \middle| \nabla^2_{\mathbf{R}_A} \middle| \psi_K(\mathbf{r}; \mathbf{R}) \right\rangle \right] . \tag{2.6}$$

Neglecting the couplings between different electronic states ($I \neq K$) yields the adiabatic approximation, in which the total molecular wavefunction reduces to the product of a single nuclear and electronic wavefunction $\Psi(\mathbf{r}, \mathbf{R}, t) = \chi_I(\mathbf{R}, t)\, \psi_I(\mathbf{r}; \mathbf{R})$. In this approximation, the nuclear wavefunction $\chi_I(\mathbf{R}, t)$ is obtained as the solution of the equation:

$$i\hbar \frac{\partial \chi_I(\mathbf{R}, t)}{\partial t} = \left(\hat{T}_n(\mathbf{R}, t) + E_I(\mathbf{R}, t) + \hat{B}_{II}\right) \chi_I(\mathbf{R}, t) \,. \tag{2.7}$$

Neglecting the small correction $\hat{B}_{II}$ in Eq. 2.7 yields the Born-Oppenheimer approximation. This approximation is valid for the case of well separated electronic states and allows for the separation of nuclear and electronic coordinates, therefore reducing the dynamics to the nuclear motion on a single adiabatic surface.

A further simplification of Eq. 2.7 can be achieved by treating the nuclear motion by classical mechanics. In these semiclassical approaches, the nuclei follow classical trajectories $\mathbf{R}(t)$, while the electrons can be described by a time-dependent adiabatic wavefunction $\psi_I(\mathbf{r}; \mathbf{R}(t))$.

If the electronic states are not well separated, which is the case for most processes in the photodynamics of molecules, the $\hat{B}_{IK}$ terms describing the nonadiabatic effects have to be taken into account. Neglecting the second order couplings in Eq. 2.6, the $\hat{B}_{IK}$ can be expressed in terms of the nonadiabatic coupling vectors $\mathbf{d}_{IK}$:

$$\hat{B}_{IK} \approx \sum_A \frac{1}{m_A} \mathbf{d}_{IK} \cdot \nabla_{\mathbf{R}_A} \,, \tag{2.8}$$

where the $\mathbf{d}_{IK}$ are defined as:

$$\mathbf{d}_{IK} = \langle \psi_I(\mathbf{r}; \mathbf{R}(t)) | \nabla_{\mathbf{R}_A} | \psi_K(\mathbf{r}; \mathbf{R}(t)) \rangle \,. \tag{2.9}$$

These nonadiabatic coupling vectors play a key role in surface hopping procedures such as Tully's surface hopping, which allows for the description of nonadiabatic transitions in trajectory based semiclassical dynamics.

### 2.2.2 Semiclassical Dynamics

The most widely applied semiclassical methods, which incorporate quantum effects due to electronic transitions, are either based on surface hopping or mean-field approaches. In surface hopping procedures, an ensemble of trajectories is propagated and each trajectory moves classically on a single PES except for instantaneous transitions among the surfaces. There are several different surface hopping approaches which mainly differ in the implementation of the state switches.[28,29,105–112] The most prominent is Tully's surface hopping procedure.[29,30]

In the mean-field or Ehrenfest approach, the classical trajectories are propagated along PESs that are weighted averages of many electronic states. This approach suffers from two main deficiencies:

1. The transition probabilities can be quite accurate in the region of strong coupling. In contrast, when the trajectories leave this region, they still evolve on an average PES instead of a single energy surface corresponding to one of the branches. Therefore, the mean-field method cannot be used to describe the evolution of minor channels if they involve energy surfaces which differ considerably from that of the major channel, as e.g. in molecular scattering processes.

2. The correct long-time equilibrium limit for a quantum subsystem coupled to a classical bath is not achieved: The temperature of the quantum subsystems does not approach the same temperature as the classical bath.[113]

Tully's surface hopping procedure, which is described in detail in the following section, addresses both of these deficiencies.[29,30,113]

### 2.2.3 Tully's Surface Hopping Procedure

The surface hopping procedure was initially introduced by Tully and Preston in 1971[28] and was generalized in 1990 to the widely applied fewest switches surface hopping procedure.[29] The basic idea is that independent trajectories evolve on single PESs, interrupted only by the possibility of sudden switches to another surface at a rate determined by the nonadiabatic coupling vectors $\mathbf{d}_{IK}$ defined in Eq. 2.9.

Following the spirit of semiclassical dynamics, the electronic wavefunction is represented in the basis of adiabatic Born-Oppenheimer states $|\psi_K(\mathbf{r};\mathbf{R}(t))\rangle$:

$$|\psi(\mathbf{r};\mathbf{R}(t))\rangle = \sum_K C_K(t)\,|\psi_K(\mathbf{r};\mathbf{R}(t))\rangle\,, \tag{2.10}$$

which are parametrically dependent on the classical nuclear trajectory $\mathbf{R}(t)$ obtained by solving Newton's equations of motion. The time-dependent electronic state coefficients

$C_K(t)$ are calculated along a given classical trajectory by solving the time-dependent Schrödinger equation:[29,30]

$$i\hbar \frac{dC_K(t)}{dt} = E_K(\mathbf{R}(t))C_K(t) - i\hbar \sum_I \left\langle \psi_K(\mathbf{r};\mathbf{R}(t)) \middle| \frac{\partial \psi_I(\mathbf{r};\mathbf{R}(t))}{\partial t} \right\rangle C_I(t)\,. \tag{2.11}$$

Here, $E_K$ represents the energy of the electronic state $K$. The second term on the right hand side of the equation corresponds to the nonadiabatic coupling $D_{KI}$ between the states $K$ and $I$:

$$D_{KI}(\mathbf{R}(t)) = \left\langle \psi_K(\mathbf{r};\mathbf{R}(t)) \middle| \frac{\partial \psi_I(\mathbf{r};\mathbf{R}(t))}{\partial t} \right\rangle, \tag{2.12}$$

which can be expressed as a scalar product of the nonadiabatic coupling vector $\mathbf{d}_{KI}$ as defined in Eq. 2.9 and the nuclear velocity $\frac{d\mathbf{R}(t)}{dt}$:

$$D_{KI}(\mathbf{R}(t)) = \mathbf{d}_{KI} \cdot \frac{d\mathbf{R}(t)}{dt}\,. \tag{2.13}$$

This is particularly suitable if the nonadiabatic coupling vectors can be directly calculated "on the fly" using e.g. ab initio quantum chemical methods.[9,11,37,114]

Alternatively, the nonadiabatic coupling can be approximately calculated by using the finite difference approximation for the time derivative:

$$\begin{aligned} D_{KI}(\mathbf{R}(t+\frac{\Delta}{2})) \approx \frac{1}{2\Delta}\, &[\langle \psi_K(\mathbf{r};\mathbf{R}(t))\, | \psi_I(\mathbf{r};\mathbf{R}(t+\Delta)) \rangle \\ &- \langle \psi_K(\mathbf{r};\mathbf{R}(t+\Delta))\, | \psi_I(\mathbf{r};\mathbf{R}(t)) \rangle] \end{aligned} \tag{2.14}$$

with the time step $\Delta$ for the integration of the classical Newton's equations of motion.

Within the TSH procedure, the $D_{KI}$ are required for the calculation of the hopping probabilities which determine the rate of switches between the adiabatic PESs. For a trajectory evolving on surface $E_K$, the hopping probabilities $P_{KI}$ to all other electronic states $I$ are calculated according to the following equation:[29]

$$P_{KI}(t) = -2\Delta \frac{\mathrm{Re}\,(C_K^*(t)C_I(t)D_{KI}(t))}{|C_K(t)|^2}\,. \tag{2.15}$$

In the case of negative $P_{KI}$, the $P_{KI}$ are set to zero. This approach ensures that the fraction of trajectories residing in state $K$ equals the quantum probability $|C_K(t)|^2$. In contrast to mean-field methods, the branching of trajectories into different pathways is possible with this approach. Due to the nature of the algorithm that determines when an electronic switch will occur, the number of switches is minimized. Therefore, excessive hopping, which would lead to a resemblance of the dynamics to a weighted averaging of the adiabatic states, is avoided.

Schematically, the TSH procedure for one trajectory is performed in the following way:

1. Generation of the initial conditions (initial momenta and coordinates) and of the initial electronic density matrix consistently with the conditions of the simulation (cf. Section 2.4.1).
2. Integration of the classical equations of motion for the nuclei from $t$ to $t + \Delta$ on the PES $E_K$ and integration of Eq. 2.11 along this trajectory in order to obtain the coefficients $C_K(t)$.
3. Calculation of the hopping probabilities $P_{KI}$ according to Eq. 2.15. Subsequently, a uniform random number is generated in order to determine if a state switch occurs.
4. If a state switch has occurred, the trajectory will now evolve on PES $E_I$ and the nuclear velocities have to be rescaled in order to conserve the total energy. Usually, rescaling is performed along the direction of the nonadiabatic coupling vector $\mathbf{d}_{KI}$.[115] Alternatively, in the case that only the scalar coupling $D_{KI}$ is calculated as e.g. in the TDDFT based approach that will be derived in the following section, the kinetic energy can be uniformly rescaled. If the kinetic energy is not sufficient to compensate the loss of potential energy due to the state switching, the hop is rejected (forbidden hop).
   Subsequently, the procedure will restart from step 2.

Notice that the electronic coefficients $C_K(t)$ are continuously integrated without resetting after state switches, thus electronic quantum coherence effects are retained.[29]

Due to the classical description of the nuclear motion, quantum mechanical behavior of the nuclei is neglected. Thus, processes involving tunneling, zero-point motion, quantum interference, or the quantization of vibrational levels cannot be described. The quantum mechanical behavior is particularly important for low-energy or hydrogen transfer processes, while it is less important for processes involving heavy atoms and high nuclear velocities. A similar problem is the incorrect description of quantum decoherence.[116] One possible solution is to include quantum decoherence, e.g. by resetting the quantum amplitudes (1 for occupied and 0 for unoccupied states) at some criterion, such as an estimated decoherence time or some physical characteristics.[117]

Another general deficiency is the internal inconsistency problem caused by classically forbidden hops, which leads to the deviation of TSH populations from the exact quantum probability. The appearance of this kind of hops is usually a hint for the manifestation of quantum tunneling, which cannot be properly described by a classical mechanics approach. It has been suggested to reverse the component of the momentum in the direction of the nonadiabatic coupling vector in the case of forbidden hops.[30,111] However, results of Müller et al. indicate that the adjustment of the momentum should be omitted.[118]

For systems in which quantum effects play an important role in the nuclear dynamics, the ab initio multiple spawning (AIMS) approach[119] has been introduced. However, this method is computationally more demanding than the TSH method, which limits its application to smaller systems. Full quantum dynamical simulations are extremely demanding and therefore only feasible for very small molecules. In systems where only few degrees of freedom exhibit significant quantum effects, the description by TSH based molecular dynamics can be improved by treating these few degrees of freedom quantum mechanically. This has been achieved e.g. for proton transfer in solution, where the hydrogen atom was treated quantum mechanically, while the heavier atoms obeyed classical dynamics.[30]

Due to its conceptual and computational simplicity, the TSH still remains the only generally applicable method for the simulation of nonadiabatic dynamics of complex molecular systems, in particular if quantum dynamics effects are not requested.

### 2.2.4 Electronic Structure Calculations for Semiclassical Dynamics

The necessary ingredients to carry out semiclassical dynamics simulations are energies and forces in ground and excited electronic states as well as nonadiabatic couplings, which can be obtained by two general approaches:

1. Precalculation of the energy surfaces and couplings in advance. The bottleneck of this approach is the exponential increase of the number of required single point electronic structure calculations with the number of degrees of freedom that are taken into account. As a consequence, its applicability is limited to small molecules. For larger systems, a few internal coordinates have to be selected for explicit treatment either neglecting the other ones or treating them by simplified assumptions such as coupling to heat bath modes. Alternatively, model potentials can be used.

2. Direct calculation of energies, gradients, and couplings “on the fly” at each time step of the nuclear dynamics. This requires the efficient calculation of energies and forces both for excited and ground states as well as the nonadiabatic couplings. This has been achieved in the frame of ab initio quantum chemistry using accurate wavefunction based methods such as configuration interaction (CI)[36] or CAS-SCF, which account for electron correlation.[9,11,37] Moreover, simulations based on semi-empirical methods[32,41–43] as well as recently in the frame of the time-dependent density functional theory (TDDFT) have been performed.[38,120–122] The implementation of the highly efficient linear response TDDFT nonadiabatic dynamics based on localized atomic basis sets and employing orthogonal eigenstates for the calculation of the nonadiabatic dynamics in complex systems has been developed in the frame of this thesis.[39,40]

## 2.3 Development of Nonadiabatic Dynamics in the Frame of the Time-Dependent Density Functional Theory

### 2.3.1 Representation of the Wavefunction within Linear Response TDDFT

The linear response (LR) TDDFT represents an efficient, generally applicable method for the determination of the optical properties in complex systems. Therefore, its combination with Tully's surface hopping procedure is the focus of this section. While the calculation of excited state forces in the framework of TDDFT is already a standard procedure available in many commonly used quantum chemical program packages, the calculation of nonadiabatic couplings in the frame of LR-TDDFT has been developed only in recent years.[38,93,122–125]

In this work, the nonadiabatic dynamics based on TDDFT has been formulated employing orthogonal eigenstates and localized Gaussian basis sets.[39,40] These localized basis sets are natural basis functions for the description of finite molecular systems. This approach requires the explicit calculation of nonadiabatic couplings, which have been developed in this thesis. For this purpose, an ansatz for the excited state electronic wavefunction in terms of singly excited configurations from the manifold of occupied Kohn-Sham (KS) orbitals to virtual KS orbitals is used:

$$|\psi_K(\mathbf{r};\mathbf{R}(t))\rangle = \sum_{ia} c_{ia}^K \left|\Phi_{ia}^{CSF}(\mathbf{r};\mathbf{R}(t))\right\rangle, \tag{2.16}$$

where $c_{ia}^K$ represents the configuration interaction (CI) coefficients. $\left|\Phi_{ia}^{CSF}(\mathbf{r};\mathbf{R}(t))\right\rangle$ is the singlet spin adapted configuration state function (CSF) defined as:

$$\left|\Phi_{ia}^{CSF}(\mathbf{r};\mathbf{R}(t))\right\rangle = \frac{1}{\sqrt{2}}\left(\left|\Phi_{i\alpha}^{a\beta}(\mathbf{r};\mathbf{R}(t))\right\rangle + \left|\Phi_{i\beta}^{a\alpha}(\mathbf{r};\mathbf{R}(t))\right\rangle\right). \tag{2.17}$$

$|\Phi_{i\alpha}^{a\beta}(\mathbf{r};\mathbf{R}(t))\ \rangle$ and $|\Phi_{i\beta}^{a\alpha}(\mathbf{r};\mathbf{R}(t))\ \rangle$ represent Slater determinants with single excitations from occupied orbital $i$ to virtual orbital $a$ with spin $\alpha$ or $\beta$, respectively.

The expansion coefficients $c_{ia}^K$ can be determined by requiring that the wavefunction in Eq. 2.16 gives rise to the same density response as obtained in LR-TDDFT. The change of the density is described by first order perturbation theory in LR-TDDFT according to:

$$\rho\left(\mathbf{r},t\right) = \rho_0\left(\mathbf{r}\right) + \delta\rho\left(\mathbf{r},t\right), \tag{2.18}$$

where $\rho_0$ is the unperturbed ground state density at $t = 0$. Expanding the electron density as $\rho\left(\mathbf{r},t\right) = \sum_i \left|\phi_i\left(\mathbf{r},t\right)\right|^2$ gives rise to the linear response of the density to a perturbation:

$$\rho\left(\mathbf{r},t\right) = \rho_0\left(\mathbf{r}\right) + \sum_i \left(\phi_i^*\left(\mathbf{r},t\right)\delta\phi_i\left(\mathbf{r},t\right) + \phi_i\left(\mathbf{r},t\right)\delta\phi_i^*\left(\mathbf{r},t\right)\right). \tag{2.19}$$

This can be decomposed in terms of the positive and negative frequency components as:

$$\delta\phi_i(\mathbf{r},t) = \phi_i^+(\mathbf{r})\, e^{-i\omega_K t} + \phi_i^-(\mathbf{r})\, e^{i\omega_K t} \tag{2.20}$$

with the transition frequency $\omega_K$ of the $K$'th excited state.[126] A possible choice for the representation of the response orbitals $\phi_i^+$ and $\phi_i^-$ is the expansion in terms of virtual KS orbitals $\phi_a(\mathbf{r})$:

$$\phi_i^+(\mathbf{r}) = \sum_a X_{ia}\phi_a(\mathbf{r})$$

$$\phi_i^-(\mathbf{r}) = \sum_a Y_{ia}\phi_a(\mathbf{r})\,. \tag{2.21}$$

Here, $\mathbf{X}$ and $\mathbf{Y}$ represent the solution of the TDDFT eigenvalue problem (cf. Eq. 1.3). Thus, the time-dependent electron density can be formulated as:

$$\rho(\mathbf{r},t) = \rho_0(\mathbf{r}) + \sum_{ia}(X_{ia}+Y_{ia})\phi_i(\mathbf{r})\,\phi_a^*(\mathbf{r})\, e^{-i\omega_K t} + c.c. \tag{2.22}$$

In the wavefunction picture, the time-dependent electron density $\rho(\mathbf{r},t)$ arises as a consequence of the coherent superposition of the ground and excited electronic state ($|\psi_0\rangle$ and $|\psi_K\rangle$):

$$|\psi(t)\rangle = a|\psi_0\rangle e^{-iE_0 t/\hbar} + b|\psi_K\rangle e^{-iE_K t/\hbar} \tag{2.23}$$

with the superposition coefficients $a$ and $b$. The time-dependent electron density is obtained from this wavefunction as:

$$\rho(\mathbf{r},t) = |a|^2\langle\psi_0|\hat{\rho}|\psi_0\rangle + |b|^2\langle\psi_K|\hat{\rho}|\psi_K\rangle + a^*b\sum_{ia} c_{ia}^{K*}\phi_i(\mathbf{r})\phi_a^*(\mathbf{r})e^{-i\omega_K t} + c.c.\,, \tag{2.24}$$

which can be further simplified by assuming that in the linear response regime $|a|^2 \approx 1 \gg |b|^2$:

$$\rho(\mathbf{r},t) = \rho_0 + a^*b\sum_{ia} c_{ia}^{K*}\phi_i(\mathbf{r})\phi_a^*(\mathbf{r})e^{-i\omega_K t} + c.c. \tag{2.25}$$

The direct comparison of Eq. 2.22 and 2.25 shows that the coefficients $c_{ia}^K$ are proportional to $X_{ia}+Y_{ia}$ up to a normalization constant.

In order to obtain orthogonal eigenstates, the non-Hermitian eigenvectors $\mathbf{X}$ and $\mathbf{Y}$

can be transformed using the relation:

$$\mathbf{C} = (\mathbf{A} - \mathbf{B})^{-1/2} (\mathbf{X} + \mathbf{Y}), \tag{2.26}$$

where $\mathbf{A}$ and $\mathbf{B}$ are standard TDDFT matrices.[49,91]

For non-hybrid functionals, the coefficients $c_{ia}^{K}$ giving rise to mutually orthogonal electronic states are thus given by:

$$c_{ia}^{K} = \sqrt{\frac{\epsilon_a - \epsilon_i}{\varepsilon_K}} (X_{ia} + Y_{ia}), \tag{2.27}$$

where $\epsilon_a$ and $\epsilon_i$ are the orbital energies while $\varepsilon_K$ is the transition energy of the $K'$th excited state. This choice of the expansion coefficients ensures the orthogonality of the electronic wavefunctions of Eq. 2.16, which will be employed for the calculation of the nonadiabatic couplings as outlined in the previous section.

## 2.3.2 Nonadiabatic Couplings for LR-TDDFT

In order to obtain the nonadiabatic coupling as defined in Eq. 2.14, the overlap between two CI wavefunctions at times $t$ and $t + \Delta$ is needed:

$$\langle \psi_K(\mathbf{r}; \mathbf{R}(t)) | \psi_I(\mathbf{r}; \mathbf{R}(t+\Delta)) \rangle = \sum_{ia} \sum_{jb} c_{ia}^{K*} c_{jb}^{I} \left\langle \Phi_{ia}^{CSF}(\mathbf{r}; \mathbf{R}(t)) \middle| \Phi_{jb}^{CSF}(\mathbf{r}; \mathbf{R}(t+\Delta)) \right\rangle, \tag{2.28}$$

with $c_{ia}^{K}$ defined according to Eq. 2.27. Employing Eq. 2.16 and 2.17 allows for reducing this expression to the overlap between singly excited Slater determinants:

$$\begin{aligned} &\left\langle \Phi_{ia}^{CSF}(\mathbf{r}; \mathbf{R}(t)) \middle| \Phi_{jb}^{CSF}(\mathbf{r}; \mathbf{R}(t+\Delta)) \right\rangle = \\ &\frac{1}{2} \left[ \left\langle \Phi_{i\alpha}^{a\beta}(\mathbf{r}; \mathbf{R}(t)) \middle| \Phi_{j\alpha}^{b\beta}(\mathbf{r}; \mathbf{R}(t+\Delta)) \right\rangle + \left\langle \Phi_{i\alpha}^{a\beta}(\mathbf{r}; \mathbf{R}(t)) \middle| \Phi_{j\beta}^{b\alpha}(\mathbf{r}; \mathbf{R}(t+\Delta)) \right\rangle \right. \\ &\left. + \left\langle \Phi_{i\beta}^{a\alpha}(\mathbf{r}; \mathbf{R}(t)) \middle| \Phi_{j\alpha}^{b\beta}(\mathbf{r}; \mathbf{R}(t+\Delta)) \right\rangle + \left\langle \Phi_{i\beta}^{a\alpha}(\mathbf{r}; \mathbf{R}(t)) \middle| \Phi_{j\beta}^{b\alpha}(\mathbf{r}; \mathbf{R}(t+\Delta)) \right\rangle \right], \end{aligned} \tag{2.29}$$

which can be further reduced to the overlap of molecular Kohn-Sham (KS) orbitals. In the case of the restricted KS method, the overlap between two singly excited Slater determinants can be calculated from the overlaps of spatial KS orbitals $\phi_i$ as shown on the example of the first term in Eq. 2.29:

$$\left\langle \Phi_{i\alpha}^{a\beta}(\mathbf{r};\mathbf{R}(t)) \middle| \Phi_{j\alpha}^{b\beta}(\mathbf{r};\mathbf{R}(t+\Delta)) \right\rangle =$$

$$\det \begin{bmatrix} \langle \phi_1 | \phi_1' \rangle & \cdots & \langle \phi_1 | \phi_j' \rangle & \cdots & \langle \phi_1 | \phi_n' \rangle \\ \vdots & & \vdots & & \vdots \\ \langle \phi_i | \phi_1' \rangle & \cdots & \langle \phi_i | \phi_j' \rangle & \cdots & \langle \phi_i | \phi_n' \rangle \\ \vdots & & \vdots & & \vdots \\ \langle \phi_n | \phi_1' \rangle & \cdots & \langle \phi_n | \phi_j' \rangle & \cdots & \langle \phi_n | \phi_n' \rangle \end{bmatrix} \begin{bmatrix} \langle \phi_1 | \phi_1' \rangle & \cdots & \langle \phi_1 | \phi_b' \rangle & \cdots & \langle \phi_1 | \phi_n' \rangle \\ \vdots & & \vdots & & \vdots \\ \langle \phi_a | \phi_1' \rangle & \cdots & \langle \phi_a | \phi_b' \rangle & \cdots & \langle \phi_a | \phi_n' \rangle \\ \vdots & & \vdots & & \vdots \\ \langle \phi_n | \phi_1' \rangle & \cdots & \langle \phi_n | \phi_b' \rangle & \cdots & \langle \phi_n | \phi_n' \rangle \end{bmatrix} \tag{2.30}$$

Here, the red orbitals label the position in the matrix where the occupied orbital $i$ is replaced by a virtual orbital $a$ or orbital $j$ by $b$, respectively. Analogous expressions can be derived for the other terms in Eq. 2.29. The overlaps between two KS orbitals at the time steps $t$ and $t+\Delta$ can be expressed in terms of the overlap integrals of the atomic basis functions at the corresponding time steps:

$$\left\langle \phi_i(t) \middle| \phi_j'(t+\Delta) \right\rangle = \sum_{\mu\nu} c_\mu^i(t) c_\nu^{j\,\prime}(t+\Delta) \left\langle b_\mu(\mathbf{R}(t)) \middle| b_\nu'(\mathbf{R}(t+\Delta)) \right\rangle , \tag{2.31}$$

where $c_\mu^i(t)$ and $c_\nu^{j\,\prime}(t+\Delta)$ represent the molecular orbital coefficients at times $t$ and $t+\Delta$, while $b_\mu(\mathbf{R}(t))$ and $b_\nu'(\mathbf{R}(t+\Delta))$ are localized Gaussian basis functions. Since the molecular structures at the time $t$ and $t+\Delta$ differ, the overlap of the atomic basis functions centered at different positions $\mathbf{R}(t)$ and $\mathbf{R}(t+\Delta)$ has to be calculated explicitly.

### 2.3.3 Nonadiabatic Couplings for TDDFTB

The nonadiabatic couplings in the frame of TDDFTB can be derived very similar to the TDDFT approach described in the previous section.[63] Analogously to the TDDFT case, an expression for the overlap $\langle \psi_K(\mathbf{r};\mathbf{R}(t)) | \psi_I(\mathbf{r};\mathbf{R}(t+\Delta)) \rangle$ between two CI functions at time steps $t$ and $t+\Delta$ is needed (cf. Eq. 2.28). For this purpose, 1.) the overlap matrix elements corresponding to the overlap of the two CSFs in Eq. 2.28 and 2.) the time-dependent expansion coefficients $c_{ia}^K$ are needed, which can be developed in the following way:

1. The corresponding terms to the overlap of two CSFs (cf. Eq. 2.29) can be derived analogously to the TDDFT case by replacing the matrix elements in the overlap of two singly excited Slater determinants (Eq. 2.30) by the corresponding terms in DFTB:

   $$\left\langle \phi_i \middle| \phi_j' \right\rangle \rightarrow \sum_{\mu\nu} c_\mu^i(t) S_{\mu\nu} c_\nu^{j\,\prime}(t+\Delta) . \tag{2.32}$$

   In order to calculate these DFTB matrix elements (cf. Section 1.3), the calculation of the overlap matrix $S_{\mu\nu} = \langle b_\mu(\mathbf{R}(t)) | b_\nu'(\mathbf{R}(t+\Delta)) \rangle$ has to be extended from the usual range which covers the region of typical atom-atom distances to the range of very small distances.

2. The eigenvalue equation for linear response TDDFTB has the same form as the corresponding TDDFT equation (Eq. 1.3). Therefore, the TDDFTB eigenvectors $\mathbf{X}$ and $\mathbf{Y}$ can be used analogously to TDDFT in order to obtain the time-dependent expansion coefficients as defined in Eq. 2.27.

In the case of TDDFTB, the integrals do not have to be explicitly calculated at runtime but can be used in tabulated form as usual in the DFTB procedure. Thus, the computational demand is decreased considerably allowing for the simulation of dynamics for more complex molecular systems.

## 2.4 Details of the Implementation

### 2.4.1 Initial Conditions for the Nonadiabatic Dynamics

**Wigner Distribution approach:**

The Wigner representation of quantum mechanics [127,128] provides a good starting point for the development of a semiclassical approximation to the full quantum dynamics, since it has a well-defined classical limit. The basic idea is the representation of the quantum state by a phase space Wigner distribution function: [127,128]

$$P\left(\mathbf{q},\mathbf{p}\right) = \frac{1}{\left(2\pi\hbar\right)^N}\int\left\langle \mathbf{q}-\frac{\mathbf{s}}{2}\right|\hat{\rho}\left|\mathbf{q}+\frac{\mathbf{s}}{2}\right\rangle \exp\left[-\frac{i}{\hbar}\mathbf{ps}\right]d\mathbf{s}\,, \tag{2.33}$$

where $\mathbf{q}$ and $\mathbf{p}$ denote position and momentum variables, and $\hat{\rho}$ is the quantum density operator. The Wigner function provides an exact phase space representation of quantum mechanics thus allowing for the calculation of quantum mechanical expectation values analog to the classical statistical mechanics. Within the Wigner approach, quantum phenomena can be approximately described by means of averaging over the ensemble of classical trajectories. [10,129–133] However, an important property of the Wigner function is that it can assume negative values, which does not allow its interpretation as a phase space probability distribution function. Indeed, these negative values reflect the quantum mechanical interference of probability amplitudes.

In this work, the Wigner function was utilized to sample the initial coordinates and momenta $\mathbf{q}_0$ and $\mathbf{p}_0$ for the dynamics simulations. In the harmonic approximation the canonical Wigner distribution at a given temperature involving all normal modes assumes the following form:

$$P(\mathbf{q}_0,\mathbf{p}_0) = \prod_{i=1}^{N}\frac{\alpha_i}{\pi\hbar}\exp\left[-\frac{\alpha_i}{\hbar\omega_i}(p_{i0}^2+\omega_i^2 q_{i0}^2)\right]. \tag{2.34}$$

Here, $\omega_i$ represents the frequency of the $i$'th normal mode and $\alpha_i = \tanh(\hbar\omega_i/2k_bT)$ with the Boltzmann constant $k_b$ and the temperature $T$. Since the canonical Wigner distribution function is temperature dependent, Eq. 2.34 allows for the inclusion of temperature effects to better model the experimental situation. However, due to the harmonic approximation, the Wigner distribution can be employed only for low temperatures where the anharmonicities can be neglected.

The phase space ensemble obtained by sampling the Wigner function can also be used to simulate the temperature broadened absorption spectrum according to:

$$I(E) = \int \int \sum_K \delta(E - E_K(\mathbf{q}_0)) f_K(\mathbf{q}_0) P(\mathbf{q}_0, \mathbf{p}_0) d\mathbf{q}_0 d\mathbf{p}_0 \,, \tag{2.35}$$

where $E_K$ and $f_K$ represent the transition energies and oscillator strengths, respectively.

**Long Adiabatic Trajectory at Constant Temperature:**

For high temperatures, the harmonic approximation is not valid and anharmonicities have to be taken into account. The quantum effects, however, can be neglected due to the high kinetic energy of the system. Therefore, for high temperatures the initial ensemble can be sampled along a classical molecular dynamics trajectory propagated in the ground electronic state at a constant temperature.

### 2.4.2 Propagation of the Classical Trajectories

In semiclassical dynamics, the time evolution of the nuclei is simulated by classical trajectories obtained from the solution of the Newton's equations of motion. For this purpose, the Verlet algorithm[134] is very suitable. Here, the positions $\mathbf{r}_A^{(n)}$ and velocities $\mathbf{v}_A^{(n)}$ of the nuclei are obtained recurrently from:

$$\mathbf{r}_A^{(n+1)} = \mathbf{r}_A^{(n)} + \mathbf{v}_A^{(n)}\Delta + \frac{1}{2}(\Delta)^2 \frac{\mathbf{F}_A}{m_A} \tag{2.36}$$

$$\mathbf{v}_A^{(n+1)} = \mathbf{v}_A^{(n)} + \frac{1}{2}\Delta \left[ \frac{\mathbf{F}_A^{(n)} + \mathbf{F}_A^{(n+1)}}{m_A} \right] \tag{2.37}$$

with the nuclear time step $\Delta$ and the forces $\mathbf{F}_A^{(n)}$ obtained from the gradients of the electronic structure calculation. Since the conservation of the total energy is demanded, high accuracy of the calculated forces is mandatory.

### 2.4.3 Hopping Procedure

The hopping probabilities $P_{KI}$ needed for the electronic state switching procedure are local in time, since they are proportional to the change of the electronic state populations calculated from the coefficients $C_K(t)$. In the original approach proposed by Tully in 1990,[29] the $P_{KI}$ are calculated on the nuclear dynamics timescale:

$$P_{KI}(t) = -2\Delta \frac{\mathrm{Re}\,(C_K^*(t)C_I(t)D_{KI}(t))}{|C_K(t)|^2}\,, \tag{2.38}$$

where the nuclear time step $\Delta$ is in general much larger than the timescale on which the electronic state populations change. This equation is only valid if the time step $\Delta$ and thus the change in the coefficients $C_K(t)$ is small enough to ensure that the following conditions are fulfilled:[30]

$$|C_K(t)|^2 \approx |C_K(t+\Delta)|^2 \tag{2.39}$$

$$|C_K(t+\Delta)|^2 - |C_K(t)|^2 \approx \left|\frac{d}{dt}C_K(t+\Delta)\right|\Delta\,. \tag{2.40}$$

In 1994 Hammes-Schiffer and Tully proposed an alternative method for the calculation of hopping probabilities, which allows for enlarging the nuclear time step beyond this limit.[30] According to this approach, the $P_{KI}$ are calculated as:

$$P_{KI}(t) = -2\int_t^{t+\Delta} \frac{\mathrm{Re}\,(C_K^*(\tau)C_I(\tau)D_{KI}(\tau))}{|C_K(\tau)|}d\tau\,, \tag{2.41}$$

where the numerator $\mathrm{Re}\,(C_K^*(\tau)C_I(\tau)D_{KI}(\tau))$ is numerically integrated simultaneously with the coefficients $C_K$ in Eq. 2.11. However, in the region of strong coupling, the change of the $C_K(t)$ can still give rise to unphysical hopping probabilities greater than 1. Therefore, a new scheme for calculating the hopping probabilities has been developed in this thesis, where the hopping procedure is performed at each integration step $\delta$ for the integration of the $C_K(t)$ in Eq. 2.11. The hopping probabilities $P_{KI}(t)$ for those small time steps can be calculated as:

$$P_{KI}(t) = -2\delta \frac{\mathrm{Re}\,(C_K^*(t)C_I(t)D_{KI}(t))}{|C_K(t)|^2}\,. \tag{2.42}$$

In contrast, the approaches proposed by Tully[29] and Hammes-Schiffer and Tully[30] calculate the hopping probabilities only once for each nuclear dynamics time step using Eq. 2.38 or 2.41. Since the nonadiabatic coupling $D_{KI}$ is calculated only at the midpoint $t + \Delta/2$ between two nuclear dynamics steps, $D_{KI}$ is linearly interpolated in the interval $[t, t + \Delta/2]$ and extrapolated in the interval $[t + \Delta/2, t + \Delta]$.

In Figure 2.1, the time evolution of the couplings $P_{01}$ from the originally populated state 0 to state 1 obtained with the three procedures described above are compared. The simple avoided crossing model potential from Tully,[29] which was employed for the simulations, is shown in Figure 2.1(a). In contrast to the approaches of Tully[29] and

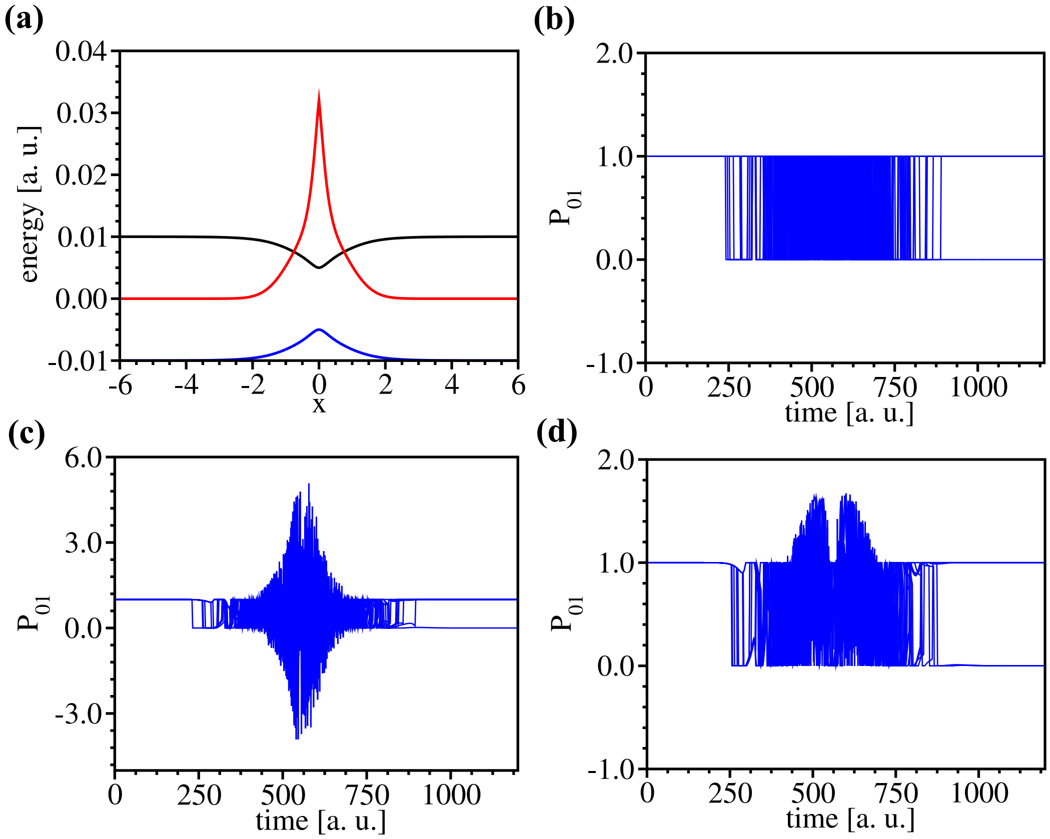

Figure 2.1: (a) Adiabatic potential energies (blue for state 0 and black for state 1) and nonadiabatic coupling strength divided by 50 (red) for the model potential from Ref. [29]. (b)-(d) Comparison of the hopping probabilities $P_{01}$ from state 0 to state 1 using potential (a) and a time step of 2 a. u. obtained (b) employing Eq. 2.42, (c) from the procedure proposed by Tully et al.,[29] and (d) from the procedure proposed by Tully and Hammes-Schiffer.[30]

Hammes-Schiffer and Tully,[30] the procedure based on Eq. 2.42 gives numerically stable results also in the case of large nuclear dynamics time steps such as the 2 a. u. employed in the example (cf. Fig. 2.1(b)-(d)). While the additional computational effort for determining the hopping probabilities at each time step during the integration (cf. Eq. 2.42) is marginal, this approach allows for the use of much larger time steps for the nuclear dynamics. Thus, the computational demand can be decreased considerably.

After a successful switch has occurred, the nuclear velocities are rescaled in order to conserve the total energy. Notice that usually velocities are rescaled parallel to the nonadiabatic coupling vector.[115] However, in the frame of the TDDFT approach as outlined in Section 2.3, the direction of the nonadiabatic coupling vector is not available and therefore uniform scaling is applied.

### 2.4.4 Implementation of Nonadiabatic Couplings

For the nonadiabatic dynamics simulation in the frame of Tully's surface hopping procedure, the time-dependent nonadiabatic couplings $D_{KI}$ which are needed for the calculation of the hopping probabilities (cf. Eq. 2.42) have to be determined in each nuclear time step according to Eq. 2.14. For this purpose, the expansion coefficients $C_K(t)$ for the electronic wavefunction (cf. Eq. 2.10 and 2.11) can be propagated by using a fourth order Runge-Kutta procedure. In order to increase the efficiency of the integration, the rapidly oscillating part of the coefficients can be eliminated by transformation of the $C_K(t)$ into the interaction representation:

$$a_K(t) = C_K(t) \exp\left[\frac{i}{\hbar}\int_{t_0}^{t} E_K\left(\mathbf{R}(\tau)\right) d\tau\right]. \tag{2.43}$$

In this representation, only the slowly varying component $a_K(t)$ remains to be calculated, for which a time step of $10^{-5}$ fs has been determined to be sufficient. Since this time step is much larger than the one necessary for the propagation of the $C_K(t)$, the computational demand can be decreased.

In order to avoid random phase variations of the nonadiabatic couplings $D_{KI}(t)$, they have to be aligned in each nuclear time step to the phases of the previous one. For this purpose, the largest elements $\langle \psi_K(\mathbf{r};\mathbf{R}(t-\Delta))\,|\psi_I(\mathbf{r};\mathbf{R}(t))\rangle$ (cf. Eq. 2.14) for each $I$ are determined, since these elements correspond to the overlap of state $I(t)$ with the state $K(t-\Delta)$ exhibiting the same character. If these largest elements are negative, all elements involving $\psi_I$ are multiplied by $-1$.

In the following section, the accuracy of the presented approach will be illustrated on the example of the nonadiabatic dynamics by the methaniminium cation $CH_2NH_2^+$. Applications to the more complex systems benzylideneaniline, furan, and pyrazine will be presented in the Chapters 4, 5, and 6, respectively.

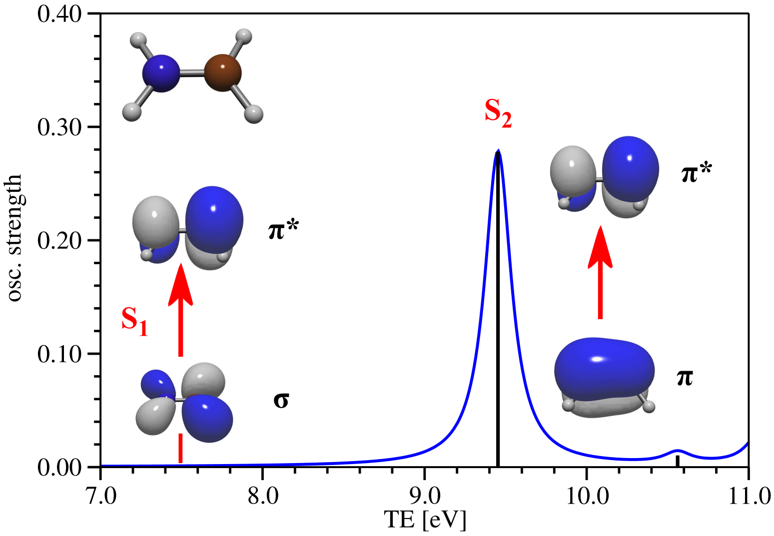

Figure 2.2: Absorption spectrum of $CH_2NH_2^+$ calculated with PBE/TZVP. The transition energy (TE) of the dark $S_1$ state is indicated by a red line and the characters of the excited states are illustrated by the dominant orbitals involved in the transition.

### 2.4.5 Test on the Photodynamics of $CH_2NH_2^+$

The accuracy of the TDDFT based nonadiabatic dynamics was tested on the photodynamics of the methaniminium cation $CH_2NH_2^+$, which is a prototype molecule for protonated Schiff-Bases.[135] $CH_2NH_2^+$ serves as a benchmark system for testing new methodologies due to its small size and thus reduced computational demands. Moreover, it represents an interesting example since the two low-lying excited states exhibit different nature: $\sigma - \pi^*$ ($S_1$) and $\pi - \pi^*$ ($S_2$), as shown in Figure 2.2.

In the absorption spectrum, the second excited state exhibits a considerably larger oscillator strength than the first excited state (cf. Figure 2.2). Photoexcitation thus promotes the system mainly into the $S_2$ state and the relaxation involves at least three states, $S_2$, $S_1$, and $S_0$, which are taken into account in the nonadiabatic dynamics simulations. The time-dependent nonadiabatic couplings $D_{2I}(t)$ from the initially excited $S_2$ state to the $S_1$ and $S_0$ state along one representative trajectory are presented in Figure 2.3(a). The time evolution of the square of electronic state coefficients $|C_K(t)|^2$ for the same trajectory is shown in Figure 2.3(b). As can be seen, strong changes of the nonadiabatic coupling $D_{21}(t)$, e.g. at $t \sim 5$ fs and $t \sim 9$ fs, induce corresponding changes in the $|C_K(t)|^2$. This results in a state switch of the trajectory from $S_2$ to $S_1$ at $t \sim 9$ fs, which corresponds to the maximum of the coupling $D_{21}(t)$ as well as to the timescale on which $|C_1(t)|^2$ is larger than $|C_2(t)|^2$. Since the coupling to the ground state $D_{20}(t)$ is very small for $t < 70$ fs, no state switch to the ground state occurs within this time period.

The time-dependent populations of the ensemble obtained either from the averaged

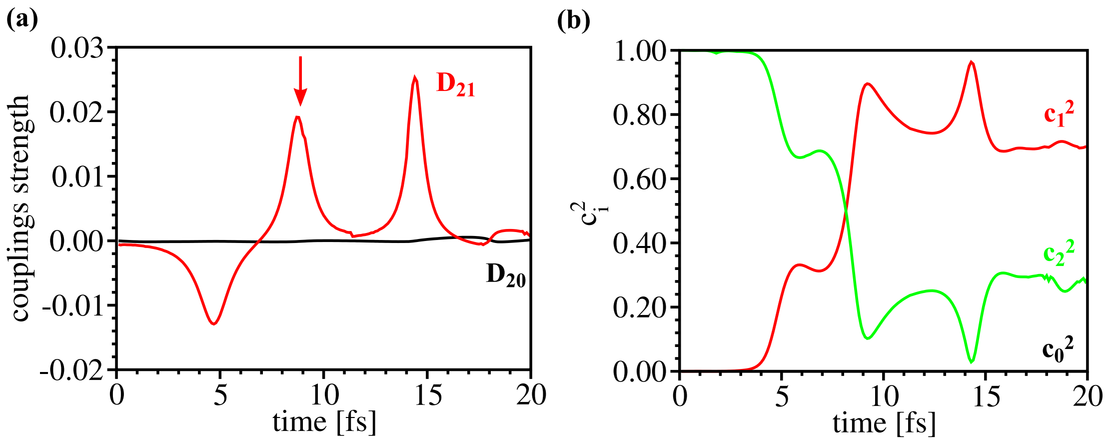

Figure 2.3: (a) Couplings $D_{2I}$ for one representative nonadiabatic trajectory from the initially populated second excited state $S_2$ to both the first excited state $S_1$ ($D_{21}$, red) and the ground state $S_0$ ($D_{20}$, black). The red arrow indicates the time step for the hopping from $S_2$ to $S_1$. (b) Time evolution of $|C_K(t)|^2$ for the same nonadiabatic trajectory.

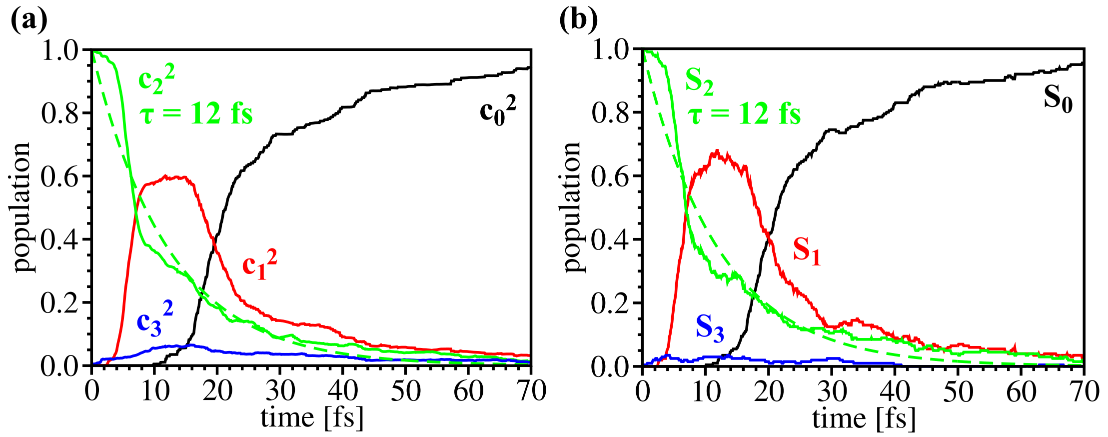

Figure 2.4: Time-dependent population of the ground state and excited states of $CH_2NH_2^+$ calculated for an ensemble of 200 nonadiabatic trajectories (a) as averaged $|C_K(t)|^2$ and (b) by monitoring the fraction of trajectories in each state as a function of time. The lifetime was determined by exponential fit to be 12 fs for both (a) and (b).

$|C_K(t)|^2$ or from the time-dependent averaged fraction of trajectories residing in each state $K$ is presented in Figure 2.4. The time evolution of the $|C_K(t)|^2$ and the corresponding fraction of trajectories as well as the lifetimes ($\tau = 12\,\mathrm{fs}$ in both cases) are in excellent agreement. Thus, the implementation of the TDDFT based nonadiabatic dynamics fulfills the condition for the TSH, that the fraction of trajectories residing in state $K$ equals the quantum probability $|C_K(t)|^2$. Moreover, the lifetime of the $S_2$ state ($\tau = 12\,\mathrm{fs}$) is in excellent agreement with the lifetime $\tau = 12 \pm 1\,\mathrm{fs}$ obtained by Barbatti et al. using TSH dynamics in the frame of the highly correlated CAS-SCF approach,[37] thus providing evidence that TDDFT describes accurately the nonadiabatic dynamics in $CH_2NH_2^+$.

Notice that recently, the accuracy of the TDDFT method for the description of nonadiabatic dynamics has also been validated against the highly correlated multi-reference ab initio methods on the example of the pyrrole molecule.[136]

# 3 Simulation of Ultrafast Observables: Time-Resolved Photoelectron Spectra

## 3.1 Introduction

The development of femtosecond laser techniques, which allows for the experimental investigation of ultrafast photoinduced processes, was pioneered by Zewail et al., as recognized in 1999 with the Nobel Prize in Chemistry.[6,12–14] These techniques have been applied to numerous problems ranging from the photodissociation dynamics of NaI[13] to studies of electron transfer in biological systems.[15,137] In general, femtosecond time-resolved methods involve a pump-probe configuration, in which a first pump pulse creates a coherent superposition of the ground and excited electronic states of the studied system. Its time evolution is subsequently monitored by processes such as absorption, fluorescence, resonant multiphoton ionization, or photoelectron spectroscopy, that are probed by a second time delayed pulse. In laser-induced fluorescence and resonant multiphoton ionization experiments, which are the standard methods for studying gas-phase clusters and molecules, the resonance of the probe pulse with an electronic transition is required. Due to significant changes of the electronic and vibrational structure during the photodynamics, this may restrict the observation of the dynamics to a limited region of the reaction coordinate.

In contrast, time-resolved photoelectron spectroscopy (TRPES) permits the investigation of dynamics along the entire reaction coordinate, since the time delayed probe pulse generates free electrons via photoionization, which is always an allowed process. Moreover, the high sensitivity of particle detectors enables gas phase experiments on systems with small quantum yields. The molecular ionization continuum permits the observation of the excited state vibrational dynamics via Franck-Condon distribution as well as the time evolution of the electronic configuration. This makes TRPES especially useful for the investigation of nonadiabatic processes.[65–69,138]

Figure 3.1 illustrates how TRPES can be used to disentangle vibrational and electronic dynamics. The pump pulse (black dashed line) induces population transfer into the bright state $a$ (red). Assuming a one-electron approximation, which implies that the cationic state is formed by a single photon ionization of a given neutral state, ionization of $a$ occurs into the $a^+$ continuum with the corresponding photoelectron band $\varepsilon_a$. Due to nonadiabatic processes, a second excited state $b$ (blue) can be populated, whose ionization into the continuum $b^+$ produces the photoelectron band $\varepsilon_b$. Thus, for a sufficiently energetic probe photon which enables the detection of both ionization channels, the nonadiabatic transition from $a$ to $b$ is expected to be reflected in the switching from ionization channel $\varepsilon_a$ to $\varepsilon_b$. This opens the perspective of simultaneously monitoring the

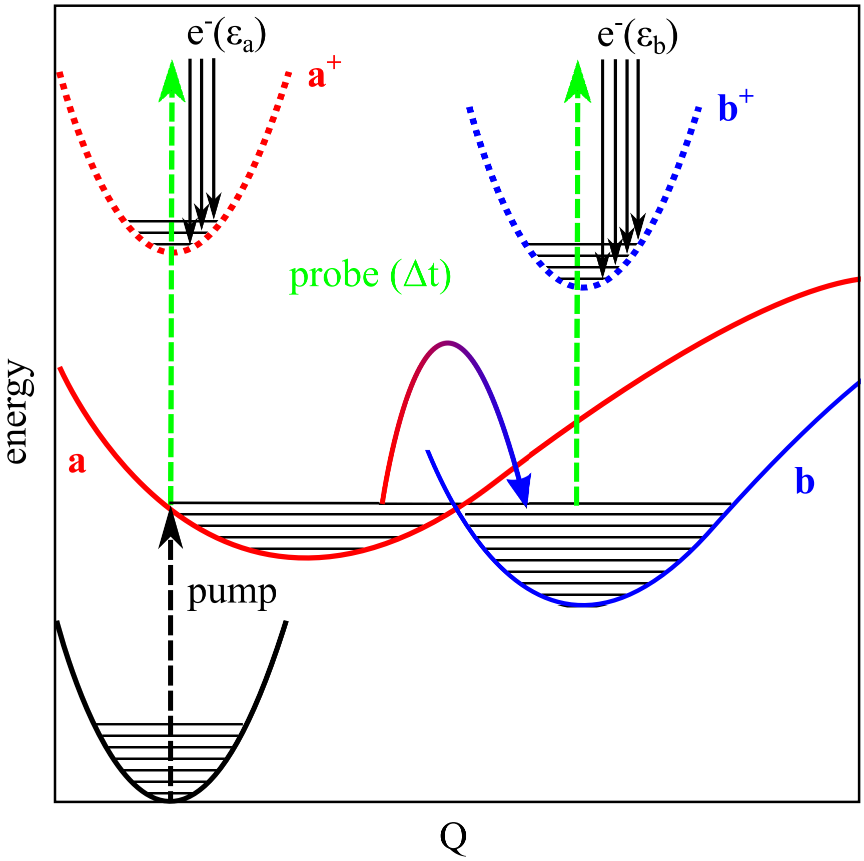

Figure 3.1: Schematic illustration for TRPES. The molecule is excited by the probe pulse (black dashed line) into the excited state $a$ (red), which can be ionized by the probe pulse (green dashed line) with the time delay $\Delta t$ into the corresponding continuum $a^+ + e^-(\varepsilon_a)$. After nonadiabatic transition to the excited state $b$ (blue) ionization by the probe pulse will occur to the corresponding continuum $b^+ + e^-(\varepsilon_b)$. The vibrational levels are indicated by horizontal black lines.

time evolution of the electronic configuration in the excited states during nonadiabatic processes and examining the nuclear vibrational dynamics via the vibrational structure within each photoelectron band (cf. Fig. 3.1).[69,139]

For cases where the neutral states ionize into the same cationic states, the disentanglement based on photoelectron kinetic energy (PKE) distribution is not possible. In such cases, the time-resolved photoelectron angular distribution (PAD) is expected to be of particular use, since it reflects the evolution of the spatial distribution of photoelectrons, which is related to the distribution of the electron in the orbital from which it was ejected. The "selection rules" for photoionization require that the product of neutral, cationic, and free electron wavefunctions and the molecular transition dipole moment contains the totally symmetric representation of the molecular point group. Since the PAD is determined by the free electron wavefunction, the electronic symmetry of the neutral state is reflected in the shape of the PAD.

TRPES experiments were first developed in the early 1980s and applied to semiconductors and surfaces.[140] In recent years, TRPES has been the subject of a number of reviews,[16,64–69] since it has been successfully used to probe excited state dynamics in a variety of systems such as organic and biochromophores,[39,75,80,81,83] metal clusters,[70–73,76,77,79] or molecular switches.[74,78,82] Simultaneously, theoretical approaches for the simulation of TRPES based on the full quantum mechanical description of nuclear motion[141–151] as well as on the semiclassical description in the frame of the Wigner distribution approach[39,40,79,84,85,152] have been developed.

In order to enable accurate simulations of TRPES for complex systems taking into account all degrees of freedom, an extension of the TDDFT nonadiabatic dynamics to the simulation of time-resolved photoionization was developed in this thesis[84] and will be presented in the following sections. For this purpose, first a general expression for the simulation of time-resolved photoionization is derived. Subsequently, the approximate description of photoionization probabilities based on both the discretized description of the electronic continuum (DC) obtained from TDDFT and the Stieltjes imaging (SI) procedure are presented. Finally, the implementation of SI in the frame of the TDDFT is outlined.

## 3.2 Derivation of an Expression for the Simulation of Time-Resolved Photoelectron Spectra

The theoretical interpretation of TRPES spectra and the exploration of underlying dynamical processes are challenging, since both nonadiabatic effects and the treatment of the photoionization continuum need to be taken into account. In order to extend the simulation of nonadiabatic dynamics outlined in Section 2 to the simulation of TRPES, the transition dipole moments to the ionization continuum have to be included, in addition to the description of the bound electronic states dynamics. For this purpose, the wavefunction can be formulated for a system containing the bound as well as the continuum states for the combined cation-free electron system:

$$\begin{aligned}\Psi\left(\mathbf{r},\mathbf{R},t\right) &= \sum_{I} \chi_I^{(N)}\left(\mathbf{R},t\right)\psi_I^{(N)}\left(\mathbf{r};\mathbf{R}\right) \\ &\quad + \sum_{K} \int dE\, \chi_K^{(N-1)}\left(\mathbf{R},t,E\right)\mathcal{A}\left[\psi_K^{(N-1)}\left(\mathbf{r};\mathbf{R}\right)\phi_K(E)\right]. \qquad (3.1)\end{aligned}$$

$\chi_I^{(N)}(\mathbf{R},t)$ and $\chi_K^{(N-1)}(\mathbf{R},t,E)$ represent the nuclear wavepackets for the bound and continuum states $I$ and $K$, respectively, where the summation extends over all singly ionized states. $\psi_I^{(N)}(\mathbf{r};\mathbf{R})$ are the adiabatic electronic wavepackets of the $N$ electron system. The antisymmetrized product $\mathcal{A}\left[\psi_K^{(N-1)}(\mathbf{r};\mathbf{R})\,\phi_K(E)\right]$ represents the combined system corresponding to the cationic state $K$ and the scattering state $\phi_K(E)$ for a photoelectron with the kinetic energy $E$.

The electronic Hamiltonian $\hat{H}_{el}^{(N)}$ for an $N$ electron system can be partitioned as:

$$\hat{H}_{el}^{(N)} = \hat{H}_{el}^{(N-1)} + \hat{T}_{el}^{(e^-)} + \hat{V}^{(e^-,N-1)}, \qquad (3.2)$$

where $\hat{H}_{el}^{(N-1)}$ is the Hamiltonian of the cationic core containing $N-1$ electrons, $\hat{T}_{el}^{(e^-)}$ is the kinetic energy operator for the photoelectron, and $\hat{V}^{(e^-,N-1)}$ is the interaction potential between the photoelectron and the cationic core.

Inserting Eq. 3.1 into the full electron-nuclear time-dependent Schrödinger equation yields a coupled set of equations for the time evolution of the continuum portion of the nuclear wavepacket for the ionized system:[141]

$$\begin{aligned}i\hbar\frac{d\chi_K^{(N-1)}\left(\mathbf{R},t,E\right)}{dt} &= \left(\hat{T} + E_K^{(N-1)} + E\right)\chi_K^{(N-1)}\left(\mathbf{R},t,E\right) \\ &\quad - \sum_{I} \vec{\varepsilon}(t)\cdot\vec{\mu}_{KI}\left(\mathbf{R},E\right)\chi_I^{(N)}\left(\mathbf{R},t\right). \qquad (3.3)\end{aligned}$$

Here, the interaction $H_{int}$ between the molecular system and the external electric field $\vec{\varepsilon}(t)$ is described as: $H_{int} = -\vec{\varepsilon}(t)\cdot\vec{\mu}$, where $\vec{\mu}$ is the dipole moment operator. The transition dipole matrix elements $\vec{\mu}_{KI}$ are accordingly defined as:

$$\vec{\mu}_{KI}\left(\mathbf{R},E\right) = \left\langle \mathcal{A}\left[\psi_K^{(N-1)}\left(\mathbf{r};\mathbf{R}\right)\phi_K(E)\right]\middle|\,\vec{\mu}\,\middle|\psi_I^{(N)}\left(\mathbf{r};\mathbf{R}\right)\right\rangle. \qquad (3.4)$$

The terms containing only transitions among cationic states or among free electron states have been neglected in Eq. 3.3. In order to connect Eq. 3.3 with the nonadiabatic dynamics outlined in Chapter 2, a semiclassical approximation related to Tully's original procedure[31] has been introduced, thus yielding a coupled set of equations for the time evolution of the coefficients $c_K^{(N-1)}$:[152]

$$i\hbar \frac{dc_K^{(N-1)}(t,E)}{dt} = \left(E_K^{(N-1)} + E\right) c_K^{(N-1)}(t,E) - \sum_I \vec{\varepsilon}(t) \cdot \vec{\mu}_{KI}(\mathbf{R},E)\, c_I^{(N)}(t)\,. \tag{3.5}$$

This formulation can be utilized for the simulation of photoionization in the frame of the nonadiabatic semiclassical dynamics for arbitrary pulse shapes. For this purpose, the time-dependent Schrödinger equation for bound states as developed in Chapter 2 (cf. Eq. 2.11) can be augmented by Eq. 3.5 in order to describe the ionization continuum. It should be emphasized that this approach provides a general framework for the simulation of time-dependent photoionization based on classical trajectories. If Gaussian laser pulses with weak intensities are employed, the perturbation theory limit of this approach is equivalent to the analytic formulation derived in Reference [130].

The intensity of the TRPES signal for the pump-probe time delay $t_D$ at a particular value of the photoelectron kinetic energy $E$ is obtained from the coefficients $c_K^{(N-1)}$ by averaging over the whole ensemble of $n_{traj}$ independently propagated trajectories according to:

$$S_{TRPES}(t_D,E) = \frac{1}{n_{traj}} \sum^{n_{traj}} \sum_K \left| c_K^{(N-1)}(t \rightarrow \infty, E) \right|^2. \tag{3.6}$$

Due to the classical description, the quantized vibrational degrees of freedom have not been taken into account, which implies the assumption that the vibrational energy does not change upon ionization.

An expression for the TRPES signal, taking into account that the energy of the probe pulse can be partly transformed into kinetic energy of the cationic species, can be derived by projecting Eq. 3.3 onto a set of orthogonal vibrational eigenstates $|\nu_K\rangle$ leading to:

$$\begin{aligned} i\hbar \frac{dc_{K,\nu}^{(N-1)}(t,E)}{dt} &= \left(E_{K,0}^{(N-1)} + E_{\nu_K}^{(N-1)} + E\right) c_{K,\nu}^{(N-1)}(t,E) \\ &\quad - \sum_I \vec{\varepsilon}(t) \left\langle \nu_K \left| \vec{\mu}_{KI}(\mathbf{R},E) \right| \chi_I^{(N)}(\mathbf{R},t) \right\rangle. \end{aligned} \tag{3.7}$$

Here $c_{K,\nu}^{(N-1)}(t,E)$ are the vibrational expansion coefficients, $E_{K,0}^{(N-1)}$ is the electronic energy of the cationic state $K$ in the vibrational ground state, and $E_{\nu_K}^{(N-1)}$ is the corresponding vibrational energy. Within the classical approximation, the neutral state wavepacket $\chi_I^{(N)}(\mathbf{R},t)$ is approximated by a spatially localized delta function. Thus, $\vec{\mu}_{KI}(\mathbf{R},E)$ can be replaced by the transition dipole moments evaluated at the position of the nuclear trajectory $\mathbf{R}(t)$. For the probe pulse, a Gaussian shape is employed:

$$\vec{\varepsilon}(t) = \frac{\vec{\varepsilon}_0}{\sigma_{pr}\sqrt{2\pi}} \exp\left[-\frac{(t-t_D)^2}{2\sigma_{pr}^2}\right] \exp\left[-\frac{iE_{pr}}{\hbar}(t-t_D)\right], \tag{3.8}$$

where $\vec{\varepsilon}_0$ is the pulse amplitude, $\sigma_{pr}$ is the temporal width of the probe pulse, and $E_{pr}$ is the pulse energy. In the limit of low pulse intensity, a perturbative expansion can be performed in order to derive an analytic expression for the TRPES signal. Assuming that the sum of the electronic and vibrational energy $E_{K,0}^{(N-1)} + E_{\nu_K}^{(N-1)}$ can be approximated by the total energy of the classical system given by $E_{K,0}^{(N-1)}(\mathbf{R}(t)) + E_{K,vib}^{(N-1)}$, the final expression for the calculation of the TRPES signal can be derived as:[152]

$$\begin{aligned} S_{TRPES}(t_D, E) = &\frac{1}{n_{traj}} \sum^{n_{traj}} \sum_{IK} \int_0^\infty dE_{K,vib}^{(N-1)} \\ \times &\int_{-\infty}^{\infty} d\tau \exp\left[-\frac{(\tau-t_D)^2}{2\sigma_{pr}^2}\right] \left|F_{KI}\left(E_{K,vib}^{(N-1)}\right)\right|^2 \left|\vec{\mu}_{KI}\left(\mathbf{R}(\tau), E\right)\right|^2 \\ \times \exp&\left[\frac{-\sigma_{pr}^2}{\hbar^2}\left(E_{pr} - \left(E_{K,0}^{(N-1)}(\mathbf{R}(\tau)) + E_{K,vib}^{(N-1)} - E_{I,0}^{(N)}(\mathbf{R}(\tau)) - E_{I,vib}^{(N)}\right) - E\right)^2\right]. \end{aligned} \tag{3.9}$$

The integration of Eq. 3.9, which provides an expression for the TRPES spectrum, can be carried out explicitly if the Franck-Condon factors $F_{KI}$ as well as the transition dipole moments $\vec{\mu}_{KI}$ are available. In the following section, two approximate descriptions for the transition dipole moments will be presented, which can be employed for the simulation of TRPES spectra.

## 3.3 Approximate Description of Photoionization Probabilities

For the simulation of time-resolved photoelectron spectra, an approximate description for the transition dipole moments to the cationic continuum is mandatory:

$$\vec{\mu}_{KI}\left(\mathbf{R}(t), E\right) = \left\langle \mathcal{A}\left[\psi_K^{(N-1)}\left(\mathbf{r};\, \mathbf{R}(t)\right)\phi_K(E)\right]\right| \vec{\mu} \left|\psi_I^{(N)}\left(\mathbf{r}; \mathbf{R}(t)\right)\right\rangle. \tag{3.10}$$

In order to account for the continuous kinetic energy spectrum of the emitted photoelectrons, various approximations[143,144,153] as well as exact numerical discretization schemes[141,142] have been developed.

Since TDDFT offers the possibility to treat complex molecular systems, the development of a TDDFT based description of the ionization probabilities is highly desirable. Therefore, an approximate description of transition dipole moments for photoionization in the frame of TDDFT as well as its combination with the Stieltjes imaging procedure were developed in this thesis.

### 3.3.1 Discretized Description of the Electronic Continuum Based on TDDFT

The electronic continuum can be approximated by a discretized description using a finite set of eigenstates, which can be obtained e.g. by TDDFT. These states do not have the correct continuum distribution, but can be used to obtain approximate transition energies and oscillator strengths.[154] Notice that this kind of description strongly depends on the quality of the basis set employed for the representation of the electronic orbitals. The transition energies and transition dipole moments needed for the discretized description of the electronic continuum can be obtained from TDDFT using CI-like wavefunctions for the excited electronic states of the neutral species, analogous to the ansatz for the nonadiabatic dynamics (cf. Eq. 2.16 in Section 2.3). For this purpose, transition dipole moments among excited states were developed in this work, which are not available in standard TDDFT procedures.[84]

Within this ansatz, the transition dipole matrix elements $\vec{\mu}_{IK}$ between two excited states $I$ and $K$ can be calculated according to:

$$\vec{\mu}_{IK} = \left\langle \psi_I \left| \vec{\mu} \right| \psi_K \right\rangle = \sum_{ia} \sum_{jb} c_{ia}^{I*} c_{jb}^{K} \left\langle \Phi_{ia}^{CSF}(\mathbf{r};\mathbf{R}(t)) \left| \vec{\mu} \right| \Phi_{jb}^{CSF}(\mathbf{r};\mathbf{R}(t)) \right\rangle , \tag{3.11}$$

where $a$ and $b$ indicate virtual while $i$ and $j$ denote occupied orbitals. The dipole matrix elements on the right hand side of Eq. 3.11 can be reduced to the transition dipoles between Kohn-Sham orbitals applying the standard Slater-Condon-Rules for matrix elements of one-electron operators.[155] The KS orbitals can be expanded in a Cartesian Gaussian basis set with the basis functions $b_\nu(\mathbf{A}, \alpha, l, m, n)$ given by:

$$b_\nu(\mathbf{A}, \alpha, l, m, n) = N(x - x_A)^l (y - y_A)^m (z - z_A)^n \exp[-\alpha r_A^2], \tag{3.12}$$

where $N$ is a normalization constant, $x_A$, $y_A$, and $z_A$ are the Cartesian coordinates for the center $\mathbf{A}$ of $b_\nu$. $l$, $m$, and $n$ are integers, while $\alpha$ is the orbital exponent. Employing these functions, the matrix elements between two KS orbitals can be further reduced to the sum of dipole matrix elements between Gaussian basis functions:

$$\left\langle \phi_i \left| \vec{\mu} \right| \phi_j \right\rangle = \sum_{\mu=1}^{n} \sum_{\nu=1}^{n} c_\mu^i c_\nu^j \left\langle b_\mu \left| \vec{\mu} \right| b_\nu \right\rangle \tag{3.13}$$

with the KS orbital coefficients $c_\mu^i$. The matrix element $\langle b_\mu | \, \vec{\mu} \, | b_\nu \rangle$ for the $x$-component of $\vec{\mu} = \hat{x}\vec{e}_i + \hat{y}\vec{e}_j + \hat{z}\vec{e}_k$ is given by:

$$\left\langle b_\mu(l') \, | \hat{x} \, | b_\nu(l) \right\rangle = \left\langle b_\mu(l') \, | b_\nu(l+1) \right\rangle + x_A \left\langle b_\mu(l') \, | b_\nu(l) \right\rangle . \tag{3.14}$$

An analogous expression can be obtained for the $y$- and $z$-components of $\vec{\mu}$. Notice that the calculation of the transition dipole moments between excited states within the random phase approximation (RPA), which has been developed by Yeager et al.,[156] is related to the TDDFT based formalism.

### 3.3.2 Stieltjes Imaging Procedure

The Stieltjes imaging procedure can be employed in order to describe accurately the photoionization process. The method avoids the extremely demanding solution of the scattering problem for the electronic continuum functions.[157,158] This is achieved by reconstructing the photoionization spectrum from the so-called spectral moments. These spectral moments can be either calculated from discrete states obtained by diagonalization of the full Hamiltonian matrix or by using some approximate approach for the calculation of the spectral moments as shown e.g. by Gokhberg et al.[159]

In general, the interaction of unpolarized electric dipole radiation with an atom or molecule can be described starting from the Kramers-Heisenberg expression of the polarizability $\alpha$ as a function of the complex frequency $z$:[160–162]

$$\alpha(z) = \int_0^\infty \frac{df(\epsilon)}{\epsilon^2 - z^2}\,, \tag{3.15}$$

where $\alpha(z)$ is defined as the Stieltjes integral over the oscillator strength distribution $df(\epsilon)$. In the above equation, $\epsilon$ is an transition energy and $df(\epsilon)$ is defined as:

$$df(\epsilon) = \sum_i^\infty \left(f_i\, \delta\left(\epsilon - \epsilon_i\right) + g(\epsilon)\right) d\epsilon\,, \tag{3.16}$$

containing both the contributions from the discrete and the continuous part of the electronic spectrum. Here, $g(\epsilon)$ is the density of continuum states and $\epsilon_i$ are discrete transition energies with the corresponding oscillator strengths $f_i$. Thus, $\alpha$ can be reformulated as:

$$\alpha(z) = \sum_i^{discrete} \frac{f_i}{\epsilon_i^2 - z^2} + \int_{\epsilon_0}^\infty \frac{g(\epsilon)d\epsilon}{\epsilon^2 - z^2}\,, \tag{3.17}$$

where $\epsilon_0$ is the beginning of the ionization continuum. The ionization cross section $\sigma(\omega)$, which reflects the frequency-dependent ionization probability, can be calculated from the imaginary part of $\alpha$ for real values $\omega$ of the frequency or from the density of continuum states according to:

$$\sigma(\omega) = \frac{4\pi\omega}{c}\mathrm{Im}\left(\alpha(\omega)\right) = \frac{2\pi}{c} g(\omega), \tag{3.18}$$

where $c$ is the speed of light.

In the Stieltjes imaging method as originally proposed by Langhoff et al.,[157,158] $g(\omega)$ was approximated by a histogram representation. Following this approach, $\alpha$ can be expanded into a series using the mathematical theory of moments:[163]

$$\alpha(z) = \sum_{k}^{\infty} S(-2k) z^{2k-2}\,, \tag{3.19}$$

where $S(-k)$ are the negative power spectral moments:

$$S(-k) = \sum_{i=1}^{discrete} \frac{f_i}{(\epsilon_i)^k} + \int_{\epsilon_0}^{\infty} \frac{g(\epsilon)d\epsilon}{\epsilon^k}\,. \tag{3.20}$$

The moments $S(-k)$ should converge to the correct limit of $\alpha$ when the variational procedures for the calculation of $\epsilon_i$ and $f_i$ are improved. The pseudo spectra with $n$ pairs of values $\left(\widetilde{\epsilon}_i, \widetilde{f}_i\right)$, which provide an approximation to the ionization spectrum of the real system, can then be constructed from the $2n$ moments using several algorithms.[164]

In this work, the relation between the Stieltjes integral $\beta(z)$ and the spectral moments $S(-k)$:

$$\beta(z) = \int_{\epsilon_0}^{\infty} \frac{\epsilon\, g(\epsilon)d\epsilon}{\epsilon - z} = \sum_{k=1}^{l} S(-k) z^{(k-1)} \tag{3.21}$$

is utilized.[165] This allows for including even and odd moments into the expansion, while the expansion based on $\alpha(z)$ contains only the even moments (cf. Eq. 3.19). Since this representation is divergent above $\epsilon_0$, an analytic continuation has to be performed for the calculation of $\beta(z)$ in the continuum part of the spectrum. Therefore, the Padé-approximation[154] is introduced:

$$\sum_{k=1}^{l} S(-k) z^{(k-1)} \approx \frac{P_{n-1}(z)}{Q_n(z)}\,. \tag{3.22}$$

To obtain an accurate representation of $\beta(z)$, a large number of spectral moments has to be calculated with high numerical precision. Afterwards, the pseudo ionization energies $\widetilde{\epsilon}_i$ are obtained as the real roots of the polynomial $Q_n(z)$ and the corresponding pseudo oscillator strengths $\widetilde{f}_i$ are gained from the residues of the Padé-approximant for $z \to \widetilde{\epsilon}_i$:

$$\widetilde{f}_i = \frac{-1}{\widetilde{\epsilon}_i} \lim_{z \to \widetilde{\epsilon}_i} (\widetilde{\epsilon}_i - z) \frac{P_{n-1}(z)}{Q_n(z)} = \frac{-1}{\widetilde{\epsilon}_i} \frac{P_{n-1}(\widetilde{\epsilon}_i)}{Q_n{}'(\widetilde{\epsilon}_i)}\,. \tag{3.23}$$

Here, $Q_n{}'(\widetilde{\epsilon}_i)$ is the derivative of the polynomial $Q_n(z)$ with respect to the transition energies. Notice that for the determination of the roots, high numerical accuracy beyond the double precision level is required.

The pseudo energies $\widetilde{\epsilon}_i$ and pseudo oscillator strengths $\widetilde{f}_i$ obtained this way combined with the nonadiabatic dynamics "on the fly" allow for the simulation of TRPES spectra in complex systems. For this purpose, the nonadiabatic dynamics is simulated as outlined in Chapter 2. Subsequently, the ionization spectrum can be approximated by the Stieltjes imaging pseudo spectrum for selected time steps in the nuclear dynamics.[84]

### 3.3.3 Implementation and Tests of the Stieltjes Imaging Procedure

In order to provide an adequate accuracy for the Stieltjes imaging procedure, a careful computational implementation is necessary, since the procedure exhibits serious numerical difficulties. As stated by Langhoff,[158] a sufficient number of spectral moments $S(-k)$ has to be employed for a smooth representation of the pseudo spectrum. However, the polynomials $P_{n-1}(z)$ and $Q_n(z)$ (cf. Eq. 3.22) constructed from a high number of spectral moments are numerically difficult to treat. Tests performed in the frame of this thesis showed that the standard accuracy for computational calculations of double precision is not sufficient for this purpose, in particular for determination of the roots of the polynomial $Q_n(z)$. Therefore, the infinite precision library CLNUM, which provides exact rationals and the opportunity to calculate floating points with a defined precision, has been implemented for the treatment of $P_{n-1}(z)$ and $Q_n(z)$.

The numerical accuracy for the implementation of the SI procedure was tested on the model system for the negative hydrogen ion.[166,167] Within this model, the analytic expression for the normalized oscillator strength distribution $g$ and the associated cumulative oscillator strength distribution $f$ are given as:[158,165]

$$g(\varepsilon) = \frac{8}{3\pi}\left(\frac{\sqrt{\varepsilon-1}}{\varepsilon}\right)^3, \qquad 1 \leq \varepsilon \leq \infty \tag{3.24}$$

$$f(\varepsilon) = \frac{2}{\pi}\left[\frac{\sqrt{\varepsilon-1}}{3}\left(\frac{2}{\varepsilon^2}-\frac{5}{\varepsilon}\right) + \arctan(\sqrt{\varepsilon-1})\right], \tag{3.25}$$

where $\varepsilon$ is the dimensionless frequency $\varepsilon = \omega/(0.0277\ \mathrm{a.u.})$. The spectral moments for the SI procedure (cf. Eq. 3.22) can be derived as:[158,165]

$$S(-k) = \frac{2^{1-2k}\,(2k)!}{k!\,(k+2)!}, \quad k = 0, 1, \ldots \tag{3.26}$$

In Figure 3.2, the $f(\varepsilon)$ and $g(\varepsilon)$ that were obtained from the current implementation of the SI procedure employing 100 spectral moments as described above, are compared with the results from the analytic formulation in Eq. 3.24 and 3.25. The good agreement of the results provides confidence for the numerical accuracy of the SI implementation.

In order to test the combination of the SI approach with TDDFT for the calculation of $\epsilon_i$ and $f_i$, the photoionization spectrum of the theoretically and experimentally well investigated benzene molecule was simulated. The energies and oscillator strengths for the calculation of the spectral moments were obtained from TDDFT employing the B3LYP functional[88,169] and 6-311++G** atomic basis sets.[88,169] The comparison of the calculated photoionization cross section both with SI results of Gokhberg et al.,[159] based on the representation of the molecular Hamiltonian with a second order algebraic

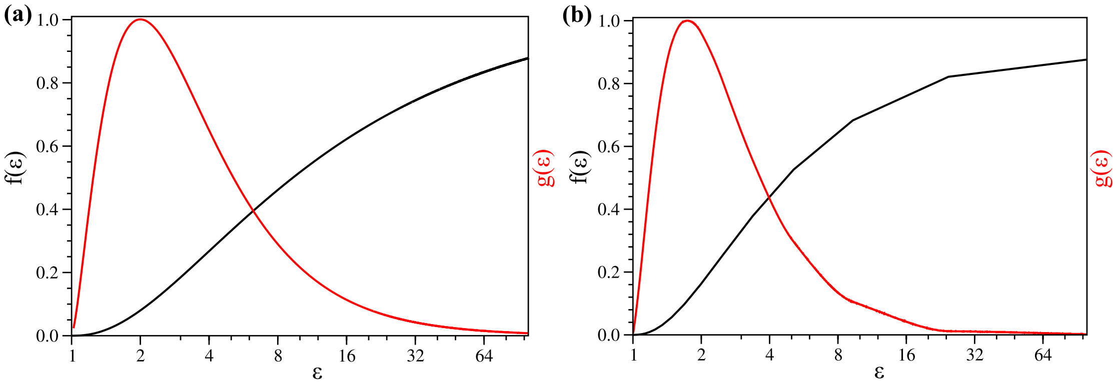

Figure 3.2: Normalized oscillator strength distribution $g(\varepsilon)$ (red) and associated cumulative oscillator strength distribution $f(\varepsilon)$ (black) for the H ion obtained from (a) model ionic system[166,167] and (b) from the Stieltjes imaging approach using 100 moments.

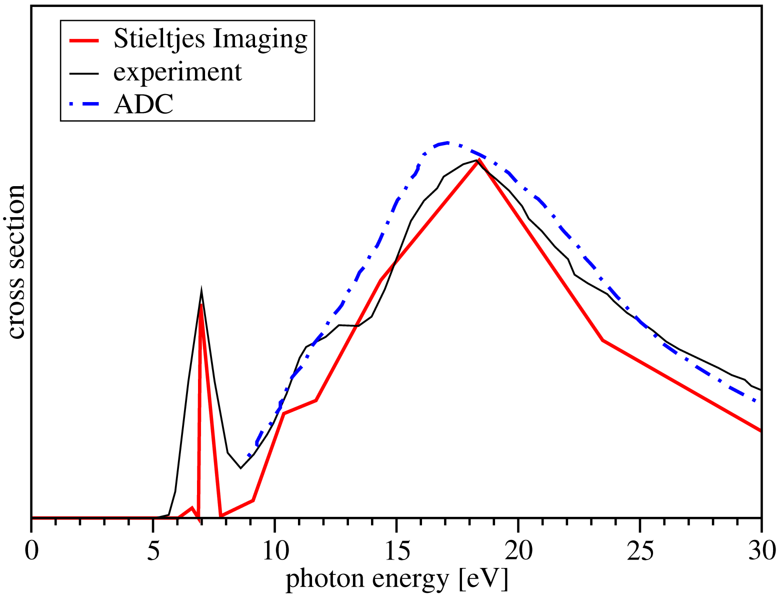

Figure 3.3: Comparison of the photoionization cross section for benzene obtained from Stieltjes Imaging (red), algebraic diagrammatic constructions (ADC)[159] (blue, dashed), and experiment[168] (black).

diagrammatic construction (ADC) scheme, and with experimental results from Feng et al.,[168] is presented in Figure 3.3. As can be seen, the results are in good agreement thus providing evidence for the accuracy of the presented SI procedure.

The results for the simulation of the time-resolved photoionization spectrum of pyrazine obtained with the described approaches (DC and SI) and their excellent agreement with recent experimental findings will be presented in Chapter 6.

# Part II

# Applications

# Introduction

The scope of the theoretical methods developed in Part I will be demonstrated on several examples in the following chapters. The theoretical results obtained in this work lead to new insights into the mechanisms of ultrafast nonadiabatic processes in important organic molecules and biochromophores.

As a first application, the ultrafast dynamics of photoswitching processes will be investigated on the example of the benzylideneaniline (BAN) molecule in Chapter 4. Furthermore, the time-resolved photoelectron spectrum will be predicted. The presented theoretical results serve to stimulate recent experimental investigation of the photoinduced isomerization processes in derivatives of BAN.

The time-dependent photoionization processes in furan and pyrazine will be explored in Chapters 5 and 6. For these molecules, TRPES and time-resolved photoelectron imaging (TRPEI) experiments with high resolution are available. The presented theoretical simulations provide for the first time an interpretation of the experimental findings. Moreover, the agreement with the experimental results demonstrates the accuracy of the developed theoretical methods. The TRPES spectrum of pyrazine will be used to demonstrate that inclusion of the ionization probabilities is mandatory for an accurate simulation of time-resolved photoionization processes.

Representing chromophores in a solvated environment, microsolvated adenine will be studied in Chapter 7. The simulation of the relaxation dynamics in microsolvated adenine and the comparison to adenine in the gas phase allow for the first time to determine the influence of solvent on the photoinduced relaxation process in adenine.

# 4 Ultrafast Photoisomerization in Benzylideneaniline

## 4.1 Introduction

Benzylideneaniline (BAN) serves as a prototype for molecular switch Schiff bases, which are of great interest in many fields of chemistry and biochemistry.[170–172] The azomethine group (–CH=N–), that is also present in rhodopsin, plays a central role in the light-driven proton pump process occurring during the visual cycle.[170,171,173] Therefore, the photochemistry of this group has been extensively studied in the past.[174] Although BAN is structurally similar and isoelectronic with stilbene and azobenzene, the ultraviolet spectrum of BAN is remarkably different.[175] According to experimental[176,177] and theoretical studies,[178–180] the main reason for this difference is the non-planar conformation of BAN compared to the nearly planar structures of stilbene and azobenzene. The investigation of the ultrafast photoisomerization in BAN is of particular interest in context of applications of molecular switches in molecular electronics and biosensoring. In contrast to stilbene and azobenzene, which have been intensively investigated theoretically as well as experimentally,[34,74,181–188] the photodynamics of benzylideneaniline has been studied for the first time in the frame of this thesis.[40]

The chapter is structured as follows: First, the computational aspects are shortly outlined followed by the investigation of the structures for cis and trans isomers of BAN and their stationary absorption spectra. Subsequently, the nonradiative lifetime of the

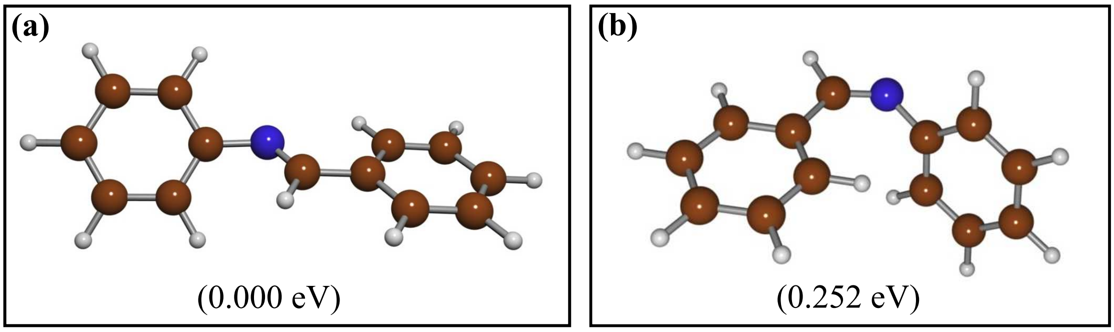

Figure 4.1: Equilibrium structures for (a) the trans and (b) the cis isomer of BAN optimized with the PBE functional and the TZVP basis set. Carbon atoms are indicated by brown color, hydrogen atoms by white, and nitrogen atoms by blue. The relative energies of the isomers are given in parenthesis.

optically allowed $S_1$ state of the trans isomer is determined from the nonadiabatic dynamics simulations. The investigation of the mechanism of the ultrafast photoinduced switching in BAN will allow fundamental insight into the selectivity and dynamics of molecular switches. Finally, the simulated time-resolved photoelectron spectrum is presented. Since in photoionization usually several cationic excited states can be reached, the influence of a manifold of cationic excited states on the general appearance of the TRPES is also investigated.

## 4.2 Computational Methods

The photodynamics of benzylideneaniline was simulated employing the TDDFT nonadiabatic dynamics approach, which has been presented in Chapter 2. For this purpose, the energies, forces, and the nonadiabatic couplings were calculated with the gradient corrected Perdew-Burke-Ernzerhof (PBE) exchange-correlation functional [189] as implemented in the Turbomole [96] program package in combination with the triple-$\zeta$ valence plus polarization (TZVP) atomic basis set. [190] In order to speed up the calculations, the Resolution-of-the-Identity (RI) approximation [191,192] was employed.

The accuracy of PBE for the description of the low-lying excited states of BAN was investigated by comparing the calculated stationary absorption spectra for the cis and trans isomers with those obtained with the hybrid B3LYP [88,169] functional as well as with experimental measurements (cf. Section 4.3). Furthermore, nonadiabatic dynamics simulations were performed using both the B3LYP and the PBE functional for a small number of trajectories in order to examine the influence of the functional. The results show that the features of the excited state dynamics are not strongly dependent on the choice of the functional. Since the RI approximation is only available for non-hybrid DFT functionals, the more efficient non-hybrid PBE functional was employed for the dynamics simulations.

The nonadiabatic dynamics was simulated in a manifold consisting of the ground electronic state and the two lowest electronically excited states. For this purpose, an ensemble of 220 trajectories was generated and excited to the $S_1$ state. The initial coordinates and momenta were sampled from an 18 ps trajectory propagated in the ground electronic state at a constant temperature of 100 K for the trans isomer. For the calculation of the nuclear dynamics, the classical Newton's equations of motion were integrated using the velocity Verlet algorithm with a time step of 0.1 fs. In the case that a crossing of the ground state and the first excited state occurred during the dynamics, the trajectory was forced to switch to the ground state.

For the simulation of the time-resolved photoelectron spectrum of BAN, only photoionization to the cationic ground electronic state $D_0$ was considered, since it can be effectively reached both from the ground state and from the excited states of the neutral species. Furthermore, constant Franck-Condon factors and constant transition dipole moments were assumed for photoionization. Within these approximations, the TRPES spectrum can be simulated in the frame of the Wigner distribution approach. For this purpose, the equation for the zero kinetic energy (ZEKE) pump-probe signals (cf. Ref. [133]) is modified by taking into account that a part of the probe-pulse energy $E_{pr}$ changes into kinetic energy of the photoelectrons $E$:[40,79]

$$
\begin{aligned}
S(t_D, E) \sim \int\!\!\int d\mathbf{q}_0 d\mathbf{p}_0 \int_0^\infty d\tau_1 \exp\left\{-\frac{(\tau_1 - t_D)^2}{\sigma_{pu}^2 + \sigma_{pr}^2}\right\} \\
\times \exp\left\{-\frac{\sigma_{pr}^2}{\hbar^2}\left[E_{pr} - V_{21}\left(\mathbf{q}_1\left(\tau_1; \mathbf{q}_0, \mathbf{p}_0\right)\right) - E\right]^2\right\} \\
\times \exp\left\{-\frac{\sigma_{pu}^2}{\hbar^2}\left[E_{pu} - V_{10}\left(\mathbf{q}_0\right)\right]^2\right\} P_{00}(\mathbf{q}_0, \mathbf{p}_0). \qquad (4.1)
\end{aligned}
$$

In this equation, $\sigma_{pu}$ ($\sigma_{pr}$) and $E_{pu} = \hbar\omega_{pu}$ ($E_{pr} = \hbar\omega_{pr}$) are the pulse durations and transition energies for the pump and probe pulse, respectively, with time delay $t_D$. $V_{21}(\mathbf{q}_1(\tau_1; \mathbf{q}_0, \mathbf{p}_0))$ labels the time-dependent energy gap between the cationic state and the neutral state obtained from the nonadiabatic dynamics. The TRPES spectrum is calculated by averaging over the ensemble of trajectories employing the analytical expression in Eq. 4.1. In order to examine the influence of higher cationic states on the appearance of the TRPES spectrum, simulations for selected individual trajectories including an additional eleven cationic excited states were performed.

## 4.3 Structural and Electronic Properties

The stationary absorption spectrum of benzylideneaniline differs from those of the related molecules azobenzene and stilbene. This has led to a great number of theoretical and experimental studies in the past decades.[175–180,193–197] This discrepancy is attributed to the differences in the structural properties: In contrast to stilbene and azobenzene, BAN does not exhibit a planar equilibrium geometry.[178,198] This can be seen from Figure 4.1(a), which shows the optimized structure of trans-BAN as obtained from DFT (PBE/TZVP). The dihedral angle of the phenyl ring bound to the carbon atom is almost coplanar with the C=N bond, while the dihedral angle of the second phenyl ring exhibits a value of 42°, resulting in the nonplanar overall geometry of BAN. These calculated values are in good agreement with experimental gas phase electron diffraction measurements.[178]

The optimized structure for the cis isomer of BAN, which lies 0.252 eV higher in energy, is shown in Figure 4.1(b). In this isomer, the phenyl ring bound to the carbon atom is almost coplanar with a small torsion angle of 14° with respect to the C=N bond, while the second phenyl ring is tilted by 76°. Since the cis isomer is the product of the photoisomerization, its thermal stability was examined by propagating a 10 ps molecular dynamics trajectory in the electronic ground state employing the PBE functional at a constant temperature of $T = 200\,\mathrm{K}$. Within the simulation period no isomerization occurred, indicating that the cis-BAN is thermally stable well above the usual temperature of e.g. molecular beam experiments. Therefore, the trans-cis photoisomerization in BAN

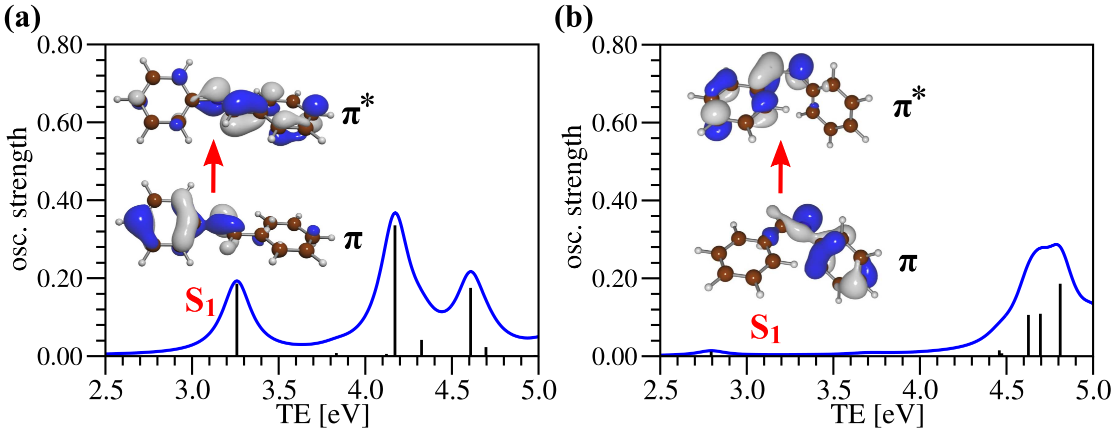

Figure 4.2: Theoretical stationary absorption spectrum for (a) the trans isomer and (b) the cis isomer of BAN calculated with the PBE functional combined with the TZVP basis sets. The discrete transitions were convoluted with a Lorentzian function of 0.2 eV width. The character of the $S_1$ state is indicated by the dominant KS orbitals involved in the transition.

should be observed in experiments.

The stationary absorption spectra for both isomers calculated with the PBE functional are presented in Figure 4.2. The lowest intense electronic transition of the trans isomer labeled by $S_1$ is centered at 3.26 eV and has dominantly $\pi - \pi^*$ character. The second excited state ($S_2$), which also exhibits $\pi - \pi^*$ character, is a dark state located at 3.83 eV. Thus, trans-BAN is expected to be excited mainly into the $S_1$ state. The first intense transition in the cis isomer featured in panel (b) is located at 4.5 - 5.0 eV and lies much higher in energy than the optical absorption of the trans isomer. Therefore, both isomers can be selectively excited, which is a necessary requirement for reversible photoswitching.

In order to determine the accuracy of the PBE functional for the description of the excited states of trans-BAN, a comparison with both the hybrid B3LYP functional and experimental results is presented in Table 4.1. As can be seen, the transition energy for the $S_1$ state obtained from the PBE functional is lower by $\sim 0.4$ eV with respect to the B3LYP results and lower by $\sim 0.8$ eV in comparison with the experiment.[175,195] However, with both theoretical methods, the characters of the $S_1$ and $S_2$ transitions ($\pi - \pi^*$) are identical and no additional dark states appear below the $S_2$ state.

Due to the well known problem of TDDFT in describing long-range interactions, especially for non-hybrid functionals, the characters of the $S_1$ and $S_2$ states of trans-BAN were examined by calculating the indicator quantity $\Lambda$. This quantity was introduced by Peach et al.[95] as a measure of the charge-transfer character of an excited state (cf. Section 1.2.2). The values 0.67 and 0.47 for the $S_1$ and $S_2$ states, respectively, of the trans isomer obtained from PBE, correspond to transitions exhibiting predominantly local character.[95] These results indicate that the charge-transfer contribution is not dominant. Therefore, PBE should offer an acceptable description for the nonadiabatic

Table 4.1: Comparison of vertical transition energies for the lowest excited states of trans-BAN (in eV).

| **Method** | $\mathbf{S_1}$ | $\mathbf{S_2}$ |
|---|---|---|
| RI-PBE/TZVP | 3.26 | 3.83 |
| B3LYP/TZVP | 3.68 | 4.48 |
| exp | $4.00^a/4.07^b$ | - |

[a] Ref. [175], [b] Ref. [195]

dynamics simulation, in particular for the initially excited $S_1$ state.

## 4.4 Nonadiabatic Dynamics

The thermally broadened absorption spectrum at $T = 100$ K obtained from the initial conditions for the nonadiabatic dynamics simulation is presented in Figure 4.3. The initial ensemble, which is given as an inset in the figure, shows that only the trans isomer is populated and that the structure is relatively rigid.

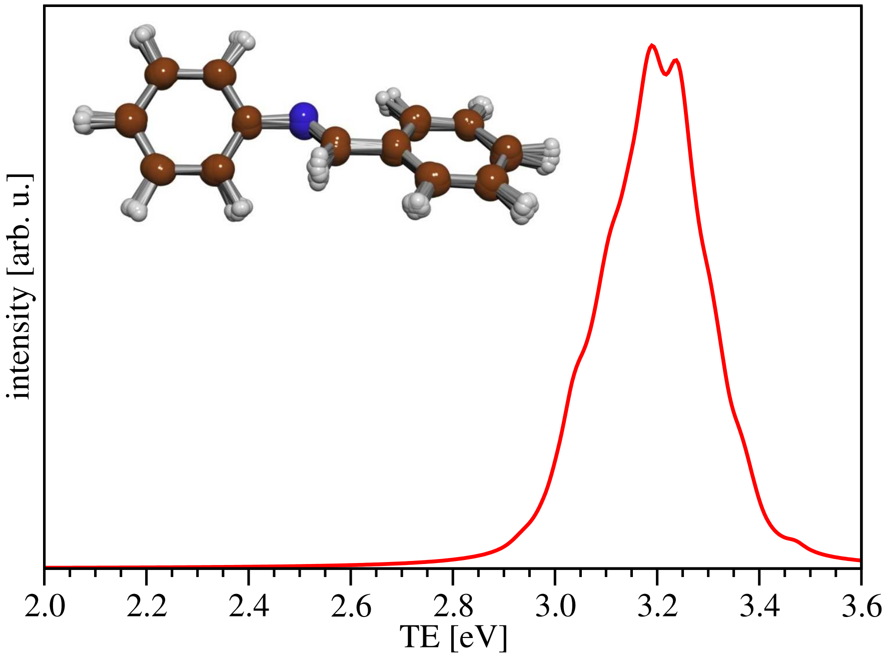

Figure 4.3: Theoretical thermally broadened stationary absorption spectrum for the $S_1$ state of trans-BAN at $T = 100\ K$. The discrete absorption lines for the ensemble presented in the inset were calculated with the PBE functional and subsequently convoluted with a Lorentzian function of 0.04 eV width.

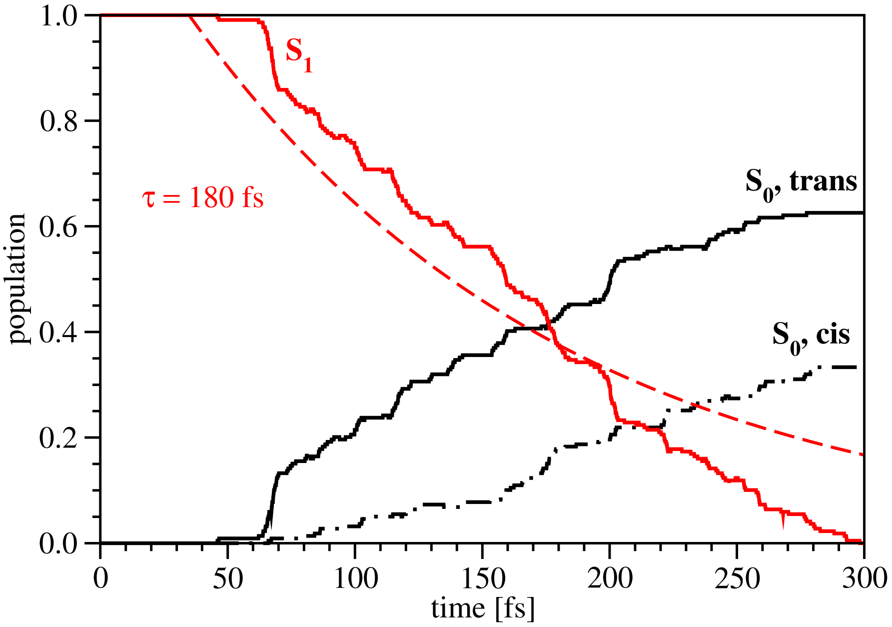

Figure 4.4: Time-dependent population of the $S_1$ state (solid red line) and the $S_0$ state of the cis (dash-dotted black line) and trans (solid black line) isomer for BAN, obtained from 220 nonadiabatic trajectories. The structures were classified as trans isomer if the final $C_{Ph}$-N=C-$C_{Ph}$ dihedral angle was in the range $[120°, 180°]$ and as cis if it was in the range $[0°, 60°]$. The lifetime $\tau$ of the $S_1$ state was determined by exponential fit (dashed red line) to be 180 fs.

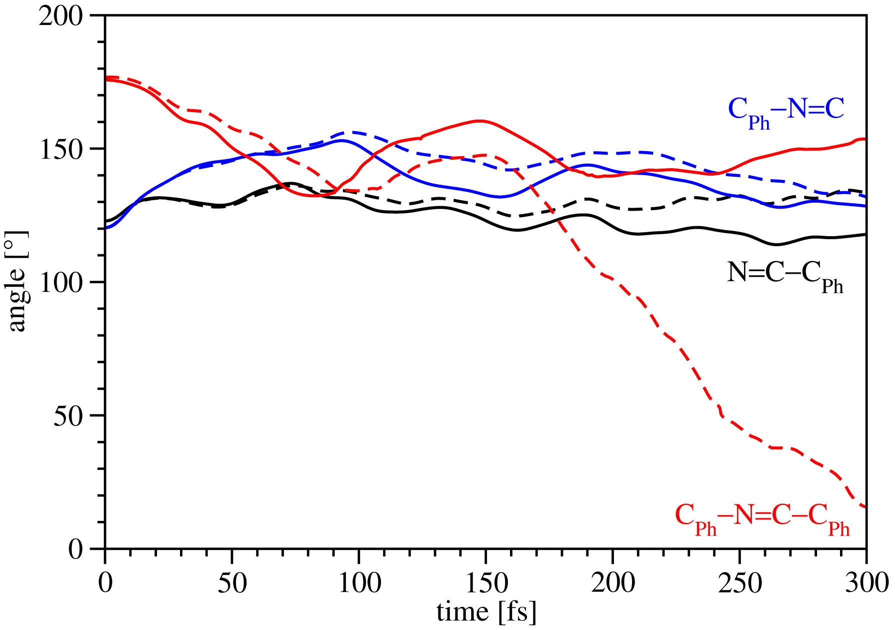

Figure 4.5: Time-dependent angles N=C-$C_{Ph}$ (black), C=N-$C_{Ph}$ (blue), and the dihedral angle $C_{Ph}$-N=C-$C_{Ph}$ (red) of the trans (solid lines) and cis (dashed lines) isomer of BAN, averaged over the ensemble of nonadiabatic trajectories. The structures are classified as cis if the final $C_{Ph}$-N=C-$C_{Ph}$ dihedral angle was in the range $[0°, 60°]$ and as trans if it was in the range $[120°, 180°]$.

For the analysis of the ultrafast photoisomerization process in BAN, the time-dependent state populations have been determined by monitoring the fraction of trajectories in each state as a function of time. As evident from the results presented in Figure 4.4, the initially excited $S_1$ state decays approximately exponentially with a resulting lifetime of 180 fs. Within 300 fs, the population is almost completely transferred into the ground state $S_0$, while the second excited state is not populated at all. For the investigation of the mechanism for the photoisomerization in BAN, the population of the ground state was decomposed into contributions of cis and trans isomers according to the value for the dihedral angle $C_{Ph}$-N=C-$C_{Ph}$ at the end of the simulation period. A trajectory was classified as trans for values in the interval $[120°, 180°]$ and as cis for values in the interval $[0°, 60°]$, since this dihedral angle is large for the trans isomer and small for the cis isomer of BAN (cf. Section 4.3). As can be seen in Figure 4.4, the photoswitching process is nonselective and only $\sim 33\,\%$ of the trajectories build up cis isomers, while the others exhibit no isomerization.

The analysis of the underlying processes in terms of the time-dependent angles N=C-$C_{Ph}$, C=N-$C_{Ph}$, and the dihedral angle $C_{Ph}$-N=C-$C_{Ph}$ is provided in Figure 4.5. As can be seen, the dihedral angles (red) of the whole ensemble remain in an interval of $[120°, 180°]$ for times $< 150$ fs. At this timescale, the population transfer from the $S_1$ state to the ground state ($S_0$) starts to occur (cf. Fig. 4.4). Subsequently, the trajectories

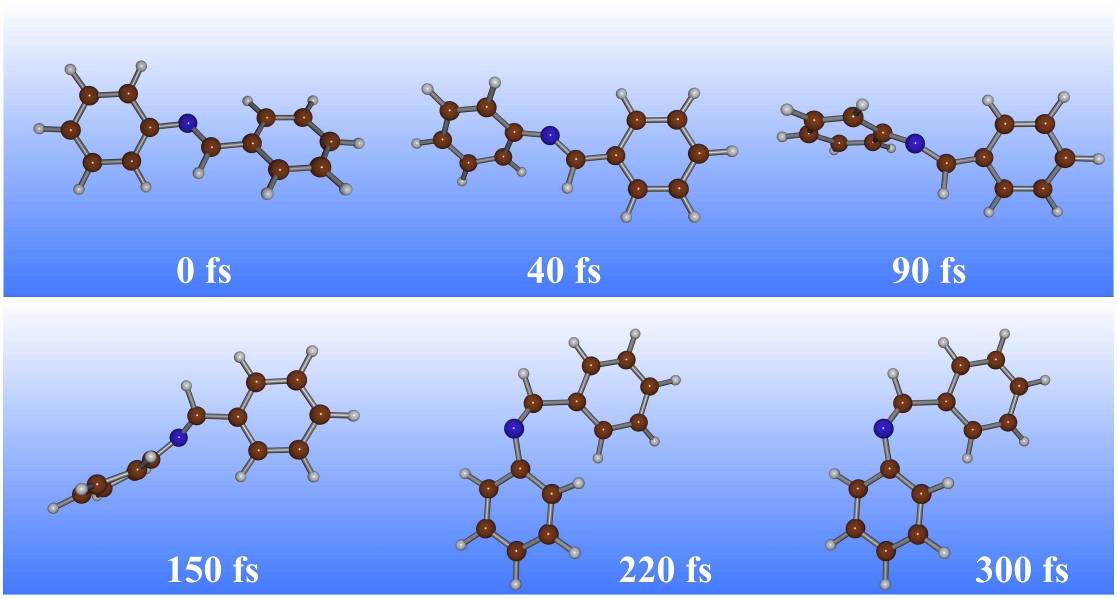

Figure 4.6: Snapshots of the nonadiabatic dynamics of BAN for one selected trajectory exhibiting isomerization to cis-BAN.

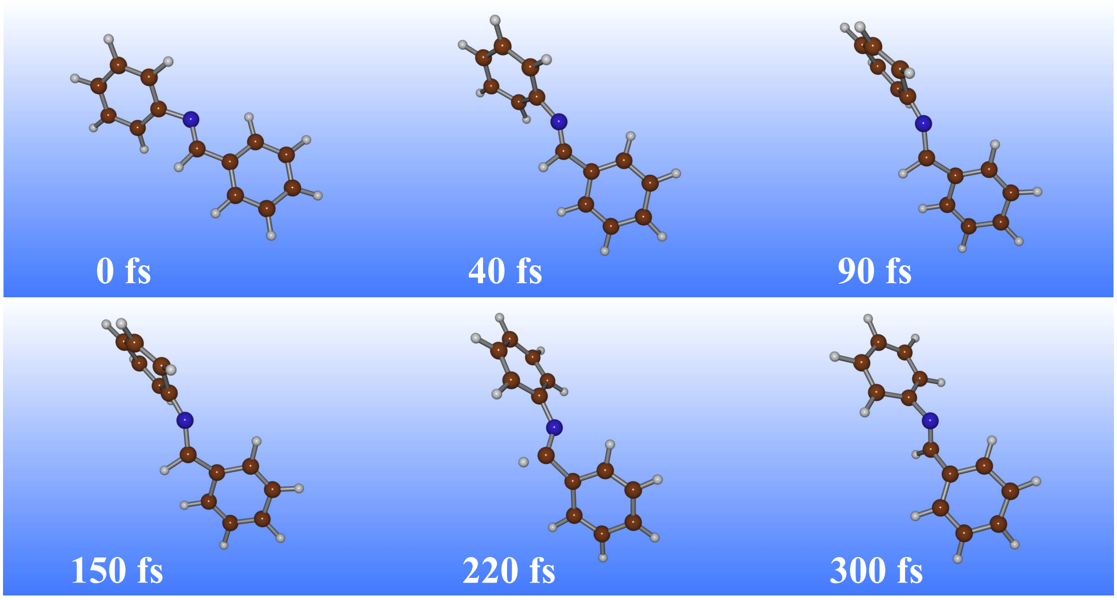

Figure 4.7: Snapshots of the nonadiabatic dynamics of BAN for one selected trajectory exhibiting no isomerization.

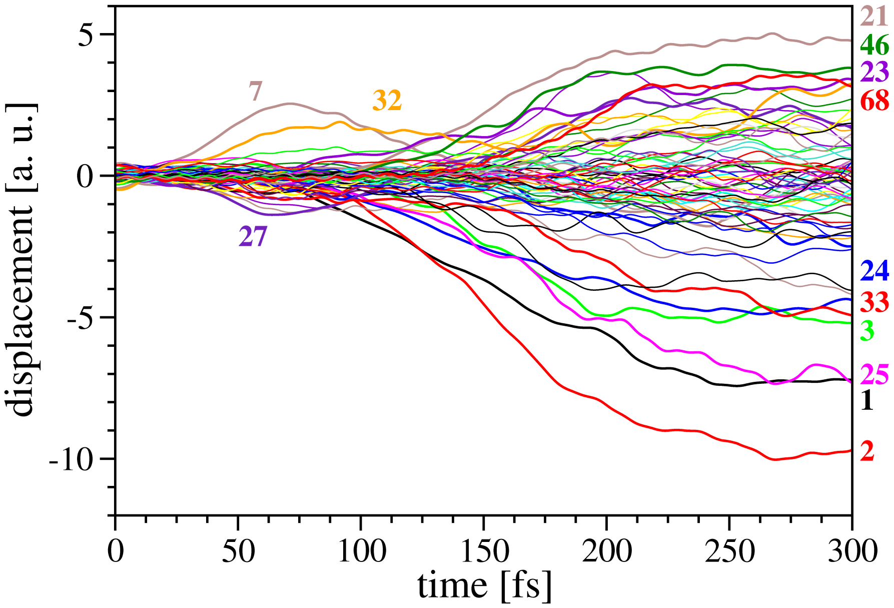

Figure 4.8: Time-dependent deviation of the normal coordinates from the trans-BAN equilibrium coordinates for one trajectory exhibiting isomerization to cis-BAN. The normal modes are indicated by numbers corresponding to increasing frequencies.

split into two channels, whereas the first channel corresponds to the formation of the cis isomer (dashed lines in Fig. 4.5). This process is reflected in the decreasing values of the $C_{Ph}$-N=C-$C_{Ph}$ angle for this fraction of the ensemble as time proceeds. The second channel is the back-isomerization into the trans isomer, for which the average angle of $\sim 160°$ at the end of the simulation is similar to the original value of $\sim 180°$ at $t = 0\,\mathrm{fs}$.

The mechanism of the photoisomerization is further analyzed on the example of two typical trajectories for both channels, which are presented in Figures 4.6 and 4.7. The snapshots of the dynamics of the trajectory exhibiting isomerization to the cis form (cf. Fig. 4.6) show that the molecule reaches a configuration with an almost linear C=N-C unit within the first 150 fs. An equivalent geometry can also be identified for the trajectory exhibiting no isomerization as illustrated in Figure 4.7. This configuration is closely related to the transition state that has been identified for the thermal isomerization in BAN.[198] Therefore, after nonadiabatic transition to the ground state, both the cis and the trans isomer can be built up, which provides an explanation for the low isomerization selectivity.

The complexity of the isomerization process is evident from Figure 4.8, in which a selected trajectory exhibiting trans-cis isomerization is projected onto the normal modes of the trans isomer. Within the first 70 fs, only a few normal modes are activated, while an increasing amount of normal modes are excited during the subsequent dynamics. The fact that a considerable number of degrees of freedom is involved in the nonadiabatic

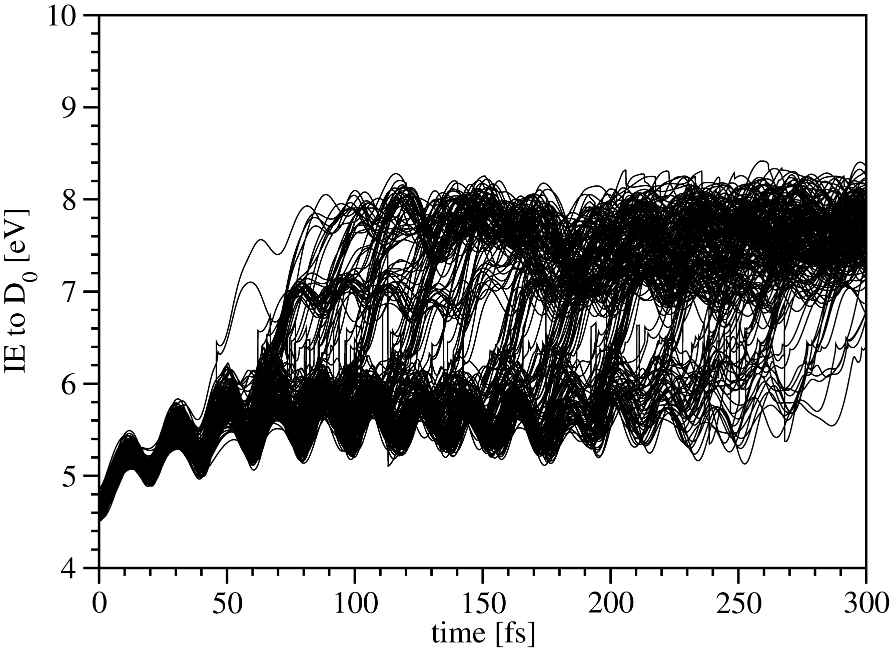

Figure 4.9: Time-dependent ionization energies (IE) to the cationic ground state $D_0$ calculated along 220 nonadiabatic trajectories.

dynamics clearly demonstrates that the photoisomerization process of benzylideneaniline cannot be accurately described based on reduced models which take into account only few degrees of freedom.

## 4.5 Time-Resolved Photoelectron Spectrum

The TRPES spectrum of BAN was simulated according to Eq. 4.1 by using the time-dependent ionization energies (IE) for an ensemble of 220 nonadiabatic trajectories. The latter were calculated from the energy difference of the neutral state, in which dynamics takes place, and the cationic ground state. As can be depicted from Figure 4.9, the time-dependent IEs rise from an average initial value of approximately 5 eV at $t = 0$ fs to IEs higher than 7 eV for times > 200 fs. This timescale corresponds to the population transfer from the initially excited $S_1$ state into the ground state (cf. Fig. 4.4).

The simulated TRPES spectrum presented in Figure 4.10(a) initially exhibits coherent oscillations of the ionization energy in the range between 4.7 and 6.0 eV with a period of approximately 20 fs, which can also be identified in Figure 4.9. The origin of these oscillations can be determined from the time evolution of the averaged internal coordinates corresponding to the C=N, C-$C_{Ph}$, and N-$C_{Ph}$ bond lengths shown in Figure 4.11. The figure illustrates the C=N bond (red) exhibiting a stretching motion with an oscillation period of $\sim 20$ fs, which is strongly activated due to the initial electronic excitation into the bound $S_1$ state involving the antibonding $\pi^*$ orbital (cf. Fig. 4.2). Thus, it can be

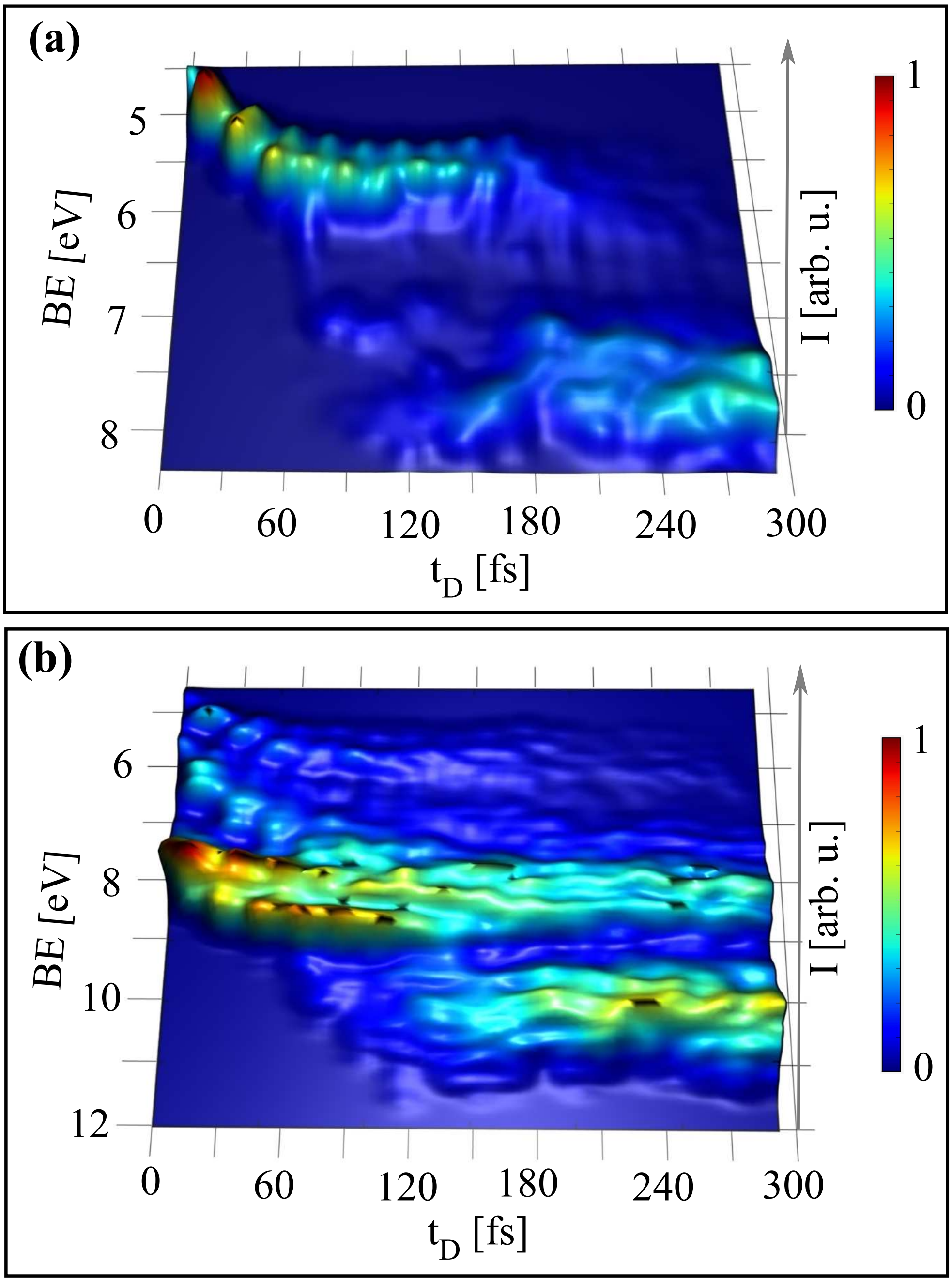

Figure 4.10: Simulated time-resolved photoelectron spectrum, illustrating the population transfer from the $S_1$ to the $S_0$ state in BAN as obtained from the nonadiabatic dynamics. (a) takes into account only the cationic ground state, (b) takes into account an additional eleven excited cationic states. The spectra (a) and (b) were independently normalized with respect to the highest peak.

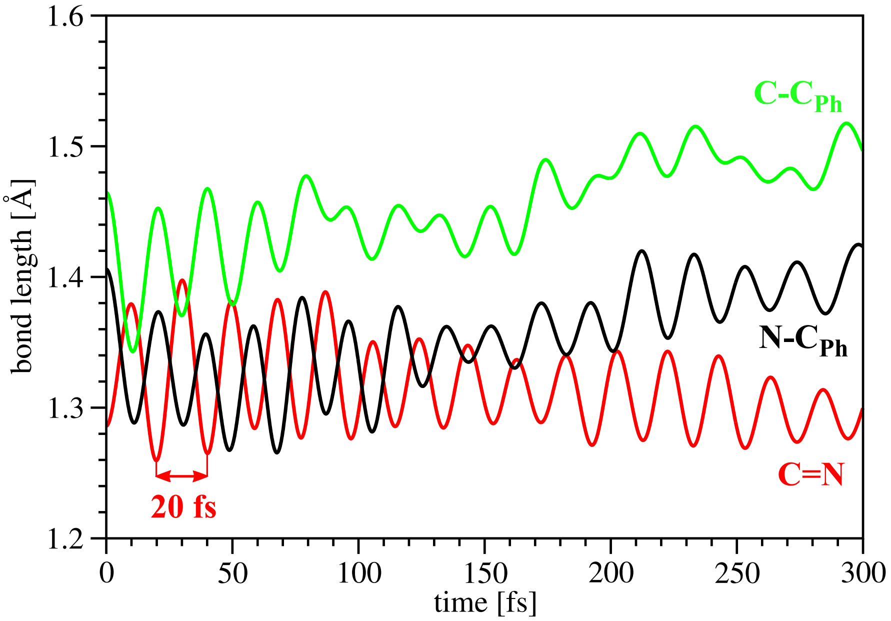

Figure 4.11: Time evolution of the C=N (red), C-C$_{Ph}$ (green) and N-C$_{Ph}$ (black) bond lengths of BAN, averaged over 220 nonadiabatic trajectories.

concluded that the stretching motion causes the coherent oscillations that have been identified in the TRPES spectrum (cf. Fig. 4.10).

The TRPES spectrum also exhibits a systematic shift of the ionization from initially 4.75 eV to a slightly higher energy of 5.75 eV after ∼ 100 fs. This shift is characteristic for the onset of the isomerization process and the reaching of the semi-linear transition state that was described in the previous section. Subsequently, the signal at 5.75 eV disappears and a new signal at the much higher ionization energy of ∼ 7.5 eV appears. This second shift reflects the population transfer from the excited S$_1$ state into the electronic ground state. Due to the high excess of energy that was gained during the nonadiabatic transition, this part of the spectrum does not exhibit any vibrational structure in contrast to the signal for shorter time delays.

Since in ionization processes higher cationic states can also be reached, their influence on the features of the time-resolved photoelectron spectrum was investigated by including eleven excited cationic states in the TRPES simulation. In the resulting spectrum presented in Figure 4.10(b), the contribution of higher states mainly smears out the oscillations corresponding to the C=N stretching motion in the bound S$_1$ state and leads to a broadening of the signal. However, the qualitative features of the spectrum, in particular the systematic shift of the ionization energy due to the nonadiabatic transition, remain preserved. Thus, the shift of the IE on the timescale of the S$_1$ → S$_0$ internal conversion should allow the experimental determination of the lifetime for the S$_1$ state in BAN.

## 4.6 Summary

The ultrafast photoswitching in benzylideneaniline has been studied for the first time in the frame of this thesis.[40] The calculated lifetime for the $S_1$ state of BAN ($\sim 180\,\mathrm{fs}$), as well as the features of the simulated TRPES, are similar to the time-resolved experimental results for azobenzene.[74] This molecule, which is a structurally and electronically related to BAN, has been intensively investigated in the past.[34,181,184–186,188] Due to the determination of the isomerization mechanism in BAN, a semi-linear configuration for the C-C=N-C subunit has been identified. This configuration is reached during the $S_1 \rightarrow S_0$ internal conversion and can lead to both isomerization to the cis form and back-isomerization to trans-BAN. These findings provide an explanation for the low selectivity of isomerization to cis-BAN, which is populated only by $\sim 33\,\%$. The presented results demonstrate that the TDDFT nonadiabatic is well suited for the simulation of time-resolved observables and for the prediction of nonradiative lifetimes in complex molecular systems. Furthermore, the method can serve to identify the mechanisms responsible for nonradiative processes. The simulated TRPES of BAN predicts, that the $S_1 \rightarrow S_0$ IC should be detectable experimentally. These theoretical findings motivated recent experimental investigations of the ultrafast photoisomerization in derivatives of BAN.[199]

# 5 Ultrafast Photodynamics in Furan

## 5.1 Introduction

Furan is one of the basic heteroatomic molecules. It serves as a structural unit in various biological substances. Therefore, the photophysical and photochemical properties of furan have attracted considerable attention in recent years.[200–211] In contrast to other heterocyclic aromatic molecules such as the isovalent thiophene,[212] the time-resolved photodynamics of furan has been investigated only recently in a joint cooperation between the theoretical group of Prof. V. Bonačić-Koutecký and the experimental group of Prof. Suzuki (Kyoto University, Kyoto, Japan) in the frame of this thesis.[85] In order to provide the interpretation of the experimental results, the time-resolved photoelectron spectrum of furan was simulated for the first time.

The broad absorption spectrum of furan in the deep UV region has been assigned to the four low-lying electronic transitions from the ground state to the $^1\mathrm{A}_2(\pi-3\mathrm{s})$, $^1\mathrm{B}_2(\pi-\pi^*)$, $^1\mathrm{A}_1(\pi-\pi^*)$, and $^1\mathrm{B}_1(\pi-3\mathrm{p_y})$ states.[213,214] While the $^1\mathrm{B}_2$ and $^1\mathrm{B}_1$ states exhibit rather large oscillator strengths, the forbidden transition to the $^1\mathrm{A}_2$ state is weakly allowed due to vibronic coupling with $^1\mathrm{B}_2$. In order to study the excited state dynamics of furan, Gromov et al. performed wave packet dynamics, using the multiconfigurational time-dependent Hartree (MCTDH) method with reduced dimensionality and applying the linear vibronic coupling approximation.[205–207] For this purpose, the parameters for the model were determined based on the EOM-CCSD method. Within this approach, the absorption spectrum was reproduced reasonably well. Ultrafast decay of the optically-excited $^1\mathrm{B}_2$ state into the $^1\mathrm{A}_2$ state was predicted to occur on a timescale of $\sim 25$ fs and the lifetime of the $^1\mathrm{A}_2$ was estimated to exhibit a lifetime longer than 200 fs. Since the ground state was not included in the model, internal conversion to the $\mathrm{S}_0$ state could

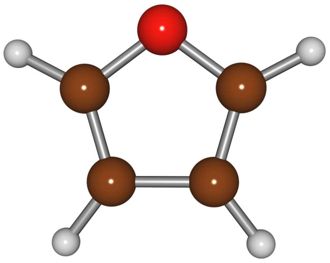

Figure 5.1: Equilibrium structure of furan optimized at the DFT level of theory (PBE0/6-311++G**). Carbon atoms are indicated by brown color, hydrogen atoms by white, and oxygen atoms by red.

not be described.

A possible deactivation of furan via a ring-opening mechanism was addressed by Wilsey et al.,[201] who used the complete active space self-consistent field (CAS-SCF) method. They identified the ring opened structure in both the singlet ($S_0$) and the triplet ($T_1$) state. Following this direction, Gavrilov et al. calculated excited states of furan by employing a combined density functional/multi-reference configuration interaction method (DFT/MRCI). They suggested a ring-opening deactivation pathway involving the $^1B_1(\pi - \sigma^*)$ state.[209] Along this pathway, they proposed rapid internal conversion from $^1B_2$ over $^1B_1$ to the ground state, but simulations of dynamics have not been carried out. Employing the EOM-CCSD method, Gromov et al. calculated potential energy surfaces recently, which were restricted to planar nuclear configurations, for future investigation of the ring-opening decay channel with nonadiabatic dynamics.[210]

In this work, nonadiabatic dynamics simulations taking into account all degrees of freedom were used to elucidate the photophysics and photochemistry of furan. For this purpose, the approach for the nonadiabatic dynamics in the frame of the TDDFT was employed (cf. Chapter 2). Moreover, the time-resolved photoelectron spectrum was simulated taking into account an approximate description of the photoionization probabilities based on TDDFT as developed in Chapter 3. The joint experimental and theoretical effort allowed for revealing ultrafast deactivation of excited furan through internal conversion from $S_2$ over $S_1$ to the ground state.[85,86]

The chapter is organized as follows: First, the computational aspects are outlined, followed by the theoretical and experimental absorption spectra of furan. Subsequently, theoretical simulations of ultrafast nonadiabatic dynamics in furan as well as the simulated time-resolved photoelectron spectrum are discussed and compared to experimental TRPES and time-resolved photoelectron imaging (TRPEI) results. Finally, the mechanism for the internal conversion as well as an interpretation of the experimental observables are proposed and discussed.

## 5.2 Computational and Experimental Methods

The photoinduced internal conversion in furan was examined by employing the TDDFT nonadiabatic dynamics simulations, which is outlined in detail in Chapter 2. The simulations were performed in a manifold consisting of the ground and the three lowest excited states. In the case that a crossing of the ground state and the first excited state occurred during the dynamics, the trajectory was forced to switch to the ground state. The 240 initial conditions were generated by sampling a molecular dynamics trajectory propagated in the neutral ground state with DFT at a constant temperature of $T = 300\,\mathrm{K}$. In order to examine if higher vibrational states are occupied at the simulation temperature, the populations of the vibrational states were calculated from their vibrational temperature. According to the results, even for the lowest vibrational mode with the vibrational temperature of 883 K, the $v = 1$ vibrational state is only populated to $5\,\%$. Since the occupation of $v = 1$ for the higher normal modes is even smaller, it can be assumed that at the simulation temperature only the $v = 0$ vibrational ground state is occupied for all modes. This corresponds to the experimental conditions in a supersonic molecular beam.

The energies, gradients, and nonadiabatic couplings for the molecular dynamics simulations were calculated with the hybrid PBE0 functional[215] combined with the 6-311++G** basis set[216] containing also diffuse functions. As will be demonstrated in Section 5.3, this level of theory describes accurately the stationary absorption properties of furan. Furthermore, the accuracy of TDDFT for the low-lying excited states of furan is evidenced in Section 5.4 by the comparison of the calculated sections of the potential energy surfaces along the main relaxation coordinate with the results obtained from the more accurate EOM-CCSD method.

For the simulation of the TRPES spectrum of furan, the experimental values were used for the pump and probe pulse energies ($E_{pu} = 6.2\,\text{eV}$ and $E_{pr} = 4.7\,\text{eV}$) as well as for the pulse widths ($\sigma_{pu} = 7.22\,\text{fs}$ and $\sigma_{pr} = 5.95\,\text{fs}$, corresponding to the experimental full width at half maximum (FWHM) values of 17 fs and 14 fs). The electronic transition dipole moments and the Franck-Condon factors for photoionization were assumed to be constant. Thus the analytic evaluation of the TRPES signal according to Eq. 3.9 in Chapter 3 has been performed by integration over all vibrational levels of the cation.

Since this work was performed in cooperation with the Prof. Suzuki's group, the experimental setup is also briefly described (for details see reference [85]). The experimental TRPEI was performed with sub-20 fs pulses at 4.7 eV (260 nm, FWHM = 14 fs) and 6.2 eV (200 nm, FWHM = 17 fs) generated by the multi-color filamentation method.[217,218] The photoelectron imaging apparatus consisted of a source, a buffer, and an ionization chamber. As in standard TRPEI experiments, the linear polarization directions of the pump and probe laser beams were aligned parallel to each other, and these were also set parallel to the face of the MCP detector. The three-dimensional photoelectron speed and angular distributions were reconstructed from the projection images using the pBaseX method.[219] The cross-correlation of the pump and probe pulses was determined in situ to be 22 fs by nonresonant $(1 + 1)$ multiphoton ionization of a supersonic beam of ethanol seeded in Argon. The time origin of the pump-probe delay was determined with an accuracy of a few femtoseconds. The delay time $t_D$ between the pump and probe pulses was controlled with a closed-loop translation stage with 5 nm accuracy.

## 5.3 Electronic Properties

The temperature broadened TDDFT absorption spectrum of furan at room temperature simulated for an ensemble of 240 initial conditions is presented in Figure 5.2, together with the experimental photoabsorption spectrum. The good agreement between experiment and theory allows for the straightforward assignment of electronic transitions.

The lowest excited state ($S_1$) is the $\pi - 3s$ Rydberg state with $A_2$ symmetry, which gives rise to the weak feature in the low energy part of the experimental spectrum (5.6 - 6.0 eV) in agreement with the assignment in previous experimental and theoretical works.[200,204,205,209,213,214] The comparison of the transition energy of 5.87 eV calculated with TDDFT at the equilibrium geometry (cf. Fig. 5.1) with experimental measurements

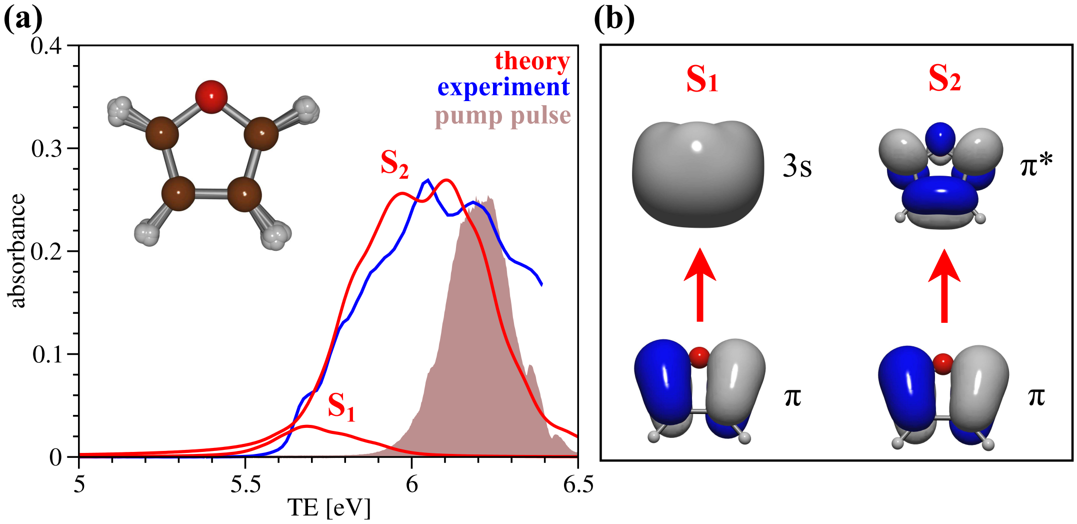

Figure 5.2: (a) Comparison of the theoretical thermally broadened absorption spectrum of furan (solid red lines) for the first $S_1(\pi - 3s)$ and second $S_2(\pi - \pi^*)$ excited state with the measured absorption spectrum at room temperature (solid blue line). The discrete absorption lines for the ensemble presented in the inset were calculated with the PBE0 functional and subsequently convoluted with a Lorentzian function of 0.04 eV width. The spectrum of the experimental pump pulse is shown as a filled curve. (b) Character of the $S_1(\pi - 3s)$ and $S_2(\pi - \pi^*)$ transitions.

Table 5.1: Comparison of vertical transition energies for the $S_1$ and $S_2$ states of furan (in eV).

| **Method** | $\mathbf{S_1}$ $(\pi - 3s)$ | $\mathbf{S_2}$ $(\pi - \pi)$ |
|---|---|---|
| PBE0/6-311++G** | 5.87 | 6.20 |
| EOM-CCSD/aug-cc-pVTZ+diffuse(O) | 6.16 | 6.49 |
| DFT/MRCI[a] | 5.81 | 6.00 |
| CASPT2[b] | 5.92 | 6.04 |
| experiment[c] | 5.91 | 6.04 |

[a] Ref. [209], [b] Ref. [200], [c] Ref. [213, 214]

as well as previous theoretical results presented in Table 5.1 yields a good agreement. However, the transition energy obtained with EOM-CCSD is 0.3 eV higher in energy. For these calculations, the aug-cc-pVTZ basis set with an additional diffuse basis function centered at the oxygen atom was employed, as suggested by Serrano et al.[200] The optically allowed transition from the highest molecular orbital with $\pi$ character into the lowest unoccupied orbital with $\pi^*$ character produces the bright second excited state $S_2$ (cf. Fig. 5.2(b)) with $B_2$ symmetry. This state produces the strong absorption feature at $\sim$ 6 eV in the experimental spectrum. The vertical transition energy calculated at the equilibrium geometry of $TE = 6.20$ eV agrees reasonably well with available experimental and theoretical results (cf. Table 5.1). As in the case of the $S_1$ state, the transition energy of the $S_2$ state calculated with the EOM-CCSD methods is $\sim$ 0.3 eV higher in energy. However, according to Gromov et al., the EOM-CCSD energies of the $S_1$ and $S_2$ states are expected to be too high in energy with respect to the experiment,[206] thus providing an explanation for the deviation from the PBE0 results. The third excited $^1B_1$ $(\pi - 3p_y)$ Rydberg state with a transition energy of 6.34 eV is responsible for a second strong absorption band in the experimental spectrum above 6.45 eV (not shown in Fig. 5.2).[85]

The excellent agreement of the theoretical and the experimental spectrum in Figure 5.2(a) provides confidence for the use of PBE0/6-311++G** in the nonadiabatic dynamics simulations.

## 5.4 Nonadiabatic Dynamics

The experimental pump pulse centered at 6.2 eV is expected to induce population transfer mainly into the $S_2$ state, since both the oscillator strength of the $S_1$ state and the overlap with the experimental pump pulse are small (cf. Fig. 5.2(a)). In contrast, the $S_2$ state overlaps well with the pump pulse spectrum and exhibits a high oscillator strength. The second strong absorption band due to the $\pi - 3p_y$ Rydberg state is well separated from the pump pulse spectrum. Thus it can be assumed that no excitation to the Rydberg state takes place in the experiment. Therefore, the nonadiabatic dynamics simulations were performed for an ensemble initially excited to the $S_2$ state.

The ultrafast nonadiabatic processes can be analyzed in terms of the time-dependent electronic state populations presented in Figure 5.3. The nonadiabatic transition from

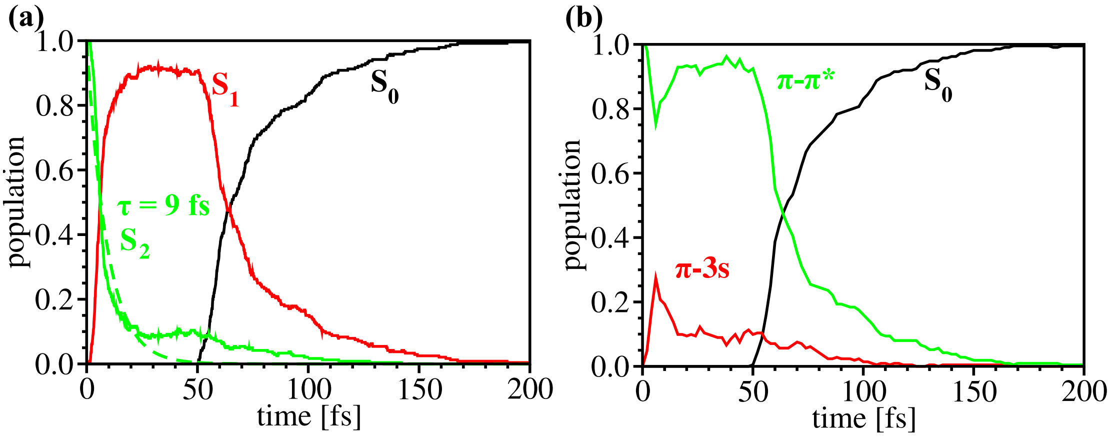

Figure 5.3: Time-dependent (a) calculated adiabatic ($S_0$, $S_1$, and $S_2$) and (b) approximate diabatic ($S_0$, $\pi-\pi^*$, and $\pi-3s$) populations of the ground state and the two lowest excited states of furan after excitation into the $S_2$ state. The lifetime $\tau$ of the $S_2$ state was determined by exponential fit (green dashed line) to be 9 fs.

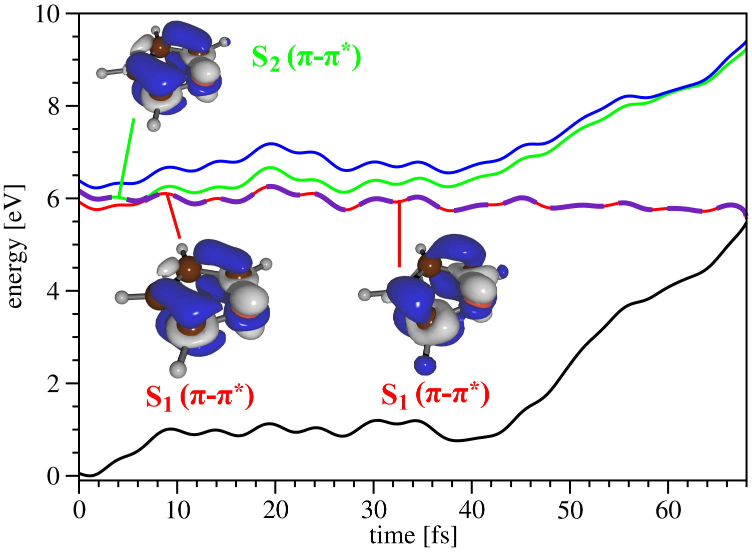

Figure 5.4: Energies of the ground state (black) and the three lowest excited states (red $S_1$, green $S_2$, blue $S_3$) as a function of time obtained from nonadiabatic dynamics along one selected trajectory. The dashed violet line indicates the energy of the currently populated state during the dynamics. The character of the electronic state is indicated by the electron density differences between ground and given excited state shown in the insets.

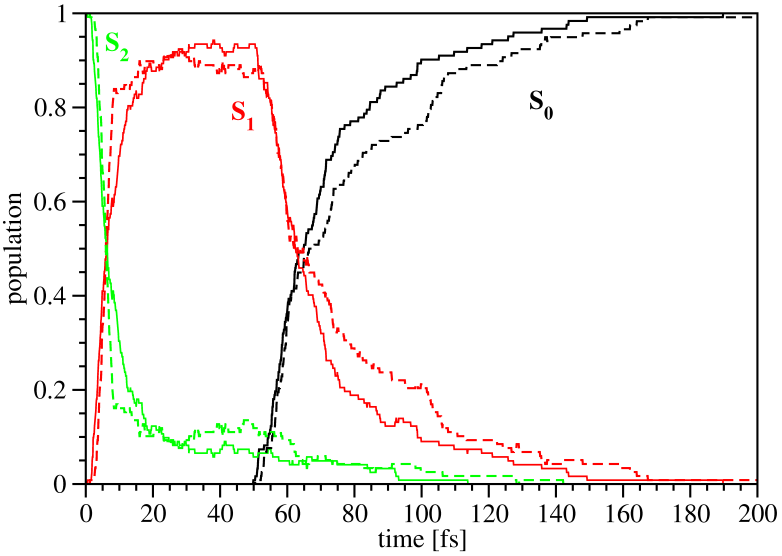

Figure 5.5: Time-dependent adiabatic populations for the ground state and the two lowest excited states of furan for two different initial distributions: transition energy for the initial excitation into the S$_2$ state $< 6.01$ eV (solid lines) and $> 6.01$ eV (dashed lines).

the adiabatic S$_2$ state to the adiabatic S$_1$ state takes place at very short times yielding an S$_2$ state decay time constant of 9 fs. Subsequently, dynamics takes place in the first excited state exhibiting a lifetime of $\sim 50$ fs. This is followed by the return to the ground state, which is completed after $\sim 140$ fs (cf. Fig. 5.3(a)). The adiabatic electronic state populations, which were directly obtained from the surface hopping procedure, can be decomposed in terms of the approximate diabatic characters of the involved state. These characters can be estimated by analyzing the KS orbitals mainly involved in the currently populated adiabatic state. In the resulting approximate diabatic picture presented in Figure 5.3(b), the character of the initially excited $\pi - \pi^*$ remains mainly preserved during the adiabatic S$_2 \rightarrow$ S$_1$ transition, while the diabatic $\pi - 3s$ state is only weakly populated during the dynamics simulation. The time evolution of the character of the excited states together with their time-dependent energies for one selected trajectory are visualized in Figure 5.4. As can be seen, the populated diabatic state during the dynamics maintains the $\pi - \pi^*$ diabatic character until transition to the ground state takes place, while a switch from the adiabatic S$_2$ state to S$_1$ occurs at $t \sim 7$ fs.

In order to investigate the influence of the pump pulse energy on the nonadiabatic dynamics, simulations for two different ensembles representing different parts of the Franck-Condon region ($TE < 6.01$ eV and $TE > 6.01$ eV) were performed. As shown in Figure 5.5, the time-dependent populations show no significant dependence on the energy distribution of the initial ensemble. This indicates that the photodynamics of furan should not be sensitive to small changes of the pump pulse energy.

The analysis of the molecular motion involved in the nonadiabatic relaxation in terms

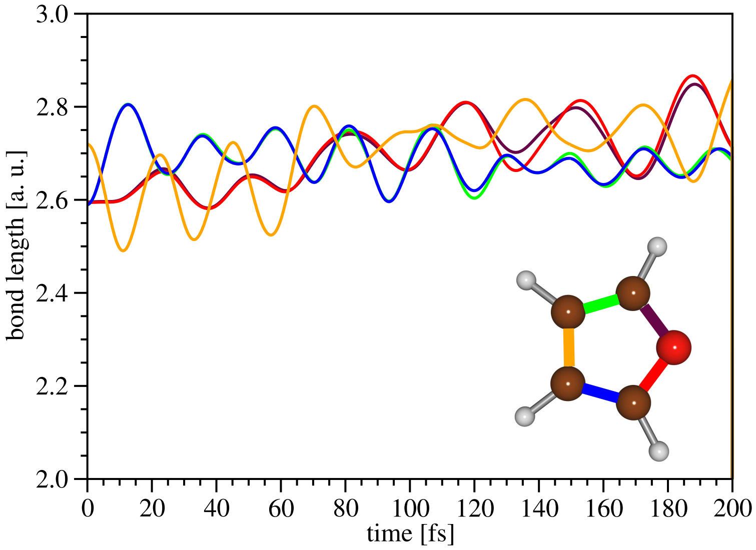

Figure 5.6: Time-dependent C-C and C-O bond lengths of furan averaged over 240 trajectories obtained from nonadiabatic dynamics. The bond types are indicated by their colors as given in the inset.

of five bond lengths of furan is presented in Figure 5.6. As can be observed from the time evolution of both C-O distances (red and maroon), the C-O stretching motions are excited after 100 fs. Since in previous theoretical investigations the relaxation along the ring-opening coordinate involving the $\pi - \sigma^*$ excited state had been suggested as a possible deactivation pathway,[209,210] the energies of the lowest excited states were calculated as a function of the C-O bond elongation. The comparison of the TDDFT and EOM-CCSD results shown in Figure 5.7 yields a good agreement, therefore providing confidence for the description of the PESs with the TDDFT method. As can be seen, the excited state dynamics takes place in a region of the potential energy surfaces in which both the $S_1$ and $S_2$ states are either of $\pi - 3s$ Rydberg or $\pi - \pi^*$ character. Thus, the $\pi - \sigma^*$ is not involved in the nonadiabatic dynamics of furan. For larger C-O bond elongations than those reached in the dynamics simulation, the lowest excited state adopts $\pi - \sigma^*$ character, as depicted in Figure 5.7.

Figure 5.8 shows a schematic representation of the processes during the photodynamics, which was extracted from the results of the nonadiabatic dynamics simulations. The geometric relaxation of furan in the excited states $S_1$ and $S_2$, which is shown in the upper part of the scheme and is indicated by red arrows, occurs within the C-O-C subunit. In contrast to the suggested ring-opening pathway involving only planar configurations of furan,[209,210] the $S_2 \rightarrow S_1 \rightarrow S_0$ nonadiabatic dynamics involves an out of plane distortion in combination with an elongation of the C-O bonds. After the return to the ground state, three channels can be identified. The main channel, which is indicated by a thick arrow in Figure 5.8, leads to formation of hot furan (I). The other two possible minor

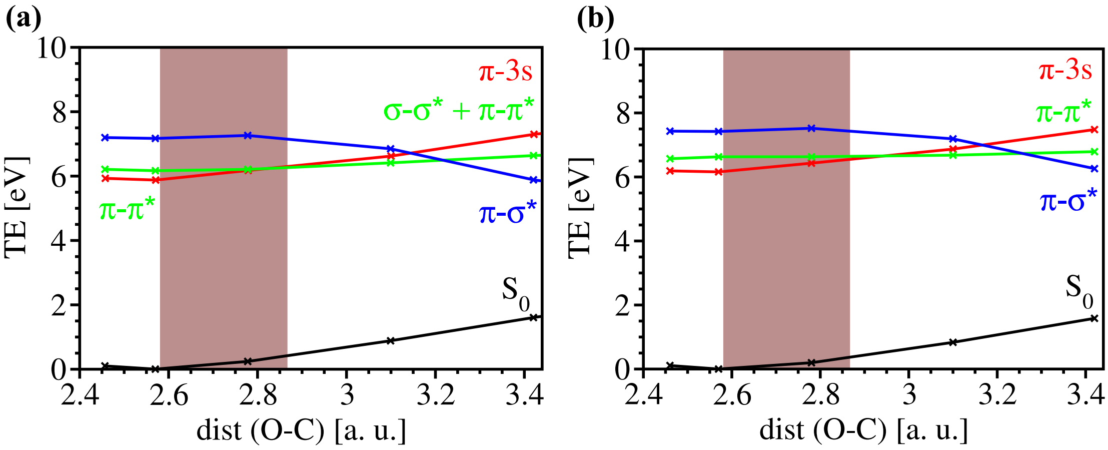

Figure 5.7: Comparison of (a) TDDFT and (b) EOM-CCSD energies of the ground state and three excited electronic states of furan as a function of the elongation of one C-O bond. The red region indicates the range of C-O bond lengths reached during the nonadiabatic dynamics simulations.

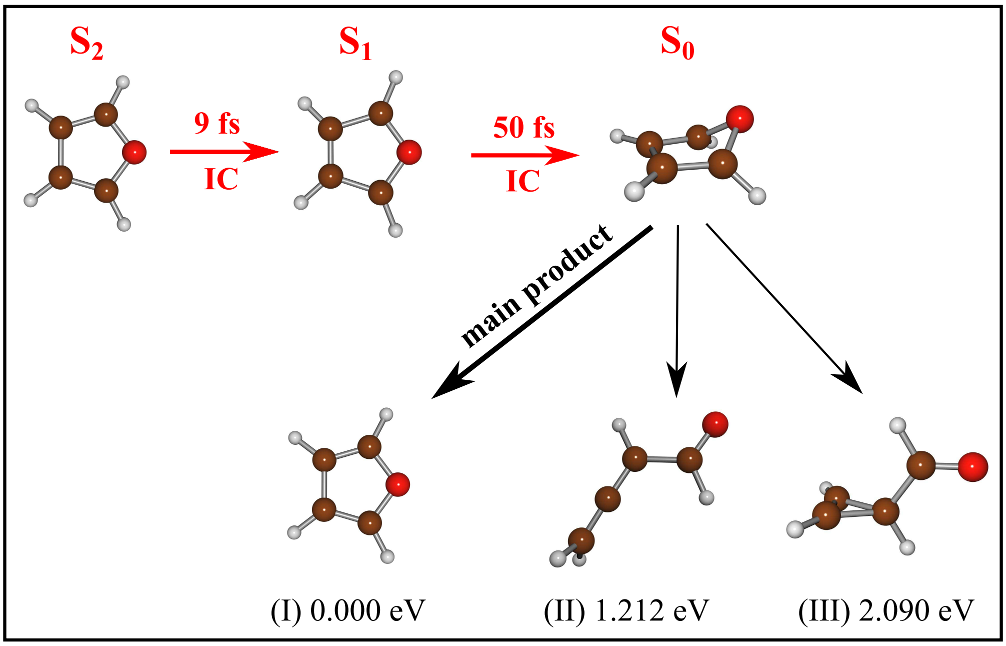

Figure 5.8: Schematic representation of the photodynamics of furan obtained from nonadiabatic dynamics. The $S_2 \rightarrow S_1$ and $S_1 \rightarrow S_0$ internal conversions and the corresponding timescales are shown in red, while the products in the ground state are indicated by black arrows (main product thick arrow, other two products thin arrows). The relative energies in eV for the minimized structures of the products are also given.

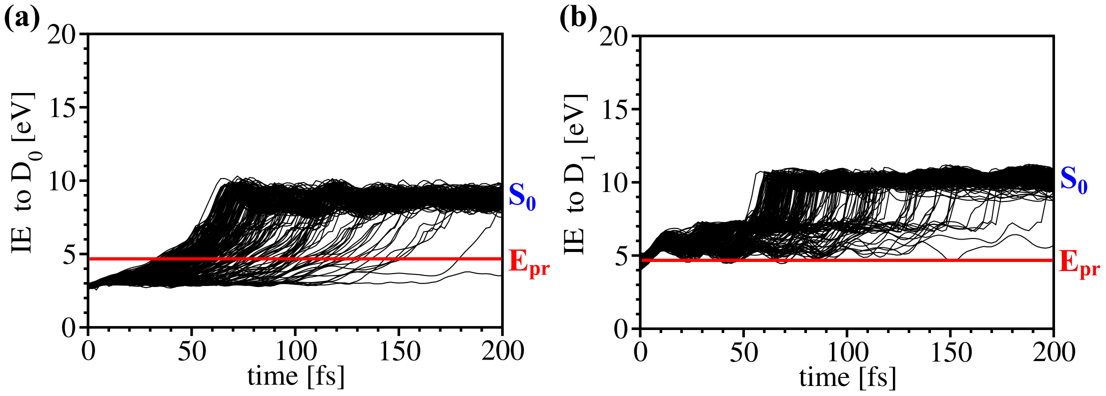

Figure 5.9: Time-dependent ionization energy (IE) calculated along 240 nonadiabatic trajectories for (a) the cationic ground state $D_0$ and (b) the cationic first excited state $D_1$. The red line at 4.7 eV indicates the experimental probe pulse energy $E_{pr}$.

channels, which involve breaking the C-O bond, lead to formation of 2,3-butadienal (II) or cyclopropen-3-carbaldehyde (III). However, they are reached only with very low probability after the transition to the ground state. Thus, according to the MD simulations, bond breaking occurs exclusively in the ground state.

## 5.5 Time-Resolved Photoelectron Spectrum

The calculated ionization energies from the neutral ground state to the cationic ground state ($D_0$) and first excited state ($D_1$) of furan at the equilibrium geometry, $IE(\mathrm{D}_0) = 8.91\,\mathrm{eV}$ and $IE(\mathrm{D}_1) = 10.61\,\mathrm{eV}$, are in good agreement with available experimental values of 8.9 eV[208,220] and 10.3 eV.[220,221] Both of these states can be reached by the ionization from the equilibrium geometry in the experiment, since the sum of the pump (6.2 eV) and probe (4.7 eV) photon energy of 10.9 eV is sufficiently high.

The photoionization process can be investigated by analyzing the time evolution of the ionization energies along the nonadiabatic trajectories. The results presented in Figure 5.9 show that only for very short times ($t < 10$ fs) both cationic states are accessible by the experimental probe pulse. Afterwards ($t > 10$ fs), the only energetically possible transition occurs to the $D_0$ state. This corresponds to the timescale of the decay for the adiabatic $S_2$ state with a calculated time constant of 9 fs (cf. Fig. 5.3). After that, when the ensemble has returned to the ground state $S_0$, no photoionization can occur since the cationic states are energetically not accessible.

In both the simulated and experimental TRPES spectra presented in Figure 5.10(a) and (b), the ultrafast deactivation of furan is reflected in the decreasing signal intensities for time delays between 10 and 100 fs. This decrease indicates the population transfer into the electronic ground state $S_0$, from which ionization is energetically not possible.

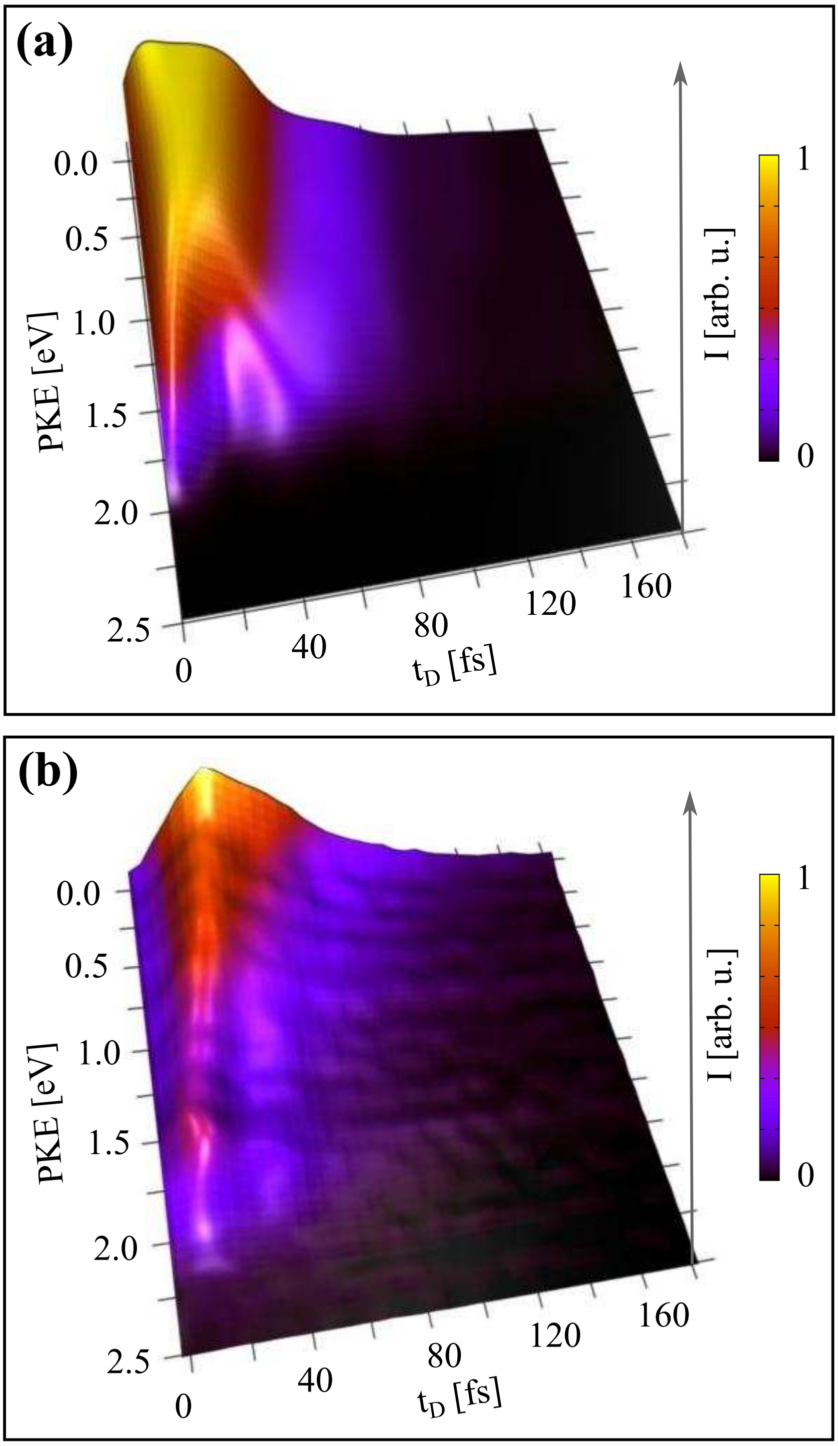

Figure 5.10: (a) Simulated and (b) experimental TRPES spectra of furan. The spectra (a) and (b) were independently normalized with respect to the highest peak.

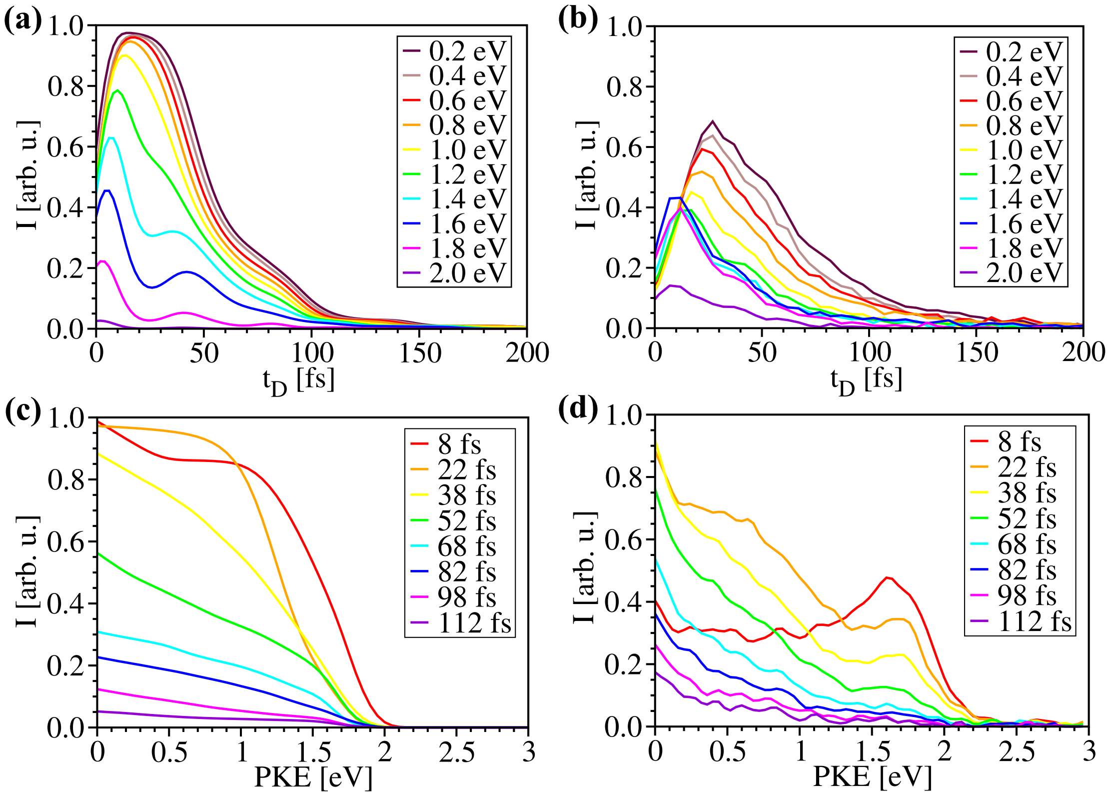

Figure 5.11: Time evolution of (a) theoretically and (b) experimentally obtained photoelectron intensities at selected photoelectron kinetic energies (PKE). (c) Simulated and (d) experimental photoelectron spectra for selected pump-probe time delays $t_D$. The signals (a)-(d) were independently normalized with respect to the highest peak in the TRPES spectra.

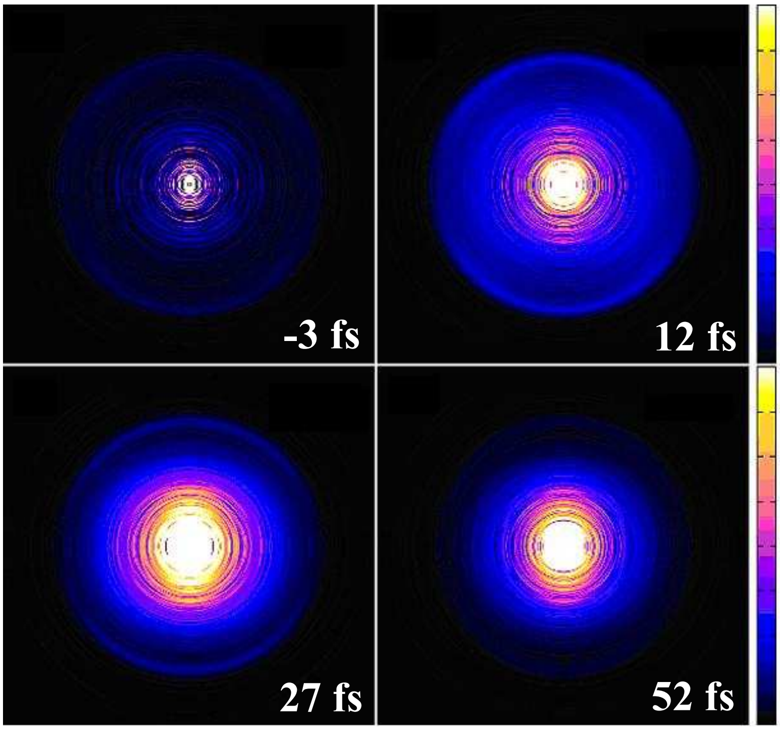

Figure 5.12: False-color maps of experimental photoelectron images observed at different pump-probe time delays. The images correspond to the two-dimensional slices of three-dimensional distributions calculated by the pBaseX method. The color bar for the intensity of the signals is also given.

For a more detailed analysis, the photoelectron intensities at selected PKEs have been calculated and are presented in Figure 5.11(a) together with the experimental signals in Figure 5.11(b). As can be seen, the average intensities of the theoretical as well as the experimental signals increase with decreasing PKEs. All of the signals exhibit maxima at short time delays ($t_D < 40\,\mathrm{fs}$). The maxima are shifting to longer time delays with decreasing PKE values. The slices from the TRPES for selected time delays shown in Figure 5.11(c) also reproduce well the features of the experimental slices presented in Figure 5.11(d), except at very short time delays. For time delays with overlapping pump and probe pulses (8 fs in Fig. 5.11(c) and (d)), the simulation provides only qualitative TRPES results, since the $S_2$ state is excited instantaneously without taking into account the overlap between pump and probe pulses.

Figure 5.12 shows representative snapshots of the experimental photoelectron images. In these images, a sharp single ring can be identified in the outer part of the images corresponding to high PKE values, whose intensity is diminishing within 50 fs. Careful inspection of the image observed at 12 fs confirms that more electrons are ejected in the parallel than in the perpendicular direction with respect to the laser polarization, thus yielding an anisotropic PAD. The analysis of the $\beta$ parameters for this ring yields

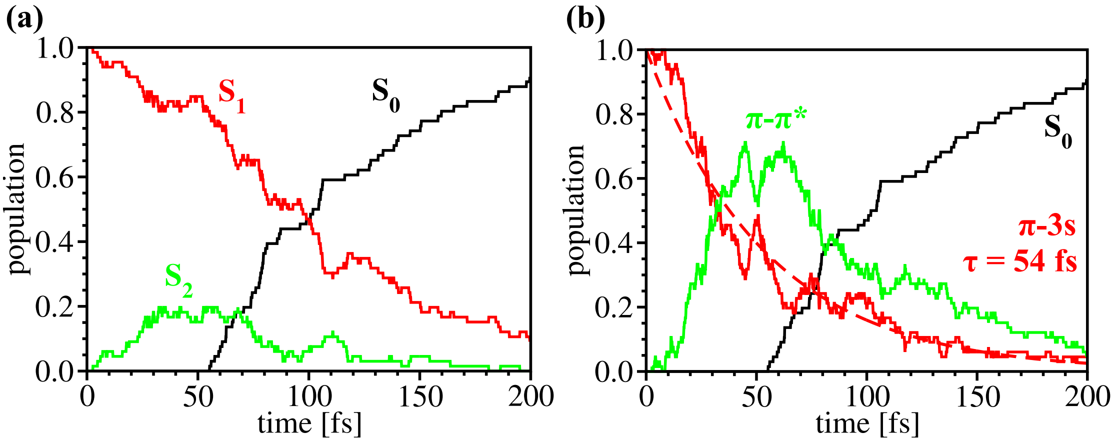

Figure 5.13: Time-dependent (a) calculated adiabatic ($S_0$, $S_1$, and $S_2$) and (b) approximate diabatic ($S_0$, $\pi-\pi^*$, and $\pi-3s$) populations of the ground and two excited states of furan initially excited to the $S_1$ state. The lifetime $\tau$ of the diabatic $\pi-3s$ state was determined by exponential fit (red dashed line) to be 54 fs.

an angular distribution with high positive $\beta_2$ values (cf. Figure 4(b) in Ref. [85]), which is typical for photoionization from a 3s Rydberg state.[222] These results indicate that in the experiment the $S_1$ ($\pi-3s$) Rydberg state was simultaneously excited with the $S_2$ ($\pi-\pi^*$) state, which is a possible explanation for the additional experimental signal at high PKE values for short time delays (cf. Fig. 5.11(b)). However, this is a minor component compared to the experimental TRPES signal for lower PKEs, which corresponds to the $S_2$ state (cf. Fig. 5.10(b) and 5.11(b)).

In order to investigate the $S_1$ component of the experimental TRPES signal, nonadiabatic dynamic simulations for an ensemble initially excited to the $S_1$ ($\pi-3s$) state was carried out. As shown in Figure 5.13, this state decays within 200 fs. During the decay process the character of the $S_1$ state changes from $\pi-3s$ Rydberg to $\pi-\pi^*$ on the timescale of 54 fs. The experimental value for the $\pi-3s$ lifetime, which was determined as 29 fs from exponential fit of the corresponding PKE slice of the TRPES signal, (cf. Fig. 2 in Ref. [85]) is shorter. Notice that after change from diabatic $\pi-3s$ to $\pi-\pi^*$ character, this part of the experimental signal is expected to strongly interfere with the signal from the originally populated $S_2$ state also exhibiting $\pi-\pi^*$ character.

Ultrafast $S_2 \rightarrow S_1 \rightarrow S_0$ internal conversion of furan within 140 fs is also reflected in the time-resolved total photoelectron and total photoion signals given in Figure 5.14. The good agreement of the experimental photoion and photoelectron signals shown in Figure 5.14(b), which have been independently measured, indicates that dissociative ionization is negligible. The calculated total photoelectron signal obtained from integration of TRPES over the whole PKE range, as shown in Figure 5.14(a), agrees well with the experimental results, thus providing evidence of the accuracy of the simulations. As in the case of the TRPES spectra (cf. Fig. 5.10), both the theoretical and experimental

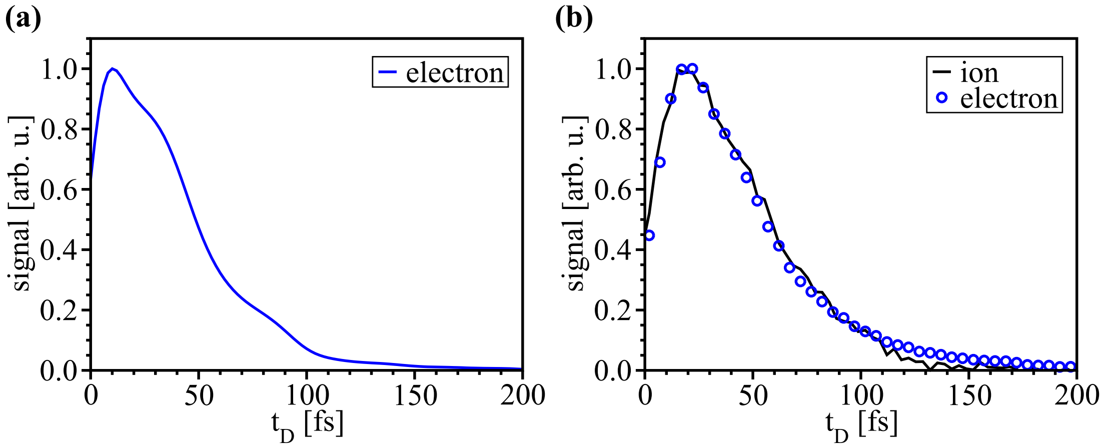

Figure 5.14: (a) Total photoelectron signal obtained from integration of the simulated TRPES spectrum over the whole PKE range. (b) Total photoelectron (solid circles) and photoion (full line) signal obtained from (1 + 1') REMPI.[85] The signals (a) and (b) were independently normalized with respect to the highest peak.

signals exhibit a maximum at short time delays corresponding to the timescale of the $S_2 \rightarrow S_1$ internal conversion. Subsequently, the signals decrease constantly and approach zero intensity after $\sim 140\,\mathrm{fs}$, indicating completion of the return to the ground state.

## 5.6 Summary

The ab initio nonadiabatic dynamics and the simulation of time-resolved photoelectron spectra in the frame of TDDFT combined with the experimental time-resolved photoelectron imaging spectroscopy have for the first time revealed the ultrafast deactivation process from the $S_2$ to the $S_0$ state in furan.[85] It has been shown that the $S_2 \rightarrow S_1$ internal conversion takes place on a very short timescale yielding a lifetime of 9 fs for the $S_2$ state followed by the return to the ground state within $\sim 140\,\mathrm{fs}$. According to the simulations, the $\pi - \pi^*$ diabatic character remains mainly preserved during the deactivation process, in contrast to previously suggested mechanisms involving the $\pi - \sigma^*$ state. These findings agree with the experimental TRPEI results, which do not indicate a change in the character of the excited state after initial $\pi - \pi^*$ excitation. The excellent agreement of simulated and experimental signals proves the accuracy of the theoretical approach for the simulation of nonadiabatic dynamics and TRPES spectra.[85,86] Therefore, the presented theoretical approach provides a valuable tool for the investigation of ultrafast photochemical reactions and assignment of experimental features to the underlying processes.

# 6 Internal Conversion in Pyrazine

## 6.1 Introduction

Pyrazine represents a prototype for heterocyclic biochromophores, which can serve as a model system for the examination of ultrafast photoinduced processes in biologically important chromophores. Pyrazine can be employed as a benchmark system for the test of new methods, since it has been intensively investigated both theoretically and experimentally to study the ultrafast internal conversion (IC) through conical intersection.[39,81,142,144,146,223–234]

The electronic absorption spectrum covering transitions from the ground state $S_0$ to both the $S_1$ $(n - \pi^*)$ and $S_2$ $(\pi - \pi^*)$ excited states has been accurately measured.[235,236] Excitation to the $S_2$ state yields a broad band with little structure, indicating fast relaxation due to the $S_2 \rightarrow S_1$ IC. In order to reproduce the broad $S_2$ absorption spectrum, a model consisting of 4 vibrational modes[227] was found to mimic the essential dynamics of the system. However, convolution with a broad Lorentzian was necessary for yielding an agreement with the experimental spectrum. By including the neglected 20 vibrational modes as a harmonic oscillator heat bath,[228,229] a qualitatively correct description of the ultrafast relaxation was gained. The experimental absorption spectrum, however, could not be fully reproduced. Simulations with an increased number of explicitly treated modes (e.g. 12 by Puzari et al.[234]) still required additional broadening in order to reproduce the experimental spectrum. These findings indicate that for the accurate description of the $S_2 \rightarrow S_1$ IC in pyrazine, all degrees of freedom have to be included. In this work, the simulations of the nonadiabatic dynamics of pyrazine taking into account all degrees of freedom was achieved by employing the TDDFT nonadiabatic dynamics presented in Chapter 2.[39]

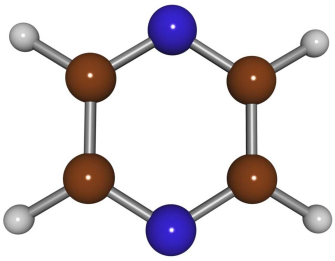

Figure 6.1: Equilibrium structure of pyrazine optimized with DFT (B3LYP/TZVP). Carbon atoms are indicated by brown color, hydrogen atoms by white, and nitrogen atoms by blue.

In earlier theoretical simulations of the TRPES spectrum of pyrazine, in which a limited number of degrees of freedom were taken into account and transition dipole moments for ionization were assumed to be constant, a systematic shift of the signal maximum to lower photoelectron kinetic energy (PKE) was predicted to occur due to the IC. [142] However, experimental measurements [81,232] as well as quantum dynamical simulations, in which a limited number of vibrations were considered explicitly and transition dipole moments for ionization to the ground and first excited cationic states were estimated from experimental data, [146] revealed no significant variation of the signal maximum. These results illustrate that a general theoretical approach taking into account all degrees of freedom and an approximate description of the transition dipole moments for ionization is mandatory for the detailed investigation of the time-dependent photoionization processes in pyrazine. Therefore, in this chapter the simulated TRPES spectrum of pyrazine employing both the discretized description of the electronic continuum (DC) obtained from TDDFT and the combination of TDDFT with the Stieltjes imaging (SI) procedure is presented.

The chapter is structured as follows: First, the computational aspects are described. Subsequently, the comparison of the simulated stationary absorption spectrum obtained from TDDFT with the experiment from the group of Prof. Suzuki (Kyoto University, Kyoto, Japan) is presented. Finally, simulations of the ultrafast nonadiabatic dynamics and of the TRPES spectrum of pyrazine are discussed. The close collaboration with the Suzuki group provided the opportunity for the validation of the theoretical approach by comparison with experimental TRPES results. [83]

## 6.2 Computational and Experimental Methods

The photodynamics of pyrazine was simulated following the approach for the nonadiabatic dynamics in the frame of TDDFT as outlined in Chapter 2. For the simulations, the ground state and the four lowest excited states were taken into account. For this purpose, the hybrid B3LYP [88,169] functional was employed in combination with the triple-$\zeta$ valence plus polarization (TZVP) atomic basis sets [190] as implemented in the Turbomole program. [96] In order to check the accuracy of B3LYP for the description of the low-lying excited states of pyrazine, the stationary absorption spectrum as obtained from TDDFT was compared with both the results from the more accurate EOM-CCSD(T) method and experiment. As will be presented in Section 6.3, the results yield a reasonable agreement.

The 60 initial conditions for the nonadiabatic dynamics were sampled from a canonical Wigner distribution at $T = 260\,\mathrm{K}$ according to Eq. 2.34, taking into account all degrees of freedom. In order to examine whether higher vibrational states are occupied at the simulation temperature, the populations of the vibrational states were calculated from their vibrational temperature. The results indicate that even for the lowest vibrational mode exhibiting a vibrational temperature of 492 K, the $v = 1$ state is only populated by 15 %. For the higher normal modes, the $v = 1$ state is populated by less than 1 %. Therefore, it can be assumed that at the simulation temperature only the vibrational ground state ($v = 0$) is occupied, which corresponds to the experimental conditions in a

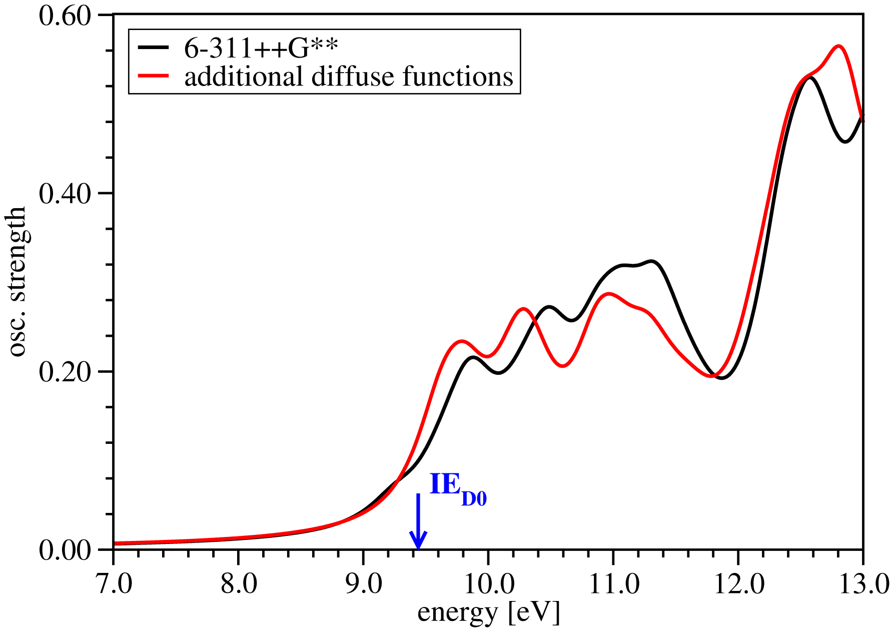

Figure 6.2: Comparison of the absorption spectra of neutral highly excited states above the ionization threshold for pyrazine employing the 6-311++G** basis set (black) and employing additional diffuse functions at the molecular center (red). The blue arrow indicates the ionization energy to the cationic ground state ($\mathrm{IE}_{\mathrm{D0}}$).

supersonic molecular beam.

The TRPES spectrum of pyrazine was simulated employing both the DC approach and the SI procedure as outlined in Chapter 3. In order to demonstrate the influence of the theoretical approach on the appearance of the TRPES spectra, the resulting spectra were also compared with those obtained taking into account only the cationic ground state and constant transition dipole moments. For the simulations using the SI and DC approaches, up to 200 transition energies and transition dipole moments were calculated with TDDFT densely covering the energy range between the ionization threshold and the experimental probe plus energy ($E_{pr} = 6.26\,\mathrm{eV}$). For this purpose, the hybrid B3LYP functional[88,169] and the 6-311++G** atomic basis set[216] containing diffuse functions were employed. The influence of the basis set on the neutral absorption spectrum of pyrazine was investigated by adding additional diffuse functions at the center of the molecule. The comparison of the results obtained from the augmented 6-311++G** basis set with the results employing the original basis set are presented in Figure 6.2. It can be seen that the influence of these additional functions in the energy range up to $\sim 4\,\mathrm{eV}$ above the ionization energy ($\mathrm{IE}_{\mathrm{D0}}$) is small.

The SI procedure was carried out as described in Section 3.3.2 using 200 spectral moments for selected time steps in the nonadiabatic dynamics. In order to take into account the experimental resolution and to obtain continuous TRPES spectra, the spectra for selected time delays $t_D$ obtained from either the DC or the SI approach were convoluted with a Gaussian spectral profile. For this purpose, the experimental full width at half maximum value of 22 fs (corresponding to $\sigma = 9.34$ fs) for the cross-correlation between the pump and the probe pulses was used for the time domain and a width of $\sigma = 0.2$ eV for the energy domain.

Since the presented theoretical study was performed in close collaboration with the experimental work done in the group of Prof. Suzuki, the experimental setup is briefly characterized (for details see Reference [83]). The experimental time-resolved photoelectron imaging (TRPEI) was performed with sub-20 fs pump and probe pulses with energies of 6.26 eV and 4.70 eV, respectively, which were generated by the multi-color filamentation method.[217,218] A Ti:sapphire multipass amplifier was employed as a light source. The resulting pulse widths were characterized as 14 fs for the 4.70 eV and 17 fs for the 6.26 eV pulse with energies reduced to 0.5 $\mu$J and 0.1 $\mu$J, respectively. The two pulses were vertically displaced after the grating compressor and the delay time $t_D$ between the pulses was controlled with a closed-loop translation stage exhibiting an accuracy of 5 nm. As in standard TRPEI experiments,[68] the linear polarization directions of the pump and probe laser beams were aligned parallel to each other and also set parallel to the face of the detector. The resulting photoelectron images were measured at 10 fs intervals in delay time.

## 6.3 Electronic Properties

Figure 6.3 presents the comparison of the theoretical and experimental stationary absorption spectra of pyrazine at room temperature. For the theoretical spectrum, the absorption spectra of 650 initial conditions sampled from a Wigner distribution at $T = 260$ K were calculated with B3LYP/TZVP. The first transition ($S_1$) with relatively weak intensity centered at 3.9 eV is of $n - \pi^*$ character and corresponds to the $1^1B_{3u}$ state. The dominant transition ($S_2$) is located around 5.3 eV. This transition exhibits $1^1B_{2u}$ symmetry and predominantly $\pi - \pi^*$ character, as depicted in Figure 6.4. In addition to the optically allowed $S_1$ and $S_2$ states, two dark states with $n - \pi^*$ character are present, which exhibit $1^1A_u$ and $1^1B_{2g}$ symmetry. They are located at 4.6 eV and 6.3 eV, respectively. All four states have to be taken into account for the nonadiabatic dynamics simulations. The theoretical and experimental spectra shown in Figure 6.3 agree well for the $S_1$ state. The $S_2$ state obtained from TDDFT is shifted by $\sim 0.5$ eV to higher energies with respect to the experiment. Notice that due to the classical approach of the simulation only the envelope of the experimental spectrum can be reproduced.

Table 6.1 provides the comparison of the absorption energies for the $S_1$ and $S_2$ states of pyrazine obtained from B3LYP with the more accurate EOM-CCSD(T) and experimental results.[237] As can be seen, the transition energies for the $S_1$ state are in excellent agreement within both theoretical methods. In contrast, the B3LYP transition energy of the $S_2$ state is shifted to higher energies with respect to EOM-CCSD(T) results. However, also the EOM-CCSD(T) transition energy is shifted with respect to the experimental absorption spectrum. In order to examine if the $S_1$ and $S_2$ states of pyrazine

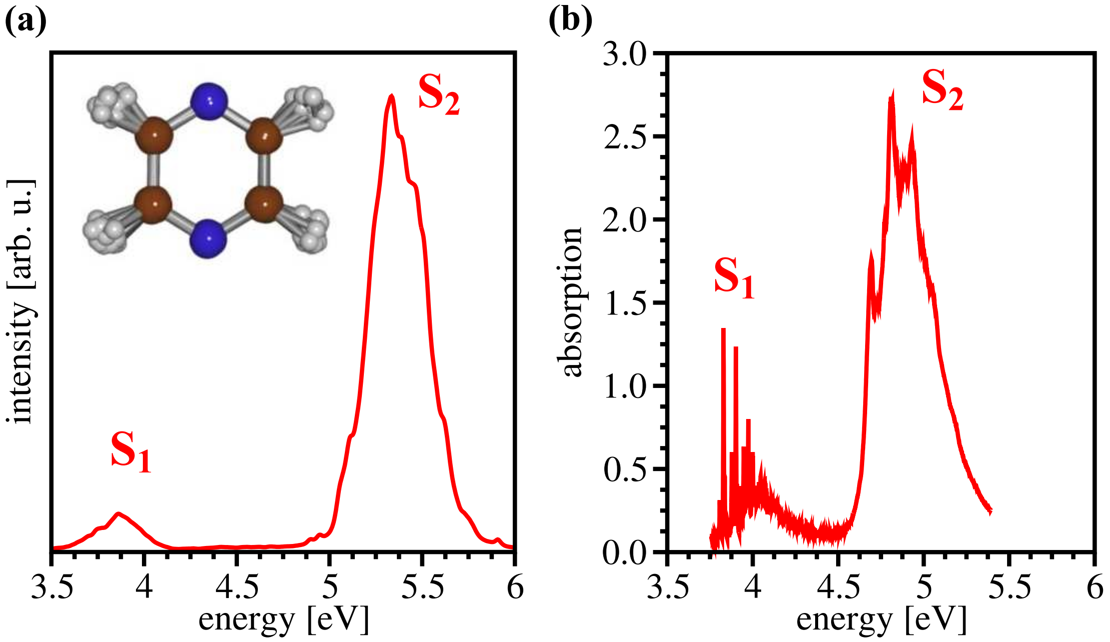

Figure 6.3: Comparison of the stationary absorption spectra for pyrazine obtained from (a) TDDFT at $T = 260\,\mathrm{K}$ and (b) experimental UV absorption spectroscopy at room temperature. For the theoretical spectrum, the discrete absorption lines for the ensemble presented in the inset were calculated with the B3LYP functional and subsequently convoluted with a Lorentzian function of 0.04 eV width.

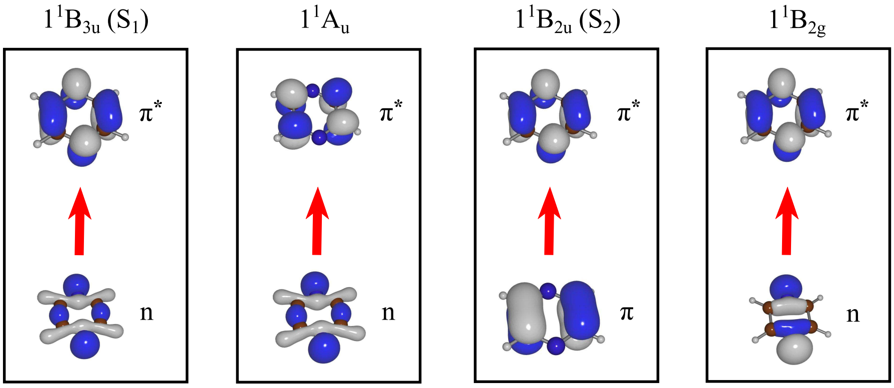

Figure 6.4: Character of the four lowest excited states ($1^1B_{2u}$, $1^1A_u$, $1^1B_{3u}$, and $1^1B_{2g}$) in pyrazine, indicated by the dominant orbitals involved in the transition.

exhibit long-range charge-transfer character, which represents a well known problem for the TDDFT (cf. Section 1.2.2), both states were analyzed by calculating the indicator quantity $\Lambda$. As outlined in Section 1.2.2, this quantity can serve as an indicator for the long-range charge-transfer contribution to electronic transitions.[95] The calculated values of 0.62 for the $S_1$ state and 0.69 for the $S_2$ state indicate that both transitions exhibit predominantly local characters within the B3LYP method. Thus, the charge-transfer contribution is not dominant and B3LYP is expected to provide a reasonable description.

Table 6.1: Comparison of calculated vertical transition energies for the $S_1$ and $S_2$ states of pyrazine (in eV).

| **Method** | $\mathbf{S_1}(\mathrm{n}-\pi^*)$ | $\mathbf{S_2}(\pi-\pi^*)$ |
|---|---|---|
| B3LYP | 3.96 | 5.46 |
| EOM-CCSD(T)[a] | 3.95 | 4.64 |
| Exp.[b,c] | 3.83/3.87 | 4.81/4.80 |

[a] Ref. [237], [b] Ref. [238], [c] Ref. [239]

## 6.4 Nonadiabatic Dynamics

The ultrafast relaxation in pyrazine was examined by employing the TDDFT based approach for the nonadiabatic dynamics. Since the $S_2$ state exhibits a remarkably strong intensity in the low energy regime of the absorption spectrum (cf. Section 6.3), pyrazine is expected to be mainly excited to this state in the experiment.

Figure 6.5 presents the time-dependent populations of the four lowest excited states after initial excitation into the $S_2$ state. This populations were obtained by monitoring the fraction of nonadiabatic trajectories in each state as a function of time. As can be seen, the $S_2$ population is transferred into the three other considered excited states ($S_1$, $1^1A_u$, and $1^1B_{2g}$), while no population transfer to the ground state ($S_0$) can be identified during the simulations. The lifetime of the $S_2$ state can be approximated by an exponential decay yielding a time constant of 21 fs, as depicted in Figure 6.6(a). In order to determine the accuracy of the TDDFT-nonadiabatic dynamics approach, the time evolution of the $S_2$ population is compared in Figure 6.6 with the results obtained from quantum dynamics simulations by Puzari et al.,[234] who employed the time-dependent discrete variable representation (TDDVR) method. In the TDDVR simulations, 12 vibrational modes were explicitly included and the remaining modes were treated as harmonic oscillator heat bath modes. The decay of the TDDFT $S_2$ population agrees well with the full quantum dynamical results. Furthermore, the TDDFT lifetime of 21 fs is in perfect agreement with both the lifetime of approximately $\sim$ 20 fs obtained from TDDVR (cf. Fig. 6.6(b)) and with the experimental value of 22 fs. These results demonstrate that the nonadiabatic dynamics simulation in the frame of TDDFT, which allows for including all degrees of freedom, provides an accurate description of ultrafast photoinduced relaxation processes.

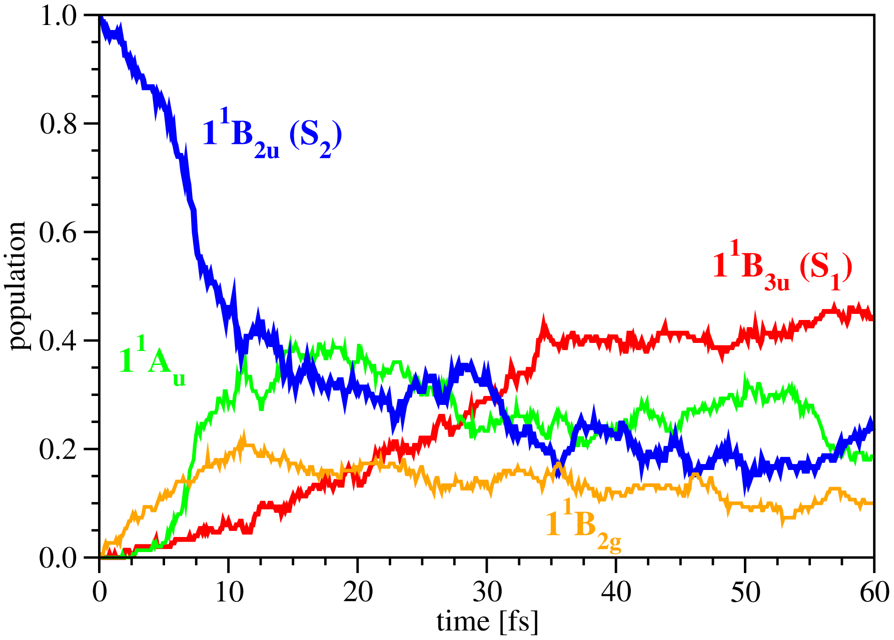

Figure 6.5: Time evolution of the excited state populations of pyrazine after excitation to the $S_2$ state: $1^1B_{3u}$ ($S_1$) (red), $1^1A_u$ (green), $1^1B_{2u}$ ($S_2$) (blue) and $1^1B_{2g}$ (orange).

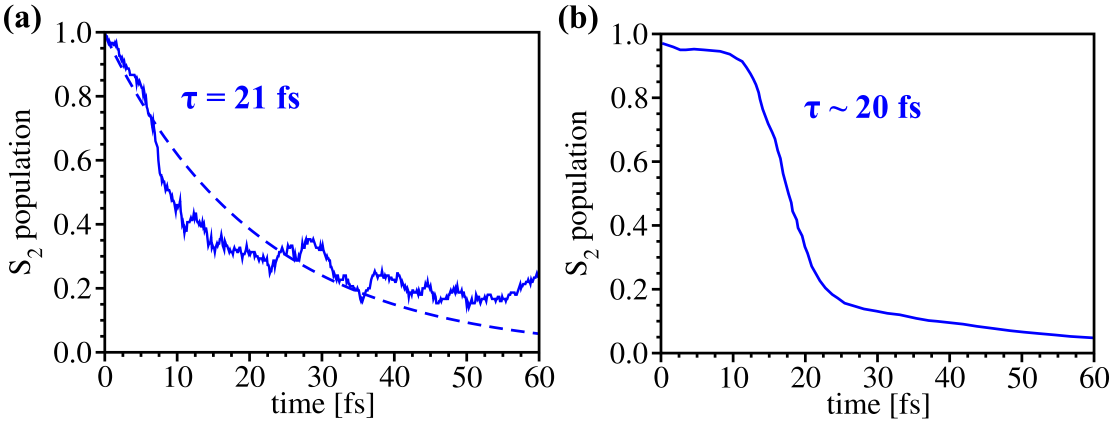

Figure 6.6: Comparison of the time-dependent population of the $S_2$ state of pyrazine (a) obtained from the TDDFT approach and (b) according to the results of Puzari et al.[234] using a numerical quantum mechanical treatment (TD-DVR). The lifetime of the $S_2$ state in (a) was determined by exponential fitting (dashed line) to be 21 fs and was approximated as 20 fs for (b).

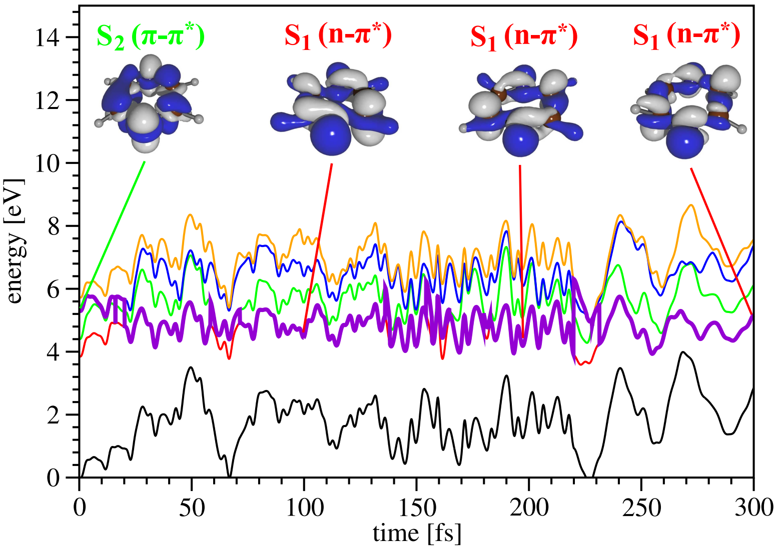

Figure 6.7: Time evolution of the ground (black) and four lowest excited states (red $S_1$, green $1^1A_u$, blue $S_2$, and orange $1^1B_{2g}$) obtained from the nonadiabatic dynamics along one selected trajectory. The thick violet line indicates the energy of the state in which the trajectory resides during the dynamics. The insets illustrate the characters of the electronic states by the electron density differences between ground and given excited state.

To provide a detailed picture of the nonadiabatic processes, the time evolution of the excited states along one selected trajectory was analyzed. As depicted in Figure 6.7, the electron density difference for selected time steps during the dynamics indicates a switch from the initially excited $S_2$ $(\pi-\pi^*)$ state to the $S_1$ $(\mathrm{n}-\pi^*)$ state at 20 fs. This agrees well with the lifetime of the $S_2$ state ($\tau = 21$ fs). Figure 6.7 also shows that the energies of the four excited states are well separated from the ground state during the entire simulation period, thus providing an explanation for the absence of population transfer to the ground state.

The time evolution of the diabatic populations was estimated from the time-dependent oscillator strength, since it reflects the nature of the photodynamics. As the $\pi-\pi^*$ state of pyrazine exhibits a high oscillator strength with respect to the $\mathrm{n}-\pi^*$ states, a high average oscillator strength indicates population in the $\pi-\pi^*$ state. In contrast, a low average oscillator strength indicates population in the $\mathrm{n}-\pi^*$ states. The results depicted in Figure 6.8 illustrate that the oscillator strength and thus the $\pi-\pi^*$ state decay within the first 50 fs, with a recurrence at $\sim 75$ fs. In comparison to the adiabatic $S_2$ state ($\tau = 21$ fs), the decay of the diabatic $\pi-\pi^*$ occurs on a slower timescale. This is also in agreement with the results of the TDDVR simulations in Reference [234].

In order to identify the normal modes that are responsible for the ultrafast relaxation in pyrazine, the time-dependent Cartesian coordinates for the entire ensemble were projected onto the normal modes of pyrazine in its equilibrium structure. The time evolution

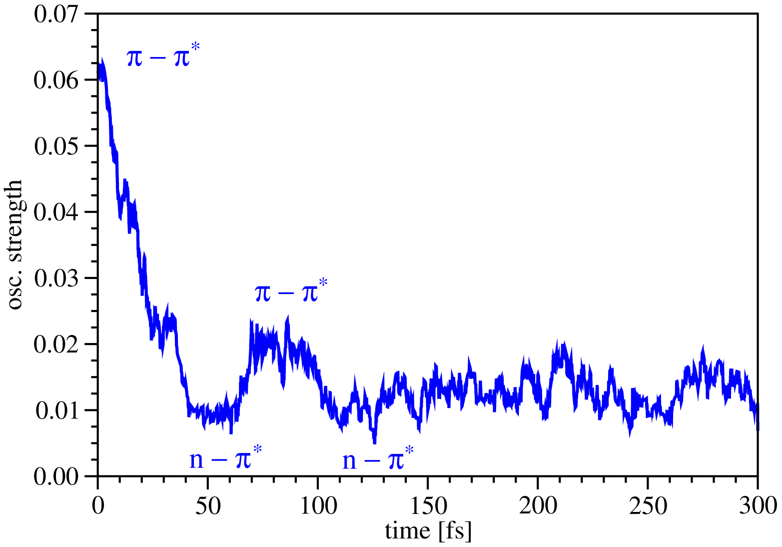

Figure 6.8: Time-dependent oscillator strength for the transitions from the $S_0$ state to the excited state in which dynamics takes place averaged over the ensemble of trajectories. The population of the diabatic states can be estimated, since the $\pi - \pi^*$ state exhibits a high oscillator strength in contrast to the $\mathrm{n} - \pi^*$ states.

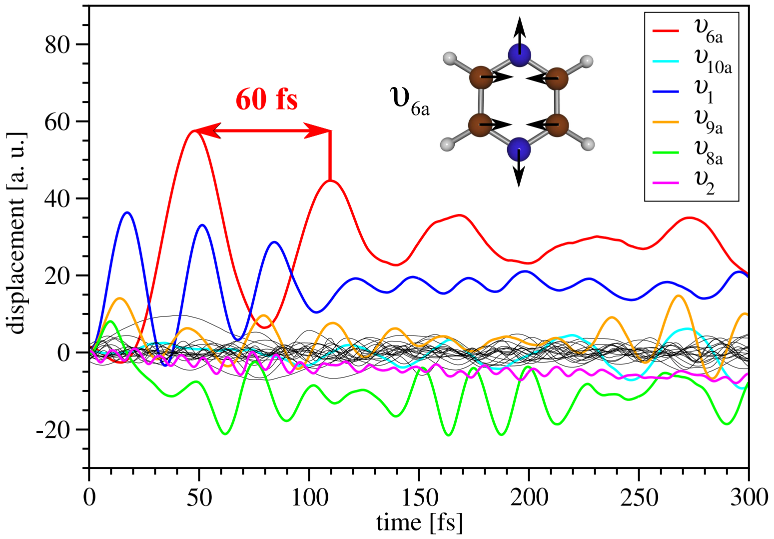

Figure 6.9: Averaged time-dependent normal mode displacements obtained by projection of the time-dependent Cartesian coordinates of the ensemble onto the normal coordinates of pyrazine in its equilibrium configuration. The displacement of the dominant normal mode $\nu_{6a}$ exhibits a periodicity of $\sim 60\,\mathrm{fs}$.

of the averaged values depicted in Figure 6.9 shows that several modes are excited during the dynamics. These modes are labeled in the Wilson notation as $\nu_1$, $\nu_2$, $\nu_{6a}$, $\nu_{8a}$, $\nu_{9a}$, and $\nu_{10a}$. The totally symmetric $\nu_{6a}$ mode can be identified as the leading mode for the relaxation. This mode mainly involves the in-plane motion of the carbon and nitrogen atoms with a period of $\sim 60$ fs, as illustrated in the inset of Figure 6.9.

## 6.5 Time-Resolved Photoelectron Spectrum

In order to investigate the influence of the accuracy for the description of photoionization on the TRPES spectrum of pyrazine, simulations based on two different levels of approximation were performed:

1. The TRPES spectrum was simulated based on the assumption that ionization occurs to the cationic ground state ($D_0$) with constant transition dipole moments ($D_0$-TRPES). For this simulation the time-dependent energy gaps between the given excited state during the nonadiabatic dynamics and $D_0$ were determined for the entire ensemble of 60 nonadiabatic trajectories.

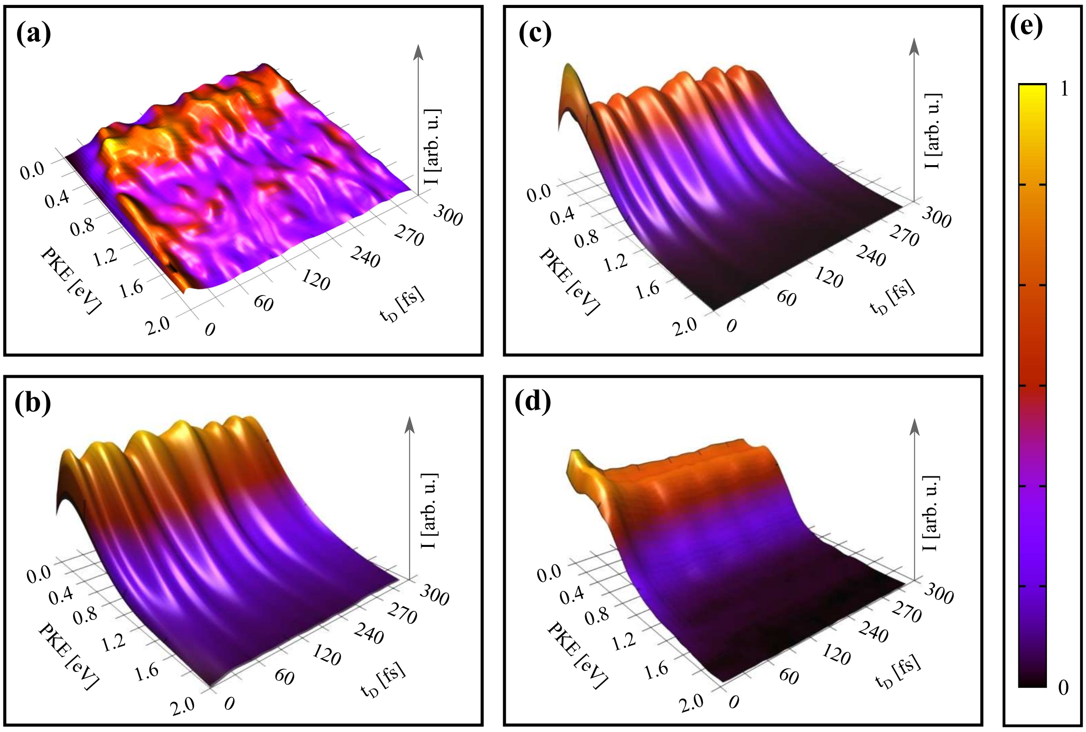

Figure 6.10: Comparison of simulated TRPES spectrum obtained from (a) $D_0$-TRPES, (b) DC, (c) SI, and (d) experiment. The spectra (a)-(d) were independently normalized with respect to the highest peak. (e) Color scale for the signal intensities.

2. Taking into account an approximate description for the ionization probabilities, both the DC and the SI approaches were employed for the simulation of TRPES.

The $D_0$-TRPES presented in Figure 6.10(a) exhibits a systematic shift of the maximum intensity from a PKE interval of 2.0 - 1.0 eV to ∼ 0.4 eV on a timescale of 20 fs. This reflects the main population transfer from the $S_2$ state ($IE_{equ.} = 4.0$ eV, calculated at the equilibrium geometry) over the $1^1A_u$ into the $S_1$ state ($IE_{equ.} = 5.5$ eV). This timescale is in agreement with both the lifetime of 21 fs for the $S_2$ state obtained from the time-dependent populations (cf. Fig. 6.6(a)) and the experimental lifetime of 22 fs. In the subsequent time interval between 20 and 120 fs, the PKE remains approximately constant, which indicates that there is no population transfer back to the $S_2$ state within this time window. Due to the systematic shift of the TRPES signal to lower PKEs, which has also been identified in earlier simulations,[142] it has been proposed to use TRPES for the real-time observation of the $S_2 \rightarrow S_1$ IC in pyrazine.[142]

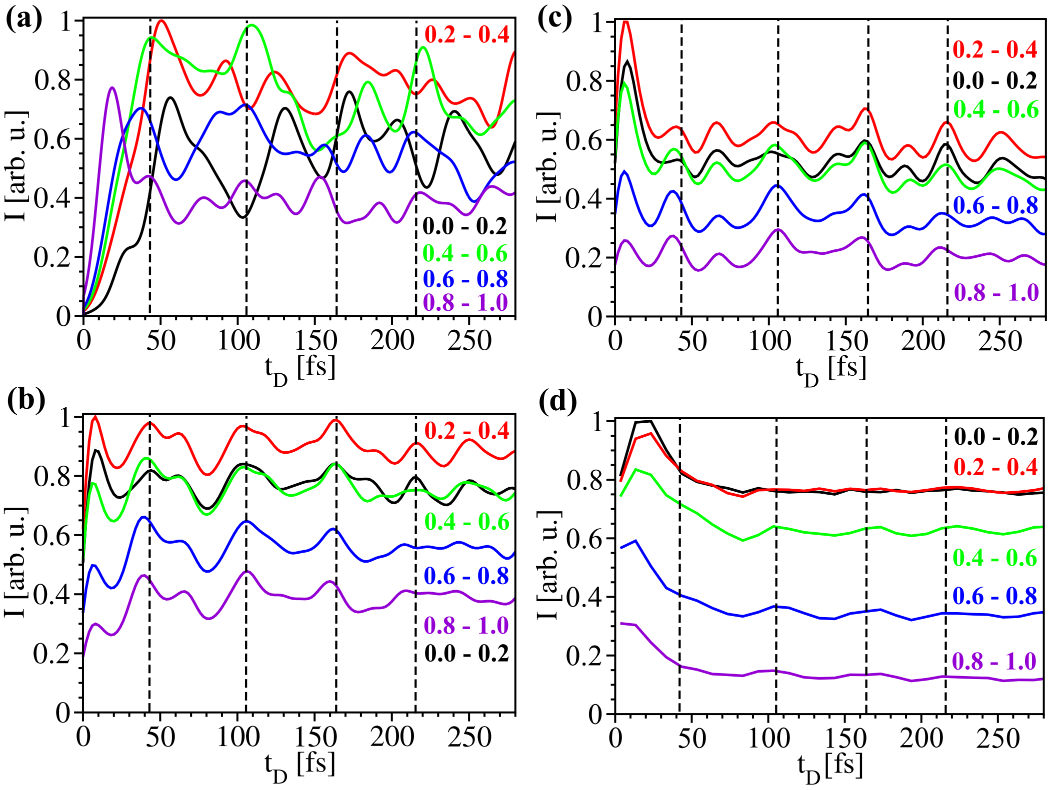

Figure 6.11: Time-dependent photoelectron signal intensities for different photoelectron kinetic energy (PKE) intervals obtained from (a) $D_0$-TRPES, (b) DC, (c) SI, and (d) experiment. The signals (a)-(d) were independently normalized with respect to the highest peak. The dashed lines indicate the quantum beats.

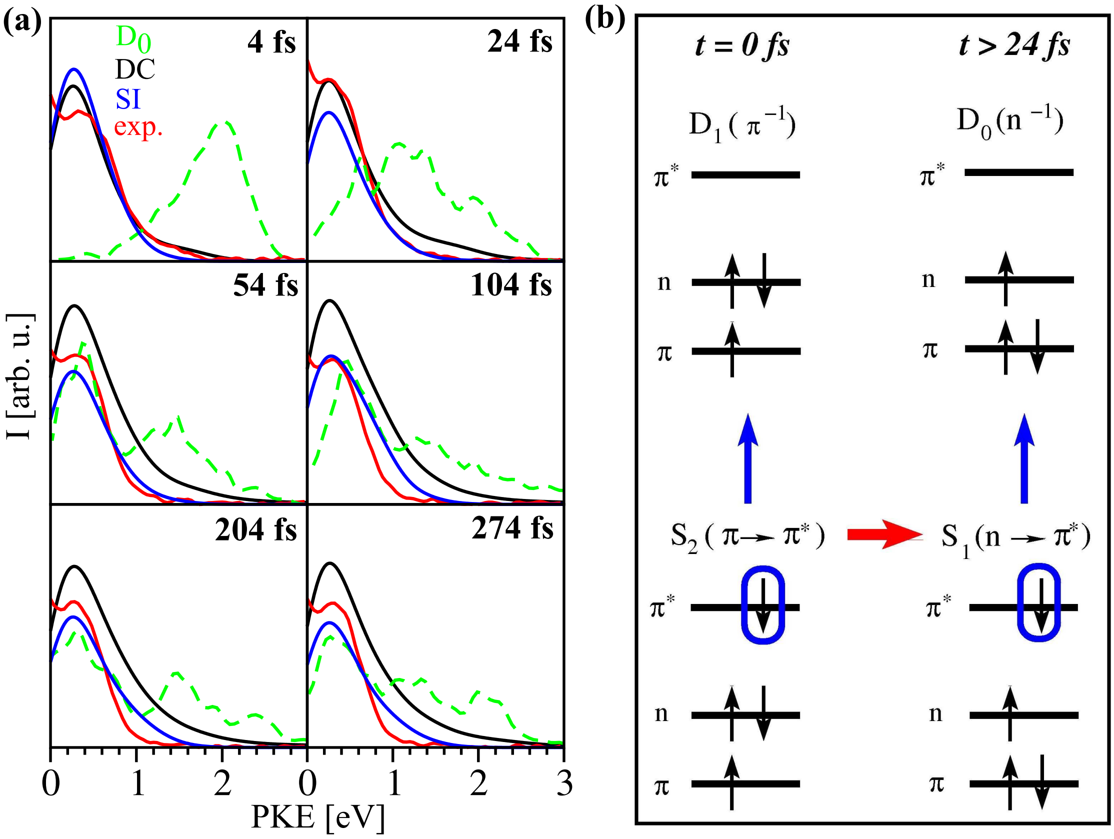

Figure 6.12: (a) Comparison of photoelectron spectra for selected time delays obtained from $D_0$-TRPES (green, dashed line), DC (black), SI (blue), and experiment (red). The signals were independently normalized with respect to the highest peak. (b) Schematic analysis of time-dependent photoionization process in pyrazine.

In contrast, the DC and SI simulations presented in Figure 6.10(b) and (c), respectively, do not exhibit a systematic shift of time-dependent PKE. During the entire simulation period, the signal remains in an interval between 0 and 1.5 eV. These results are in agreement with the experimental measurements (cf. Fig. 6.10(d)) as well as with earlier dynamical simulations with reduced dimensionality, in which the transition dipole moments for ionization to the $D_0$ and $D_1$ cationic states have been estimated from experimental data.[146]

A more detailed analysis of the simulated and experimental TRPES spectra can be performed by analyzing the sections from TRPES spectra corresponding to selected PKE ranges. The average intensity for the slices of DC and SI spectra depicted in panels (b) and (c) of Figure 6.11, respectively, is highest for the 0.0 - 0.2 and 0.2 - 0.6 eV intervals and decreases with increasing PKE above 0.6 eV. These findings are in agreement with the experimental slices shown in panel (d). In contrast, no systematic relation between average intensity and PKE range is present in the $D_0$-TRPES provided in panel (a). While both the DC and SI spectra are very similar after $\sim$ 50 fs, the SI spectrum exhibits a more pronounced maximum at $\sim$ 10 - 20 fs in agreement with the experiment. The DC, SI and experimental signal exhibit quantum beats between 50 and 250 fs, which are indicated by dashed lines in Figure 6.11. They can be assigned to the normal mode $\nu_{6a}$ with a period of $\sim$ 60 fs, which was also identified as the leading mode for the nonadiabatic dynamics (cf. Fig. 6.9). However, the quantum beats are more pronounced in the DC and SI spectra with respect to the experiment.

In order to further analyze the influence of the approximate treatment of photoionization on the appearance of the signal, slices from the TRPES spectra for selected pump-probe time delays are presented in Figure 6.12(a). At the time delay $t_D = 4$ fs, the experimental as well as DC and SI signals are located around 0.5 eV. In contrast, the signal obtained from $D_0$-TRPES for this time delay is located at $\sim$ 2 eV. This deviation indicates that ionization from the initially occupied $S_2$ state to $D_0$ occurs only weakly in the experiment and in simulations in which ionization probabilities are taken into account. As time proceeds ($t_D > 24$ fs) a change in the ionization process takes place: After the $S_2 \rightarrow S_1$ IC has occurred ($\tau = 21$ fs), ionization from $S_1$ to $D_0$ dominates. This is reflected in the similarity of all three theoretical and the experimental spectra for the time delays $> 24$ fs. Investigation of the transition energies for the dominant ionization channels ($S_2 \rightarrow D_1$ and $S_1 \rightarrow D_0$) reveals that they are very close in energy. Therefore, no significant shift of the PKE distribution can be identified in both DC and SI simulations in agreement with the experimental TRPES.

A schematic representation of the time-dependent photoionization processes in pyrazine based on the one-electron picture extracted from the simulations, is provided in Figure 6.12(b). The dominant configuration at $t = 0$ fs, which can be identified from the nonadiabatic dynamics (cf. Fig. 6.7), corresponds to the $S_2$ state. In the one-electron picture, ejection of the electron from the highest occupied molecular orbital produces the cationic $D_1$ state (cf. left hand side of panel (b)). In contrast, the main configuration after IC ($t_D > 24$ fs) is the $S_1$ state, which in the one-electron picture ionizes to $D_0$ as illustrated on the right hand side of panel (b). Notice that the wavefunction is a superposition of many configurations. Thus, an ionization process which is forbidden in the one-electron single determinant picture can become weakly allowed due to the minor contribution of other configurations.

The fact that the time-dependent photoionization in pyrazine occurs to several cationic states with varying ionization probabilities (preferential to $D_1$ at $t_D \sim 0$ fs and to $D_0$ at $t_D > 24$ fs) clearly demonstrates that the approximate description of the ionization probabilities to different cationic states is necessary for the accurate simulation of photoionization processes.

## 6.6 Summary

The accuracy of the nonadiabatic dynamics “on the fly” based on the combination of the Tully’s surface hopping procedure and TDDFT has been demonstrated by simulating the nonradiative ultrafast internal conversion between the $S_2$ and $S_1$ states in pyrazine. This approach allowed for the determination of the nonradiative lifetime of the $S_2$ state as 21 fs.[39] The results are in excellent agreement with both the experimental value of 22 fs as well as with quantum dynamical simulations.[234] Moreover, the scope of the theoretical approach combining the TDDFT nonadiabatic dynamics with an approximate description of the electronic continuum based on TDDFT as well as its implementation within the Stieltjes imaging procedure was illustrated on the simulated TRPES spectrum of pyrazine. It was shown that the $S_2 \rightarrow S_1$ IC leads to a change in the transition probabilities: The initial ionization from the $S_2$ to the $D_1$ state turns over continuously to the ionization from the $S_1$ to the $D_0$ state.[84] This demonstrates that the approximate description of ionization possibilities into ionization continua corresponding to different cationic states is mandatory for the accurate simulation of photoionization processes. Since both ionization channels exhibit similar ionization energies, the maximum of the simulated photoelectron distribution remains in an almost constant energy range. The agreement of simulated TRPES spectra obtained from both approaches DC and SI validates the use of SI, which is particularly beneficial if the spectral moments can be efficiently calculated without full diagonalization of the Hamiltonian matrix. The presented results demonstrate that the theoretical approach for the simulation of nonadiabatic dynamics and TRPES spectra in the frame of TDDFT provides a quantitative agreement with experimental measurements. Therefore, it represents a viable tool for the investigation and interpretation of the time-dependent photoionization processes in complex systems.

# 7 Nonadiabatic Dynamics of Isolated and Microsolvated Adenine

## 7.1 Introduction

The high photostability of DNA has been intensively explored in recent years and is usually attributed to the presence of efficient ultrafast nonradiative deactivation channels. The nucleobases, which serve as the chromophores in DNA, strongly absorb in the 200 - 300 nm spectral range. Therefore, they are potentially vulnerable to UV irradiation. Thus, in order to prevent destruction of the DNA, the nucleobases should be able to efficiently dissipate the absorbed radiation into the vibrationally excited ground state.[240–244] Experimental studies on the DNA base adenine, which is often taken as a prototype example for this behavior, have shown that deactivation of gas-phase adenine after excitation of the strongly absorbing $\pi - \pi^*$ state occurs within $\sim 1$ ps.[75,80,245,246] Numerous theoretical studies have been performed on gas-phase adenine, aiming to identify the conical intersections which dominate this relaxation process.[241,244,247–252] For excitations close to the absorption maximum of adenine ($\sim 5$ eV), two competing decay mechanisms involving two different conical intersections have been discussed: 1) Relaxation from the initially excited $\pi - \pi^*$ state over the first excited $\mathrm{n} - \pi^*$ state into the ground state[41,247,250,253] and 2) direct decay of the excited $\pi - \pi^*$ state into the ground state.[247,248,250,251,253,254] Alternatively, a decay mechanism involving the $\pi - \sigma^*$ state was proposed in earlier theoretical calculations[241,248] and was assigned to minor channels in experiments with transition energies $> 5.3$ eV or $\sim 4.6$ eV.[75,80,255]

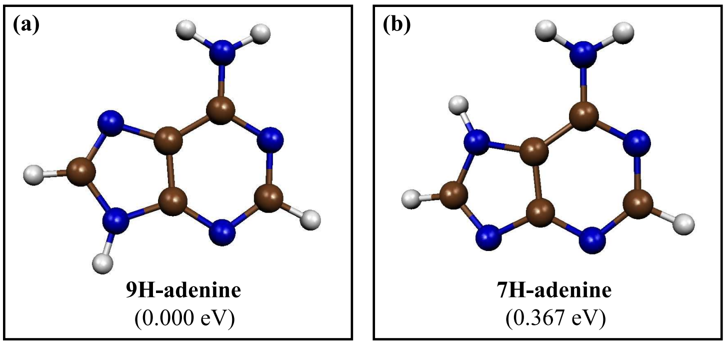

Figure 7.1: Structures for the (a) 9H- and (b) 7H-adenine tautomers optimized with the hybrid B3LYP functional. The relative energies of the tautomers are given in parenthesis.

In order to provide a dynamical picture of the nonradiative processes in adenine, mixed quantum-classical dynamics simulations were carried out recently using both the high-level ab initio multi-reference configuration interaction (MRCI) method [254] and the semiempirical CI method. [41] Moreover, simulations based on DFTB combined with the Ehrenfest treatment of the nonadiabatic dynamics have been performed. [253] According to these theoretical studies, the relaxation proceeds in a two-step process. First, the initially excited $\pi-\pi^*$ state decays into the lowest excited state with $\mathrm{n}-\pi^*$ character on a short timescale (15 - 100 fs). The second, slower step corresponds to the transition from the $\mathrm{n}-\pi^*$ state to the electronic ground state with a time constant of approximately 0.5 -1.4 ps. [41,253,254]

In contrast to the detailed knowledge about the radiationless decay mechanism in the gas phase, much less is known about the photodynamics of adenine in solution. Experimental studies have revealed that the lifetime of the $\mathrm{S}_1$ state of adenine in water (180 fs) is much shorter than in the gas phase. [256] These findings show that a realistic picture of the photodynamics of nucleobases requires the description of solvent effects, which still represents a serious theoretical challenge. In this thesis, the relaxation dynamics in gas-phase adenine was simulated and compared to microsolvated adenine. The results allow for the first time to determine the influence of solvent on the photoinduced relaxation process in adenine. [63]

In this chapter, the nonadiabatic dynamics of microsolvated adenine will be presented in order to demonstrate that nonadiabatic dynamics in the frame of the time-dependent density functional theory tight binding (TDDFTB) is suitable for the simulation of photodynamics in complex systems such as solvated biochromophores. This chapter is structured as follows: First, the computational aspects are shortly outlined followed by structural and electronic properties of gas-phase adenine. Subsequently, the nonadiabatic dynamics of isolated adenine is discussed and compared to previous theoretical and experimental findings. Finally, the simulations of the ultrafast nonradiative relaxation of microsolvated adenine are presented.

## 7.2 Computational Methods

The photodynamics of gas-phase and microsolvated adenine were simulated by using the nonadiabatic dynamics based on TDDFTB as outlined in Chapter 2. The electronic ground state and the four (isolated adenine) or respectively seven (microsolvated adenine) lowest excited states were taken into account. The accuracy of TDDFTB for the description of excited states of isolated and microsolvated adenine was carefully checked by comparing the results with other quantum chemical methods (cf. Section 7.3 and 7.5 for details). The initial conditions for the simulations of the nonadiabatic dynamics were sampled from molecular dynamics trajectories propagated with DFTB (isolated adenine) or the DFT method employing the PBE functional (microsolvated adenine) in the neutral ground state at a constant temperature of $T = 300\,\mathrm{K}$.

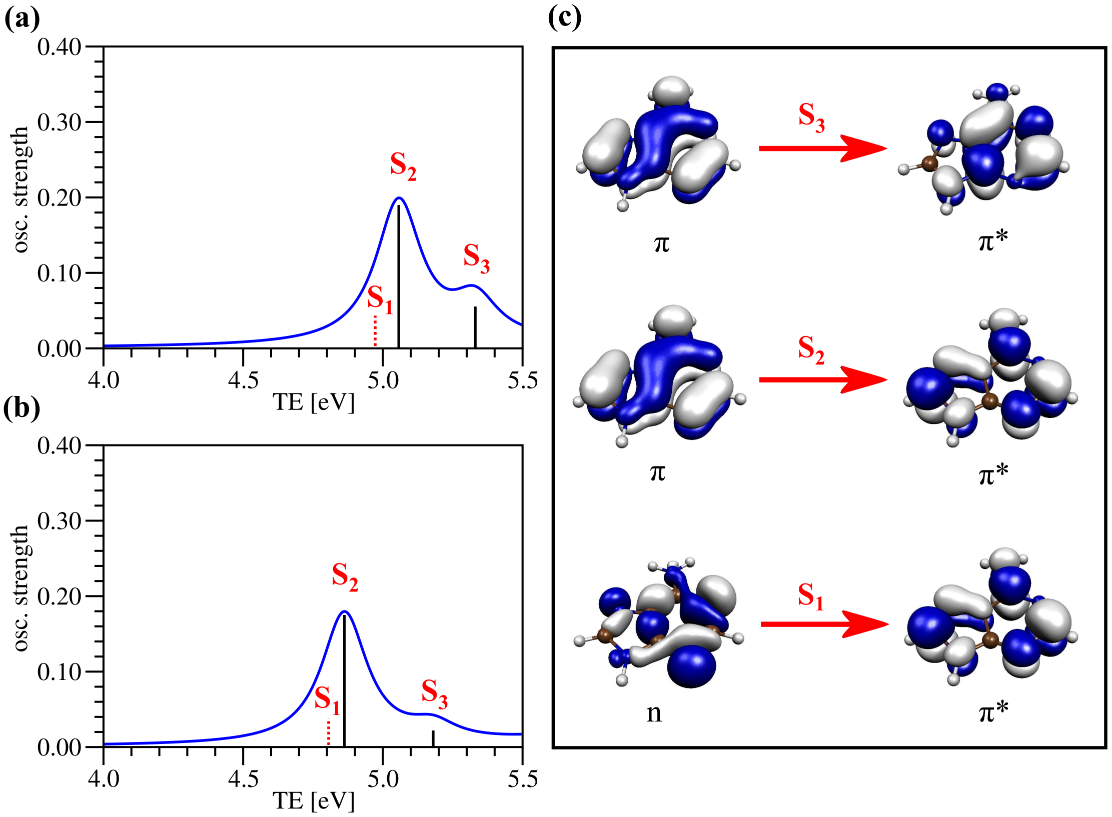

Figure 7.2: Comparison of the calculated absorption spectra of adenine obtained (a) with the hybrid B3LYP functional and (b) at the TDDFTB level of theory. The energy of the dark $S_1$ state is indicated by a dashed red line. (c) Character of the $S_1$ $(n-\pi^*)$, the $S_2$ $(L_a, \pi-\pi^*)$, and the $S_3$ $(L_b, \pi-\pi^*)$ excited states of adenine, indicated by the orbitals mainly involved in the transitions.

## 7.3 Structural and Electronic Properties of Gas-Phase Adenine

The optimized structures for the two most stable tautomers 9H- and 7H-adenine as well as their relative energies obtained using the B3LYP functional[88,169] and triple-$\zeta$ valence plus polarization (TZVP) basis set[96] are presented in Figure 7.1. The 9H-tautomer is 0.367 eV more stable in energy and has been experimentally proven to be the dominant species in the gas phase.[257] Thus, this tautomer was employed for the simulation of absorption spectra and nonadiabatic dynamics.

The comparison of the absorption spectra for 9H-adenine obtained with the TDDFT method using the B3LYP functional and with the TDDFTB method is provided in Figure 7.2(a) and (b). As can be seen, the agreement of both spectra is good despite a shift of $\sim 0.2$ eV for the TDDFTB spectrum to lower energies with respect to the B3LYP spectrum. Figure 7.2(c) shows that with both methods the dark $S_1$ state assumes $n-\pi^*$

Table 7.1: Comparison of vertical transition energies for the $n - \pi^*$, $L_a$, and $L_b$ states of adenine (in eV). The oscillator strengths for the transitions are given in parenthesis.

| **Method** | $n - \pi^*$ | $L_a$ $(\pi - \pi^*)$ | $L_b$ $(\pi - \pi^*)$ |
|---|---|---|---|
| B3LYP (TDDFT ) | 4.95 (0.000) | 5.06 (0.189) | 5.33 (0.054) |
| TDDFTB | 4.61 (0.000) | 4.86 (0.174) | 5.18 (0.022) |
| OM2$^a$ | 4.58 (0.000) | 4.66 (0.210) | 4.97 (0.140) |
| CASPT2$^b$ | 4.96 (0.004) | 5.35 (0.175) | 5.16 (0.004) |
| MR-CIS$^c$ | 5.29 | 5.56 | 5.43 |
| exp$^d$ | - | 4.98/4.76 | |

$^a$ Ref. [41], $^b$ Ref. [251], $^c$ Ref. [254], $^d$ Ref. [240, 258]

character, $S_2$ is the bright $L_a$ $(\pi - \pi^*)$ state and $S_3$ is the $L_b$ $(\pi - \pi^*)$ state with a much lower oscillator strength than the $S_2$ state.

The comparison of the transition energies for the lowest three states of adenine obtained from B3LYP and TDDFTB with theoretical values from literature as well as with experimental results is provided in Table 7.1. The lowest state is the dark $n - \pi^*$ state for all of the methods, followed by either the bright $L_a$ $(\pi - \pi^*)$ or the $L_b$ $(\pi - \pi^*)$ state. The precise ordering for the lowest excited states is difficult to determine, since the result depends on the theoretical method (cf. Table 7.1). While for TDDFT, TDDFTB and semiempirical CI [41] the second excited state is $L_a$, $L_b$ is the second excited state in the case of CASPT2 [251] and MR-CIS. [254] However, the difference of the transition energies is quite small for all of the methods and no clear experimental evidence for the ordering of the two $\pi - \pi^*$ states is available. According to Fabiano et al., the nonadiabatic dynamics is not sensitive to the original state ordering, since the ordering changes during the dynamics. Moreover, the excited states rapidly acquire mixed characters after vertical excitation due to the presence of a conical intersection between $n - \pi^*$ and $L_a$ $(\pi - \pi^*)$. [41] Thus, TDDFTB is expected to provide a reasonable description for the nonadiabatic dynamics simulation.

## 7.4 Nonadiabatic Dynamics of Gas-Phase Adenine

The theoretical stationary absorption spectrum of gas-phase adenine including the temperature broadening at the simulation temperature of $T = 300\,\mathrm{K}$ is presented in Figure 7.3. Comparison with the experimental spectrum of Callis et al. [240] as well as with the semiempirical CI spectrum of Fabiano et al. [41] yields a good agreement despite a shift of $\sim 0.2\,\mathrm{eV}$ with respect to the experiment.

In order to study the ultrafast relaxation of gas-phase adenine, nonadiabatic dynamics were performed with the TDDFTB method. The time-dependent populations obtained from an ensemble of 200 initial conditions are presented in Figure 7.4(a). After initial excitation to the $S_2$ ($L_a$, $\pi - \pi^*$) state, the $S_2$ population decays approximately exponentially with a time constant of $\tau = 94\,\mathrm{fs}$ mainly into the $S_1$ $(n - \pi^*)$ state. Subsequently,

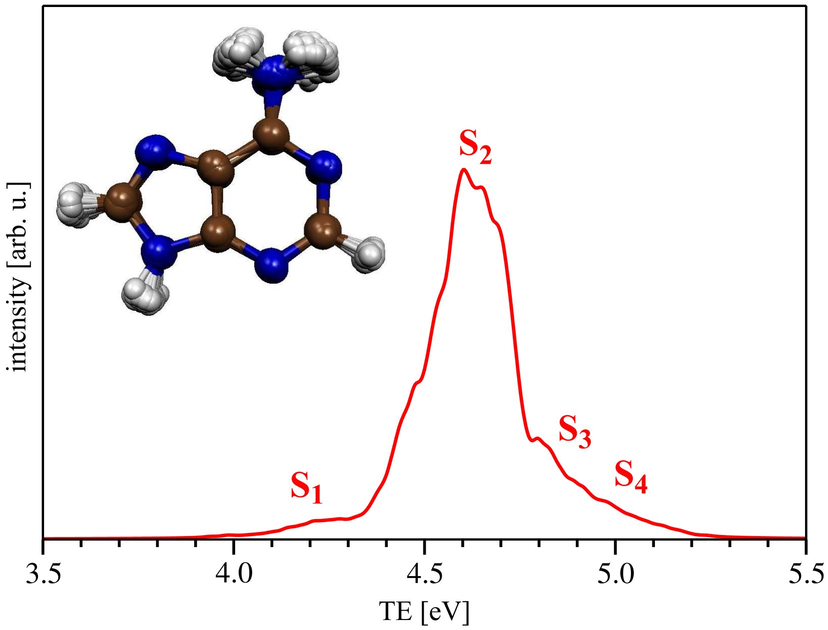

Figure 7.3: Thermally broadened stationary absorption spectrum for the four lowest excited states of adenine at $T = 300\,\mathrm{K}$. The discrete absorption lines for the ensemble presented in the inset were calculated with TDDFTB and convoluted with a Lorentzian function of 0.04 eV width.

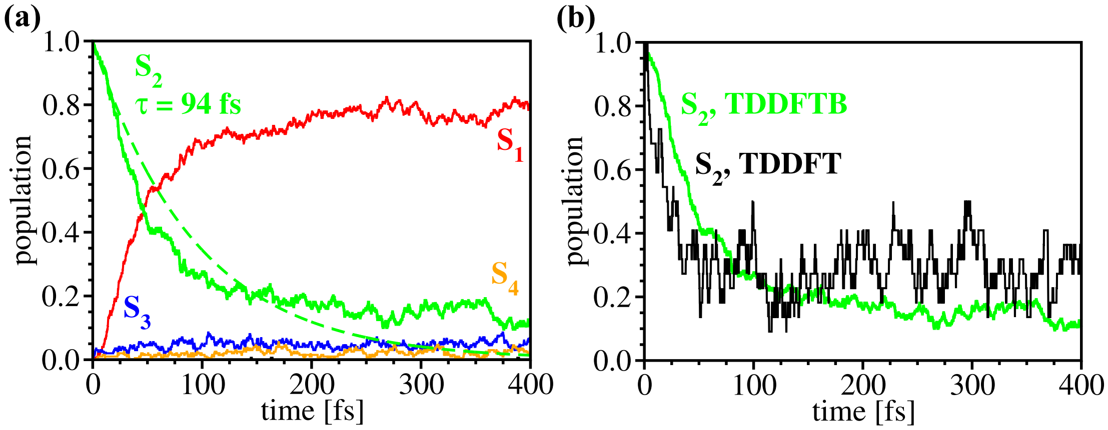

Figure 7.4: (a) Time-dependent adiabatic populations of the ground and four lowest excited states of adenine after excitation to the S$_2$ state. The lifetime $\tau$ of the S$_2$ state was determined by exponential fit (green dashed line) to be 94 fs. (b) Comparison of the time-dependent populations for the S$_2$ state of adenine obtained from TDDFTB (green) and from TDDFT (black).

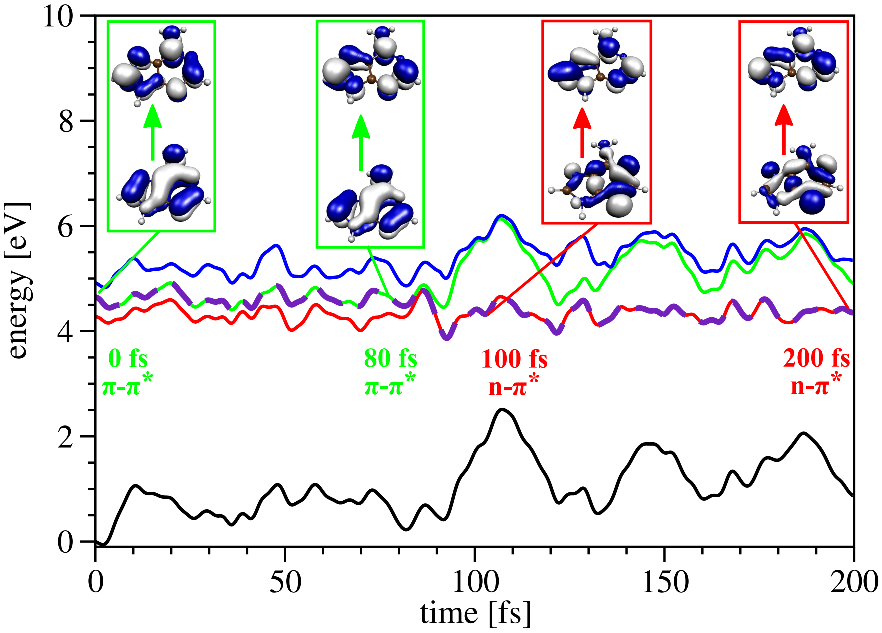

Figure 7.5: Time evolution of the ground state (black) and the three lowest excited states (red $S_1$, green $S_2$, and blue $S_3$) obtained from the nonadiabatic dynamics along one selected trajectory. The dashed violet line indicates the energy of the currently populated state during the dynamics. The character of the electronic state is indicated by the main orbitals involved in the transition.

population transfer into the ground electronic state occurs on a much larger timescale, which was estimated to be $\sim$ 11 ps. These results are in agreement with experimental findings, which predict a biexponential decay with a first component exhibiting a lifetime between 40 fs and 100 fs, followed by a second component on a much larger timescales of 1.2 - 9 ps (cf. e.g. References [75, 80, 246]).

In order to further investigate the quality of the TDDFTB nonadiabatic dynamics, simulations in the frame of TDDFT using the PBE functional and TZVP basis set have been performed for a small number of trajectories. The comparison of the time-dependent $S_2$ populations obtained from both methods shown in Figure 7.4(b) yields a good agreement, thus providing confidence for the use of TDDFTB for the simulations of nonadiabatic dynamics in adenine.

To provide a more detailed investigation of the ultrafast processes, the time evolution of one representative trajectory was analyzed. The time-dependent energies of the ground and three lowest excited states along this trajectory are presented in Figure 7.5. The character of the electronic state that was populated during the dynamics was analyzed in terms of the molecular orbitals mainly involved in the transitions. As evident from Figure 7.5, the character of the excited state changes from the initially excited $S_2$ $(\pi - \pi^*)$ to the $S_1$ $(\mathrm{n} - \pi^*)$ state at $t \sim 85$ fs. This is in agreement with the timescale of the average $S_2$ decay ($\tau \sim 100\,\mathrm{fs}$). These results confirm the two-step mechanism for the deactivation of gas-phase adenine: First, the initially excited $L_a$ state decays into the $n-\pi^*$ state. Second, population transfer into the ground state occurs providing efficient radiationless decay within a couple of ps. This mechanism is in agreement with the main decay channel identified in previous dynamics simulations[41,253,254] and with the interpretation of experimental TRPES measurements for pump pulse energies corresponding to the $L_a$ absorption maximum.[75,80,246]

## 7.5 Microsolvated Adenine

The simulations of the nonradiative relaxation of microsolvated adenine are based on previous work performed in the group of Prof. V. Bonačić-Koutecký.[63] They will be outlined in the following section in order to demonstrate the power of the TDDFTB nonadiabatic dynamics for the treatment of complex systems.

It is known from experimental work that adenine in water assumes the two tautomeric forms 9H-adenine and 7H-adenine,[256] which were also discussed for gas-phase adenine in Section 7.3. However, the simulations have been limited to 9H-adenine, since this tautomer is the dominant form in the gas phase[257] as well as in solution ($\sim 78\,\%$).[256] The structure of the 9H-adenine molecule in a solvation shell consisting of 26 water molecules was optimized with the B3LYP functional combined with the TZVP basis set. The most stable ground state structure is presented in Figure 7.6(a). The comparison of the absorption spectra for this structure calculated with B3LYP and TDDFTB, as shown in Figure 7.6(b) and (c), yields qualitative agreement, thus providing confidence for the use of TDDFTB in the nonadiabatic dynamics simulations. With both methods, the lowest intense transition indicated by a red arrow corresponds to the $L_a$ ($\pi - \pi^*$) transition in isolated adenine (cf. Fig. 7.2). The position of the $n-\pi^*$ transition in TDDFT is slightly different from the one in TDDFTB (for detailed analysis see Reference [63]). However, the relative position of the $n - \pi^*$ and $\pi - \pi^*$ states obtained from TDDFTB are analogous to those identified with the ab initio multi-reference perturbation configuration interaction method (CIPSI) combined with the PCM-IEF solvation model.[259]

For the investigation of the photodynamics of microsolvated adenine, an ensemble of 100 initial conditions was initially excited to the lowest intense state ($S_3$). The nonadiabatic dynamics was simulated using the TDDFTB method that has been developed in Chapter 2. Examination of the time-dependent populations presented in Figure 7.7 reveals the depopulation of the initially populated $S_3$ state mainly into the lower-lying $S_2$ and $S_1$ states with a time constant of 16 fs. A smaller fraction of trajectories also populates several other energetically close-lying states ($S_4$ - $S_7$), while there is no direct depopulation from $S_3$ into the ground state. Subsequently, the population transfer from the $S_2$ and $S_1$ states into the ground state ($S_0$) begins at $\sim 20\,\mathrm{fs}$ and is completed within $\sim 200\,\mathrm{fs}$. Thus, the nonradiative relaxation of microsolvated adenine occurs in a two-step process: In a first step, the initially excited $\pi-\pi^*$ state ($S_3$) is depopulated with a time constant of 16 fs, followed by a population transfer into the ground state on the timescale of $\sim 200\,\mathrm{fs}$. Comparison of the photodynamics of microsolvated adenine with isolated

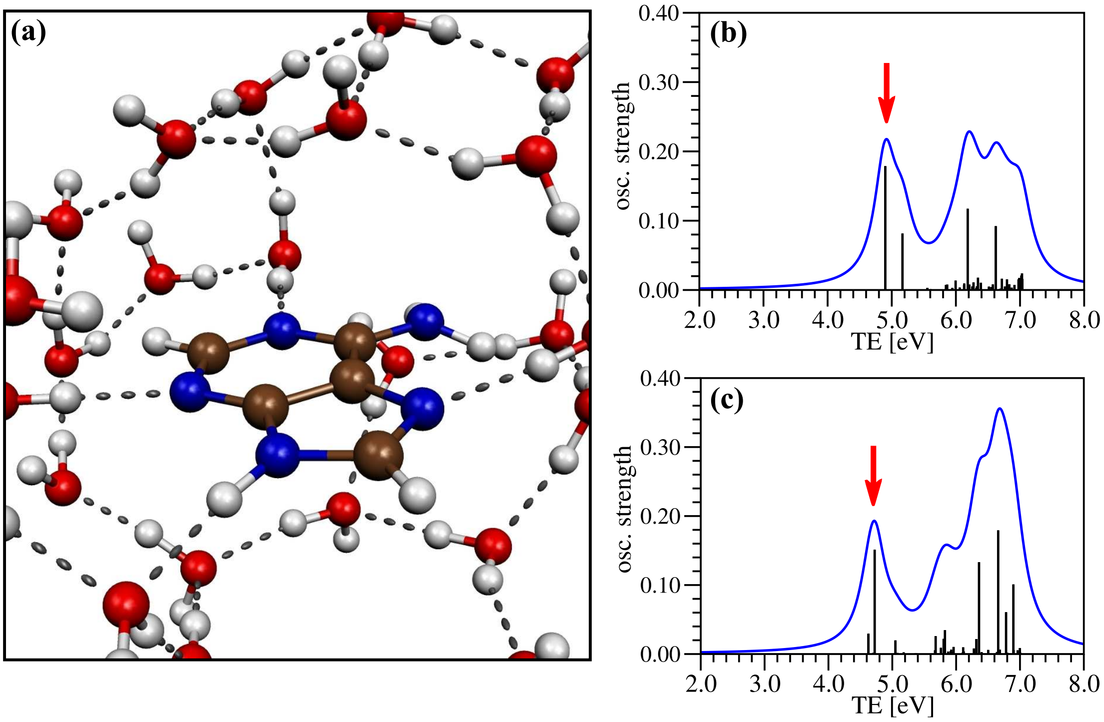

Figure 7.6: (a) Structure of microsolvated adenine, optimized with the B3LYP functional. (b)-(c) Comparison of the absorption spectra of microsolvated adenine obtained using (b) the B3LYP functional and (c) the TDDFTB method. The red arrow indicates the lowest intense transition.

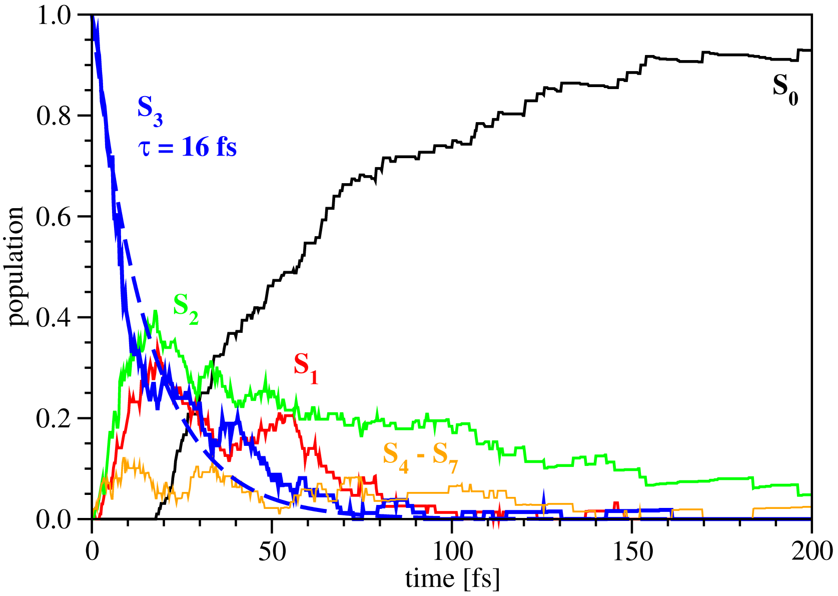

Figure 7.7: Time-dependent adiabatic populations of the ground state and the seven lowest excited states of microsolvated adenine initially excited to the S$_3$ state. The lifetime $\tau$ of the S$_3$ state was determined by exponential fit (blue dashed line) to be 16 fs.

adenine reveals qualitative similarities of the mechanisms for photorelaxation. However, the timescale for the transition to the electronic ground state in microsolvated adenine is significantly faster than in the gas phase (cf. Fig. 7.4 and 7.7). This is in agreement with the tendency toward the shortening of the lifetime identified in experiments on adenine in solution.[256] The faster timescales in microsolvated adenine can be interpreted in terms of the higher density of electronic states with respect to gas-phase adenine, which is described in detail in Reference [63]. The higher density of states increases the number of pathways that can lead to crossings with the ground state, thus provoking the shorter timescales for nonradiative relaxation.

## 7.6 Summary

In this chapter, the scope of the nonadiabatic dynamics based on the tight binding time-dependent density functional theory (TDDFTB) has been illustrated on the nonradiative relaxation of gas-phase and microsolvated adenine. As the simulations have revealed, both in gas-phase adenine and in adenine solvated by a first water shell nonradiative transition to the ground electronic state proceed in a two-step relaxation mechanism. This mechanism involves the ultrafast relaxation of the initially excited $\pi - \pi^*$ state, followed by decay into the ground state.[63] The mechanism is in agreement with previous theoretical results as well as with the interpretation of experimental TRPES spectra for gas-phase adenine.[41,75,80,246,253,254] The timescales for these nonradiative relaxation processes have been proven to be substantially shorter in microsolvated adenine with lifetimes of 16 fs for the $\pi - \pi^*$ state and $\sim 200$ fs for the return into the ground state ($\sim 100$ fs and $\sim 11$ ps, respectively, in isolated adenine).

The presented results show that the high computational efficiency of TDDFTB allows for the extension of the TDDFT-based nonadiabatic dynamics into the realm of complex molecular structures and nanostructures with an accuracy comparable to that of the TDDFT approach. It has been demonstrated that this approach represents a powerful tool for the examination of photoinduced ultrafast dynamics in complex systems such as biochromophores interacting with solvent or protein environment and polymers, which are currently beyond the scope of ab initio methods. The detailed understanding of the mechanisms for the nonradiative relaxation in these complex systems allows for the possibility of tuning their properties for future applications.

# Part III

# Summary

# 8 Summary and Outlook

The goal of this thesis was to develop a generally applicable theoretical framework for the simulation of ultrafast processes and observables in complex molecular systems. The TDDFT method was chosen as a basis for the description of the electronic structure, since it represents a good compromise between accuracy and computational efficiency. For this purpose, a new approach for the calculation of nonadiabatic couplings within TDDFT utilizing localized Gaussian atomic basis functions was formulated and implemented. This method was combined with Tully's surface hopping procedure for the treatment of nuclear dynamics based on classical trajectories. The method was advanced for the description of more complex systems such as chromophores in a solvation shell by employing the tight binding approximation to TDDFT.

Since the time-resolved photoelectron spectroscopy (TRPES) is a powerful experimental technique for real-time observation of ultrafast processes, a TDDFT based approach for the simulation of TRPES was developed. This method allows for the simulation of photoionization processes in complex systems, thus providing an interpretation of the experimental results. The basic idea of the method presented in this thesis is the approximate representation of the combined system of cation and photoelectron by excited states of the neutral species above the ionization threshold. This discrete approximation for the photoelectron spectrum can be calculated from TDDFT. For this purpose, a formulation of the transition dipole moments between excited states within TDDFT was developed. Simulations performed based on the Stieltjes imaging (SI) procedure provided the possibility to reconstruct photoelectron spectra from spectral moments. In this work, the spectral moments were calculated from the discrete TDDFT states. In principle, the approach can be extended to other methods. The convergence of the SI implementation was demonstrated by comparison of simulated photoelectron spectra with those obtained directly from TDDFT.

The scope of the developed theoretical methods for the simulation of complex systems was illustrated on several examples, which will be summarized in the following paragraphs:

**1. Photoisomerization in Benzylideneaniline (BAN):** The ultrafast trans-cis photoisomerization in BAN is particularly interesting, since BAN represents a basic structural unit for molecular switches. It was shown that both the cis and the trans isomer of BAN can be selectively excited, which is a basic requirement for reversible switching. The timescale for the deactivation of the trans isomer after optical excitation was determined as $\sim 180\,\mathrm{fs}$.[40] At the end of this process, the cis isomer of BAN is populated by 33 %. In the dynamics simulations, a semi-linear configuration for the C-C=N-C subunit of BAN was identified as a transition state for the photoinduced trans-cis isomerization.

This configuration is reached during the $S_1 \rightarrow S_0$ internal conversion (IC) and can lead to both formation of the cis isomer and back-isomerization to the trans isomer of BAN, thus providing an explanation for the low selectivity of the isomerization process. The isomer distribution may be manipulated by shaped laser pulses which can be obtained by utilizing the optimal control theory. This has already been achieved for a related smaller Schiff base[260] and can be utilized for controlling the switching process in the future. The simulated TRPES spectrum of BAN shows that the IC should be detectable experimentally. These theoretical findings already have stimulated the experimental investigation of the ultrafast photoisomerization in derivatives of BAN.[199]

**2. Ultrafast Photodynamics in Furan:** The theoretical investigation of the ultrafast photodynamics of furan reveals for the first time the mechanism of its nonradiative relaxation after excitation into the $\pi - \pi^*$ state.[85,86] According to this mechanism, the deactivation to the ground state takes place on a timescale of $\sim 140\,\text{fs}$. During this process, the Rydberg state, which exhibits a lower energy than the $\pi - \pi^*$ state in the equilibrium configuration, is not populated considerably. The simulated TRPES of furan agrees well with the experimental spectrum, thus allowing for the interpretation of the experimental findings. In contrast to earlier proposed mechanisms involving the $\pi - \sigma^*$ state, no evidence for the participation of this state in the photodynamics was found. According to the simulations, the diabatic $\pi - \pi^*$ character remains mainly preserved until the molecule returns to the ground state. These findings were confirmed by experimental time-resolved photoelectron angular distribution measurements, which did not indicate any change in the character of the excited electronic state.[85]

**3. Ultrafast Photodynamics in Pyrazine:** The ultrafast photoinduced dynamics in pyrazine involving the $S_2\,(\pi - \pi^*)$ and $S_1\,(n - \pi^*)$ states was investigated as a prototype example of ultrafast internal conversion through conical intersection. The $S_2$ state lifetime (21 fs) obtained from the TDDFT nonadiabatic dynamics simulations is in excellent agreement with the results from full quantum mechanical calculations as well as experimental values,[39] thus demonstrating the accuracy of the TDDFT nonadiabatic dynamics. The correspondence of the simulated TRPES, which takes into account the approximate ionization probabilities, with the experiment shows that the ionization probabilities are important for the accurate calculation of TRPES spectra.[84] A change in the ionization mechanism was identified in the simulations: The ionization of the initially populated $S_2$ excited state to the cationic first excited state turns over into ionization from the $S_1$ excited state to the cationic ground state after the $S_2 \rightarrow S_1$ internal conversion. The change in the ionization mechanism also provides an explanation for the absence of a systematic shift in the photoelectron kinetic energy, since the two channels exhibit similar ionization energies.

**4. Gas-Phase and Microsolvated Adenine:** The investigation of adenine in the gas phase and in the first solvation shell revealed a common two-step relaxation mechanism: In a rapid first step, internal conversion of the initially excited $\pi - \pi^*$ state into the $n - \pi^*$

state occurs. In a second step, the process is followed by a slower decay into the ground state.[63] These findings are in agreement with the mechanism identified in earlier theoretical and experimental investigations of gas-phase adenine.[41,75,80] Moreover, it was shown that the timescales for these processes of 16 fs and $\sim$ 200 fs for microsolvated adenine are substantially shorter than for gas-phase adenine, which exhibits $\sim$ 100 fs and $\sim$ 11 ps.[63] This tendency toward the shortening of the lifetime in solution compared to the gas phase is supported by experimental investigations.[256]

The above described examples demonstrate that the developed method for the nonadiabatic dynamics simulation based on TDDFT and TDDFTB is particularly suitable for the investigation and interpretation of ultrafast photoinduced processes in complex molecules. Future advancement of this approach is possible in several ways:

- Development of a TDDFT based method for the simulation of time-resolved photoelectron angular distributions.
- Implementation of this method in the frame of the QM/MM approach allowing for dynamical simulations of biomolecules in solution or in a protein environment.[261]
- Combination of the approach with the optimal control theory to manipulate photoinduced processes. This direction is already followed by the groups of Prof. V. Bonačić-Koutecký and Dr. R. Mitrić in the context of the field-induced surface hopping method.[260,262]

# 9 Zusammenfassung und Ausblick

Ziel dieser Arbeit war die Entwicklung einer breit anwendbaren Methode für die Simulation von ultraschnellen Prozessen und experimentellen Observablen. TDDFT wurde hierbei als Basis für die Berechnung der elektronischen Struktur gewählt, da die Methode einen guten Kompromiss zwischen Genauigkeit und rechnerischem Aufwand darstellt. Zu diesem Zweck wurde ein neuer Ansatz für die Beschreibung der nichtadiabatischen Kopplungen im Rahmen von TDDFT unter Verwendung lokalisierter Gauß-Basisfunktionen formuliert und implementiert. Die Methode wurde mit dem *Tully-Surface-Hopping*-Verfahren, mit welchem die Kerndynamik auf der Basis klassischer Trajektorien beschrieben wird, kombiniert. Darüber hinaus wurde eine Erweiterung der Simulationsmethode für die Beschreibung von noch komplexeren Systemen, wie etwa Chromophore in einer Solvatationshülle, im Rahmen der *Tight-Binding*-Näherung für TDDFT entwickelt.

Da die zeitaufgelöste Photoelektronenspektroskopie (TRPES) ein exzellentes experimentelles Verfahren für die Echtzeitbeobachtung von ultraschnellen Prozessen darstellt, wurde eine TDDFT-basierte Methode für die Simulation von TRPES entwickelt. Diese erlaubt die Simulation der Photoionisierungsprozesse von komplexen Systemen und ermöglicht dadurch die Interpretation experimenteller Ergebnisse. Der Methode liegt die Idee zu Grunde, das System aus Kation und Photoelektron durch angeregte Zustände des neutralen Moleküls oberhalb der Ionisierungsgrenze näherungsweise zu beschreiben. Diese diskrete Näherung für das Photoelektronenspektrum kann mit Hilfe der TDDFT berechnet werden. Dafür wurde eine Beschreibung für die Übergangsdipolmomente zwischen angeregten TDDFT-Zuständen entwickelt. Des Weiteren wurden Simulationen im Rahmen des *Stieltjes-Imaging* (SI)-Verfahrens, welches eine Möglichkeit der Rekonstruktion des Photoelektronenspektrums aus den spektralen Momenten bietet, durchgeführt. In dieser Arbeit wurden die spektralen Momente aus den diskreten TDDFT-Zuständen berechnet. Der Ansatz lässt sich im Prinzip jedoch auch auf andere Methoden übertragen. Die Konvergenz der Implementierung der SI-Prozedur konnte durch den Vergleich von simulierten Photoelektronenspektren mit direkt aus TDDFT berechneten Spektren gezeigt werden.

Die breite Anwendbarkeit der entwickelten theoretischen Methoden für die Simulation von komplexen Systemen wurde an mehreren ausgewählten Beispielen illustriert, welche im Folgenden kurz zusammengefasst sind:

**1. Photoisomerisierung in Benzylidenanilin (BAN):** Die ultraschnelle trans-cis-Photoisomerisierung in Benzylidenanilin ist besonders interessant, da BAN ein Grundbaustein für molekulare Schalter ist. Es konnte gezeigt werden, dass in BAN eine der Grundvoraussetzungen für reversibles Schalten, nämlich die selektive optische Anregbarkeit beider Isomere, gegeben ist. Die Zeitkonstante für die Deaktivierung des trans-Isomers nach der optischen Anregung wurde als $\sim$ 180 fs berechnet.[40] Am Ende dieses Prozesses liegt BAN zu einem Anteil von $\sim$ 33 % als cis-Isomer vor. In den Dynamiksimulationen wurde eine semilineare Konfiguration der C-C=N-C Untereinheit von BAN als Übergangszustand für die photochemische trans-cis-Isomerisierung identifiziert. Diese Konfiguration wird während der internen Konversion (*internal conversion*, IC) von $S_1$ zu $S_0$ erreicht und kann sowohl zur Bildung des cis-Isomers als auch zur Rückbildung des trans-Isomers von BAN führen, was eine mögliche Erklärung für die geringe Selektivität der Isomerisierung darstellt. Eine Möglichkeit zur gezielten Beeinflussung der Isomerenverteilung bietet die Anregung mit optimierten Laserpulsen, welche durch die Theorie der optimalen Kontrolle bestimmt werden können. Dies wurde bereits für eine verwandte kleinere Schiff-Base erreicht[260] und kann zukünftig für die Kontrolle des Schaltverhaltens angewendet werden. Das simulierte TRPES-Spektrum von BAN zeigt, dass dessen IC experimentell beobachtbar sein sollte. Diese theoretischen Ergebnisse haben bereits die experimentelle Erforschung der Photoisomerisierung von BAN-Derivaten angeregt.[199]

**2. Ultraschnelle Photodynamik in Furan:** Durch die theoretische Untersuchung der ultraschnellen Photodynamik in Furan konnte erstmalig der Mechanismus seiner nichtradiativen Relaxation nach der Anregung in den $\pi-\pi^*$-Zustand aufgeklärt werden.[85,86] Dem in dieser Arbeit vorgeschlagenen Mechanismus zufolge findet die Deaktivierung in den Grundzustand auf einer Zeitskala von $\sim$ 140 fs statt. Hierbei wird der in der Gleichgewichtskonfiguration energetisch tiefer liegende Rydberg-Zustand nicht merklich besetzt. Das simulierte TRPES-Spektrum von Furan stimmt weitgehend mit dem Experiment überein und erlaubt daher die Interpretation der experimentellen Ergebnisse. Im Gegensatz zu früher vorgeschlagenen Mechanismen, welche über den $\pi-\sigma^*$-Zustand verlaufen, wurde kein Hinweis auf dessen Beteiligung an der Photodynamik gefunden. Vielmehr bleibt der diabatische $\pi-\pi^*$-Charakter erhalten, bis der Übergang in den Grundzustand erfolgt. Diese Ergebnisse wurden durch die experimentellen Resultate der zeit- und winkelabhängigen Photoelektronenverteilung bestätigt, welche ebenfalls keinen Hinweis auf eine Charakteränderung des angeregten elektronischen Zustandes lieferten.[85]

**3. Ultraschnelle Photodynamik in Pyrazin:** Die ultraschnelle Photodynamik in Pyrazin, welche über den ursprünglich angeregten $S_2$ ($\pi-\pi^*$)-Zustand und den $S_1$ (n $-\pi^*$)-Zustand verläuft, wurde als Modellbeispiel für interne Konversionen über *Conical Intersections* untersucht. Dass die Lebensdauer des $S_2$-Zustandes (21 fs), die mit TDDFT-basierten nichtadiabatischen Dynamiksimulationen berechnet wurde, sowohl mit den Resultaten früherer voll-quantenmechanischer Berechnungen als auch mit den experimentell ermittelten Werten exzellente Übereinstimmung aufweist, belegt die Genauigkeit der nichtadiabatischen TDDFT-Dynamik.[39] Die Übereinstimmung des Experiments mit den TRPES-Simulationen, welche die Ionisierungswahrscheinlichkeiten berücksichtigen, zeigt, wie wichtig die Ionisierungswahrscheinlichkeiten für die akkurate Simulation von TRPES-Spektren sind.[84] In den Simulationen konnte ein Wechsel im Mechanismus für die Ionisierung ermittelt werden: Die anfängliche Ionisierung vom $S_2$ zum ersten angeregten kationischen Zustand geht über in die Ionisierung von $S_1$ in den kationischen Grundzustand, nachdem die $S_2 \rightarrow S_1$-IC stattgefunden hat. Dieser Wechsel im Mechanismus liefert auch die Erklärung für die Abwesenheit einer systematischen Verschiebung der Energie der Photoelektronen im TRPES-Spektrum, da beide Ionisierungsprozesse eine ähnliche Ionisierungsenergie aufweisen.

**4. Freies und mikrosolvatisiertes Adenin:** Die Untersuchungen von gasförmigem und mikrosolvatisiertem Adenin ergaben einen übereinstimmenden zweistufigen Relaxationsmechanismus: In einem ersten, schnelleren Schritt erfolgt die IC vom ursprünglich angeregten $\pi - \pi^*$-Zustand in einen $n - \pi^*$-Zustand. In einem zweiten Schritt findet der langsamere Übergang in den Grundzustand statt.[63] Diese Erkenntnisse stimmen mit dem Mechanismus überein, welcher in früheren theoretischen und experimentellen Untersuchungen von Adenin in der Gasphase identifiziert werden konnte.[41,75,80] Darüber hinaus konnte gezeigt werden, dass die IC-Zeitskalen in mikrosolvatisiertem Adenin mit 16 fs und $\sim$ 200 fs deutlich kürzer sind als für Adenin in der Gasphase mit $\sim$ 100 fs und $\sim$ 11 ps.[63] Die Tendenz zur Verkürzung der Lebensdauer von angeregtem Adenin in Lösung verglichen mit Adenin in der Gasphase wird durch experimentelle Ergebnisse bestätigt.[256]

Die dargestellten Beispiele zeigen, dass die entwickelte Simulationsmethode für die nichtadiabatische Dynamik im Rahmen von TDDFT bzw. TDDFTB hervorragend für die Untersuchung und Interpretation der ultraschnellen photoinduzierten Prozesse in komplexen Molekülen geeignet ist. Zukünftig wäre eine Weiterentwicklung dieses theoretischen Ansatzes in folgende Richtungen möglich:

- Entwicklung einer TDDFT-basierten Beschreibung der Photoionisierung für die Simulation der zeitabhängigen winkelaufgelösten Verteilungen der Photoelektronen.
- Implementierung im Rahmen des QM-/MM-Ansatzes, welcher beispielsweise dynamische Simulationen von großen Biomolekülen in Lösung oder in einer Proteinumgebung ermöglichen kann.[261]
- Kombination der Methode mit der Theorie der optimalen Kontrolle, um die gezielte Steuerung von photoinduzierten Prozessen zu ermöglichen. Diese Richtung wird in den Arbeitskreisen von Prof. V. Bonačić-Koutecký und von Dr. R. Mitrić im Rahmen der laserfeldinduzierten *Surface-Hopping*-Methode verfolgt.[260,262]

# Part IV

# Appendix

# Bibliography

[1] J. Michl and V. Bonačić-Koutecký. *Electronic Aspects of Organic Photochemistry.* John Wiley & Sons Inc., New York, 1990.

[2] W. Domcke, D. R. Yarkony, and Köppel H., editors. *Conical Intersections*, volume 15 of *Advanced Series in Physical Chemistry.* World Scientific, Singapore, 2004.

[3] F. Bernardi, M. Olivucci, and M. A. Robb. Potential energy surface crossings in organic photochemistry. *Chem. Soc. Rev.*, 25:321, 1996.

[4] M. A. Robb, M. Garavelli, M. Olivucci, and F. Bernardi. A computational strategy for organic photochemistry. *Rev. Comp. Chem.*, 15:87, 2000.

[5] M. Bixon and J. Jortner. Intramolecular Radiationless Transitions. *J. Chem. Phys.*, 48:715, 1968.

[6] A. H. Zewail. Femtochemistry: Atomic-Scale Dynamics of the Chemical Bond. *J. Phys. Chem. A*, 104:5660, 2000.

[7] M. Ben-Nun and T. J. Martinez. Photodynamics of ethylene: ab initio studies of conical intersections. *Chem. Phys.*, 259:237, 2000.

[8] D. R. Yarkony. Conical intersections: The new conventional wisdom. *J. Phys. Chem. A*, 105:6277, 2001.

[9] H. Lischka, M. Dallos, and R. Shepard. Analytic MRCI gradient for excited states: formalism and application to the n-$\pi^*$ valence- and n-(3s,3p) Rydberg states of formaldehyde. *Mol. Phys.*, 100:1647, 2002.

[10] M. Hartmann, J. Pittner, and V. Bonačić-Koutecký. Ab initio nonadiabatic dynamics involving conical intersection combined with Wigner distribution approach to ultrafast spectroscopy illustrated on $Na_3F_2$ cluster. *J. Chem. Phys.*, 114:2123, 2001.

[11] H. Lischka, M. Dallos, P. G. Szalay, D. R. Yarkony, and R. Shepard. Analytic evaluation of nonadiabatic coupling terms at the MR-CI level. I. Formalism. *J. Chem. Phys.*, 120:7322, 2004.

[12] M. Dantus, R. M. Bowman, M. Gruebele, and A. H. Zewail. Femtosecond Real-Time Probing of Reactions. V. The Reaction of IHgI. *J. Chem. Phys.*, 91:7437, 1989.

[13] A. Mokhtari, P. Cong, J. L. Herek, and A. H. Zewail. Direct Femtosecond Mapping of Trajectories in a Chemical-Reaction. *Nature*, 348:225, 1990.

[14] A. H. Zewail. Femtosecond Transition-State Dynamics. *Faraday Discuss.*, 91:207, 1991.

[15] J. Manz and L. Wöste, editors. *Femtosecond Chemistry Vol. 1 and 2.* VCH, Weinheim, 1995.

[16] I. V. Hertel and W. Radloff. Ultrafast dynamics in isolated molecules and molecular clusters. *Rep. Prog. Phys.*, 69:1897, 2006.

[17] R. Kienberger, E. Goulielmakis, M. Uiberacker, A. Baltuska, V. Yakovlev, F. Bammer, A. Scrinzi, T. Westerwalbesloh, U. Kleineberg, U. Heinzmann, M. Drescher, and F. Krausz. Atomic transient recorder. *Nature*, 427:817, 2004.

[18] A. L. Cavalieri, N. Müller, T. Uphues, V. S. Yakovlev, A. Baltuska, B. Horvath, B. Schmidt, L. Blumel, R. Holzwarth, S. Hendel, M. Drescher, U. Kleineberg, P. M. Echenique, R. Kienberger, F. Krausz, and U. Heinzmann. Attosecond spectroscopy in condensed matter. *Nature*, 449:1029, 2007.

[19] M. Uiberacker, T. Uphues, M. Schultze, A. J. Verhoef, V. Yakovlev, M. F. Kling, J. Rauschenberger, N. M. Kabachnik, H. Schröder, M. Lezius, K. L. Kompa, H.-G. Muller, M. J. J. Vrakking, S. Hendel, U. Kleineberg, U. Heinzmann, M. Drescher, and F. Krausz. Attosecond real-time observation of electron tunnelling in atoms. *Nature*, 446:627, 2007.

[20] F. Reiter, U. Graf, E. E. Serebryannikov, W. Schweinberger, M. Fiess, M. Schultze, A. M. Azzeer, R. Kienberger, F. Krausz, A. M. Zheltikov, and E. Goulielmakis. Route to Attosecond Nonlinear Spectroscopy. *Phys. Rev. Lett.*, 105:243902, 2010.

[21] R. Kosloff. Time-Dependent Quantum-Mechanical Methods for Molecular-Dynamics. *J. Phys. Chem.*, 92:2087, 1988.

[22] V. Engel, R. Schinke, and V. Staemmler. Photodissociation dynamics of $H_2O$ and $D_2O$ in the first absorption band: A complete ab initio treatment. *J. Chem. Phys.*, 88:129, 1988.

[23] V. Engel and H. Metiu. A Quantum-Mechanical Study of Predissociation Dynamics of NaI Excited by a Femtosecond Laser-Pulse. *J. Chem. Phys.*, 90:6116, 1989.

[24] T. Baumert, V. Engel, C. Meier, and G. Gerber. High Laser Field Effects in Multiphoton Ionization Of $Na_2$ – Experiment and Quantum Calculations. *Chem. Phys. Lett.*, 200:488, 1992.

[25] U. Manthe, H. D. Meyer, and L. S. Cederbaum. Wave-Packet Dynamics within the Multiconfiguration Hartree Framework – General-Aspects and Application to NOCl. *J. Chem. Phys.*, 97:3199, 1992.

[26] M. H. Beck, A. Jackle, G. A. Worth, and H. D. Meyer. The multiconfiguration time-dependent Hartree (MCTDH) method: a highly efficient algorithm for propagating wavepackets. *Phys. Rep.*, 324:1, 2000.

[27] R. Car and M. Parrinello. Unified Approach for Molecular Dynamics and Density-Functional Theory. *Phys. Rev. Lett.*, 55:2471, 1985.

[28] J. C. Tully and R. K. Preston. Trajectory Surface Hopping Approach to Nonadiabatic Molecular Collisions: The Reaction of $H^+$ with $D_2$. *J. Chem. Phys.*, 55:562, 1971.

[29] J. C. Tully. Molecular dynamics with electronic transitions. *J. Chem. Phys.*, 93: 1061, 1990.

[30] S. Hammes-Schiffer and J. C. Tully. Proton transfer in solution: Molecular dynamics with quantum transitions. *J. Chem. Phys.*, 101:4657, 1994.

[31] J. C. Tully. Mixed quantum-classical dynamics. *Faraday Discuss.*, 110:407, 1998.

[32] G. Granucci, M. Persico, and A. Toniolo. Direct semiclassical simulation of photochemical processes with semiempirical wave functions. *J. Chem. Phys.*, 114:10608, 2001.

[33] N. L. Doltsinis and D. Marx. Nonadiabatic Car-Parrinello Molecular Dynamics. *Phys. Rev. Lett.*, 88:166402, 2002.

[34] C. Ciminelli, G. Granucci, and M. Persico. The photoisomerization mechanism of azobenzene: A semiclassical simulation of nonadiabatic dynamics. *Chem. Eur. J.*, 10:2327, 2004.

[35] C. F. Craig, W. R. Duncan, and O. V. Prezhdo. Trajectory surface hopping in the time-dependent Kohn-Sham approach for electron-nuclear dynamics. *Phys. Rev. Lett.*, 95:163001, 2005.

[36] R. Mitrić, V. Bonačić-Koutecký, J. Pittner, and H. Lischka. Ab initio nonadiabatic dynamics study of ultrafast radiationless decay over conical intersections illustrated on the $Na_3F$ cluster. *J. Chem. Phys.*, 125:024303, 2006.

[37] M. Barbatti, G. Granucci, M. Persico, M. Ruckenbauer, M. Vazdar, M. Eckert-Maksić, and H. Lischka. The on-the-fly surface-hopping program system NEWTON-X: Application to ab initio simulation of the nonadiabatic photodynamics of benchmark systems. *J. Photochem. Photobiol., A*, 190:228, 2007.

[38] E. Tapavicza, I. Tavernelli, and U. Rothlisberger. Trajectory Surface Hopping within Linear Response Time-Dependent Density-Functional Theory. *Phys. Rev. Lett.*, 98:023001, 2007.

[39] U. Werner, R. Mitrić, T. Suzuki, and V. Bonačić-Koutecký. Nonadiabatic dynamics within the time dependent density functional theory: Ultrafast photodynamics in pyrazine. *Chem. Phys.*, 349:319, 2008.

[40] R. Mitrić, U. Werner, and V. Bonačić-Koutecký. Nonadiabatic dynamics and simulation of time resolved photoelectron spectra within time-dependent density functional theory: Ultrafast photoswitching in benzylideneaniline. *J. Chem. Phys.*, 129:164118, 2008.

[41] E. Fabiano and W. Thiel. Nonradiative Deexcitation Dynamics of 9H-Adenine: An OM2 Surface Hopping Study. *J. Phys. Chem. A*, 112:6859, 2008.

[42] E. Fabiano, T. W. Keal, and W. Thiel. Implementation of Surface Hopping Molecular Dynamics Using Semiempirical Methods. *Chem. Phys.*, 349:334, 2008.

[43] Z. Lan, E. Fabiano, and W. Thiel. Photoinduced Nonadiabatic Dynamics of Pyrimidine Nucleobases: On-the-Fly Surface-Hopping Study with Semiempirical Methods. *J. Phys. Chem. B*, 113:3548, 2009.

[44] J. R. Chelikowsky, L. Kronik, and I. Vasiliev. Time-dependent density-functional calculations for the optical spectra of molecules, clusters, and nanocrystals. *J. Phys.: Condens. Matter*, 15:R1517, 2003.

[45] K. Burke, J. Werschnik, and E. K. U. Gross. Time-dependent density functional theory: Past, present, and future. *J. Chem. Phys.*, 123:062206, 2005.

[46] H. Iikura, T. Tsuneda, T. Yanai, and K. Hirao. A long-range correction scheme for generalized-gradient-approximation exchange functionals. *J. Chem. Phys.*, 115: 3540, 2001.

[47] T. Yanai, D. P. Tew, and N. C Handy. A New Hybrid Exchange-Correlation Functional Using the Coulomb-Attenuating Method (CAM-B3LYP). *Chem. Phys. Lett.*, 393:51, 2004.

[48] S. Grimme. Accurate Description of van der Waals Complexes by Density Functional Theory Including Empirical Corrections. *J. Comp. Chem.*, 25:1463, 2004.

[49] A. Dreuw and M. Head-Gordon. Single-Reference ab Initio Methods for the Calculation of Excited States of Large Molecules. *Chem. Rev.*, 105:4009, 2005.

[50] A. D. Becke. Real-space post-Hartree-Fock correlation models. *J. Chem. Phys.*, 122:064101, 2005.

[51] S. Grimme. Semiempirical GGA-Type Density Functional Constructed with a Long-Range Dispersion Correction. *J. Comp. Chem.*, 27:1787, 2006.

[52] S. Kümmel and L. Kronik. Orbital-dependent density functionals: Theory and applications. *Rev. Mod. Phys.*, 80:3, 2008.

[53] R. Baer and D. Neuhauser. Density Functional Theory with Correct Long-Range Asymptotic Behavior. *Phys. Rev. Lett.*, 94:043002, 2005.

[54] J.-W. Song, S. Tokura, T. Sato, M. A. Watson, and K. Hirao. An Improved Long-range Corrected Hybrid Exchange-Correlation Functional Including a Short-range Gaussian Attenuation (LCgau-BOP). *J. Chem. Phys.*, 127:154109, 2007.

[55] T. Stein, L. Kronik, and R. Baer. Reliable Prediction of Charge Transfer Excitations in Molecular Complexes Using Time-Dependent Density Functional Theory. *J. Am. Chem. Soc.*, 131:2818, 2009.

[56] D. Porezag, T. Frauenheim, T. Köler, G. Seifert, and R. Kaschner. Construction of Tight-Binding-Like Potentials on the Basis of Density-Functional Theory - Application to Carbon. *Phys. Rev. B*, 51:12947, 1995.

[57] G. Seifert, D. Porezag, and T. Frauenheim. Calculations of molecules, clusters, and solids with a simplified LCAO-DFT-LDA scheme. *Int. J. Quantum Chem.*, 58:185, 1996.

[58] M. Elstner, D. Porezag, G. Jungnickel, J. Elsner, M. Haugk, T. Frauenheim, S. Suhai, and G. Seifert. Self-consistent-charge density-functional tight-binding method for simulations of complex materials properties. *Phys. Rev. B*, 58:7260, 1998.

[59] T. Frauenheim, G. Seifert, M. Elstner, T. A. Niehaus, C. Kohler, M. Amkreutz, M. Sternberg, Z. Hajnal, A. Di Carlo, and S. Suhai. Atomistic simulations of complex materials: ground-state and excited-state properties. *J. Phys.: Condens. Matter*, 14:3015, 2002.

[60] J. Fabian, L. A. Diaz, G. Seifert, and T. A. Niehaus. Calculation of excitation energies of organic chromophores: a critical evaluation. *J. Mol. Struc.-Theochem*, 594:41, 2002.

[61] T. Krüger, M. Elstner, P. Schiffels, and T. Frauenheim. Validation of the density-functional based tight-binding approximation method for the calculation of reaction energies and other data. *J. Chem. Phys.*, 122:114110, 2005.

[62] D. Heringer, T. A. Niehaus, M. Wanko, and T. Frauenheim. Analytical Excited State Forces for the Time-Dependent Density-Functional Tight-Binding Method. *J. Comput. Chem.*, 28:2589, 2007.

[63] R. Mitrić, U. Werner, M. Wohlgemuth, G. Seifert, and V. Bonačić-Koutecký. Nonadiabatic Dynamics within Time-Dependent Density Functional Tight Binding Method. *J. Phys. Chem. A*, 113:12700, 2009.

[64] K. Takatsuka, Y. Arasaki, K. H. Wang, and V. McKoy. Introductory lecture - Probing wavepacket dynamics with femtosecond energy- and angle-resolved photoelectron spectroscopy. *Faraday Discuss.*, 115:1, 2000.

[65] D. M. Neumark. Time-Resolved Photoelectron Spectroscopy of Molecules and Clusters. *Annu. Rev. Phys. Chem.*, 52:255, 2001.

[66] A. Stolow. Femtosecond Time-Resolved Photoelectron Spectroscopy of Polyatomic Molecules. *Annu. Rev. Phys. Chem.*, 54:89, 2003.

[67] A. Stolow, A. E. Bragg, and D. M. Neumark. Femtosecond Time-Resolved Photoelectron Spectroscopy. *Chem. Rev.*, 104:1719, 2004.

[68] T. Suzuki. Femtosecond Time-Resolved Photoelectron Imaging. *Annu. Rev. Phys. Chem.*, 57:555, 2006.

[69] A. Stolow and J. Underwood. Time-Resolved Photoelectron Spectroscopy of Nonadiabatic Dynamics in Polyatomic Molecules. *Adv. Chem. Phys.*, 139:497, 2008.

[70] D. W. Boo, Y. Ozaki, L. H. Andersen, and W. C. Lineberger. Femtosecond dynamics of linear $Ag_3$. *J. Phys. Chem. A*, 101:6688, 1997.

[71] N. Pontius, P. S. Bechthold, M. Neeb, and W. Eberhardt. Ultrafast hot-electron dynamics observed in $Pt_3{}^-$ using time-resolved photoelectron spectroscopy. *Phys. Rev. Lett.*, 84:1132, 2000.

[72] A. Sanov and W. C. Lineberger. Dynamics of cluster anions: a detailed look at condensed-phase interactions. *PhysChemComm*, 5:165, 2002.

[73] G. Lüttgens, N. Pontius, P. S. Bechthold, M. Neeb, and W. Eberhardt. Photon-induced Thermal Desorption of CO from Small Metal-Carbonyl Clusters. *Phys. Rev. Lett.*, 88:076102, 2002.

[74] T. Schultz, J. Quenneville, B. Levine, A. Toniolo, T. J. Martinez, S. Lochbrunner, M. Schmitt, J. P. Schaffer, M. Z. Zgierski, and A. Stolow. Mechanism and Dynamics of Azobenzene Photoisomerization. *J. Am. Chem. Soc.*, 125:8098, 2003.

[75] S. Ullrich, T. Schultz, M. Z. Zgierski, and A. Stolow. Direct Observation of Electronic Relaxation Dynamics in Adenine via Time-Resolved Photoelectron Spectroscopy. *J. Am. Chem. Soc.*, 126:2262, 2004.

[76] J. R. R. Verlet, A. E. Bragg, A. Kammrath, O. Cheshnovsky, and D. M. Neumark. Time-resolved relaxation dynamics of $Hg_n{}^-$ ($11 \leqq n \leqq 16$, n=18) clusters following intraband excitation at 1.5 eV. *J. Chem. Phys.*, 121:10015, 2004.

[77] A. E. Bragg, J. R. R. Verlet, A. Kammrath, O. Cheshnovsky, and D. M. Neumark. Time-resolved intraband electronic relaxation dynamics of $Hg_n{}^-$ clusters (n=7-13,15,18) excited at 1.0 eV. *J. Chem. Phys.*, 122:054314, 2005.

[78] D. H. Paik, J. S. Baskin, N. J. Kim, and A. H. Zewail. Ultrafast vectorial and scalar dynamics of ionic clusters: Azobenzene solvated by oxygen. *J. Chem. Phys.*, 125:133408, 2006.

[79] J. Stanzel, F. Burmeister, M. Neeb, W. Eberhardt, R. Mitrić, C. Bürgel, and V. Bonačić-Koutecký. Size-Dependent Dynamics in Excited States of Gold Clusters: From Oscillatory Motion to Photoinduced Melting. *J. Chem. Phys.*, 127: 164312, 2007.

[80] C. Z. Bisgaard, H. Satzger, S. Ullrich, and A. Stolow. Excited-State Dynamics of Isolated DNA Bases: A Case Study of Adenine. *ChemPhysChem*, 10:101, 2009.

[81] T. Horio, T. Fuji, Y.-I. Suzuki, and T. Suzuki. Probing Ultrafast Internal Conversion through Conical Intersection via Time-Energy Map of Photoelectron Angular Anisotropy. *J. Am. Chem. Soc.*, 113:10392, 2009.

[82] J. W. Ho, W. K. Chen, and P. Y. Cheng. Femtosecond pump-probe photoionization-photofragmentation spectroscopy: Photoionization-induced twisting and coherent vibrational motion of azobenzene cation. *J. Chem. Phys.*, 131:134308, 2009.

[83] Y.-I. Suzuki, T. Fuji, T. Horio, and T. Suzuki. Time-resolved photoelectron imaging of ultrafast $S_2$-$S_1$ internal conversion through conical intersection in pyrazine. *J. Chem. Phys.*, 132:174302, 2010.

[84] U. Werner, R. Mitrić, and V. Bonačić-Koutecký. Simulation of time resolved photoelectron spectra with Stieltjes imaging illustrated on ultrafast internal conversion in pyrazine. *J. Chem. Phys.*, 132:174301, 2010.

[85] T. Fuji, Y.-I. Suzuki, T. Horio, T. Suzuki, R. Mitrić, U. Werner, and V. Bonačić-Koutecký. Ultrafast photodynamics of furan. *J. Chem. Phys.*, 133:234303, 2010.

[86] R. Mitrić, J. Petersen, U. Werner, and V. Bonačić-Koutecký. Theoretical Methods for Nonadiabatic Dynamics "on the fly" in Complex Systems and its Control by Laser Fields. *Prog. Theor. Chem. Phys.*, in press, 2011.

[87] W. Kohn and L. J. Sham. Self-Consistent Equations Including Exchange and Correlation Effects. *Phys. Rev.*, 140:1133, 1965.

[88] A. D. Becke. Density-functional thermochemistry. III. The role of exact exchange. *J. Chem. Phys.*, 98:5648, 1993.

[89] J. Harris. Adiabatic-connection approach to Kohn-Sham theory. *Phys. Rev. A*, 29:1648, 1984.

[90] E. Runge and E. K. U. Gross. Density-Functional Theory for Time-Dependent Systems. *Phys. Rev. Lett.*, 52:997, 1984.

[91] M. E. Casida. *Recent Advances in Density Functional Methods, Part I*, chapter Time-Dependent Density Functional Response Theory for Molecules, page 155. World Scientific, Singapore, 1995.

[92] F. Cordova, L. J. Doriol, A. Ipatov, M. E. Casida, C. Filippi, and A. Vela. Troubleshooting time-dependent density-functional theory for photochemical applications: Oxirane. *J. Chem. Phys.*, 127:164111, 2007.

[93] E. Tapavicza, I. Tavernelli, U. Rothlisberger, C. Filippi, and M. E. Casida. Mixed Time-Dependent Density-Functional Theory/Classical Trajectory Surface Hopping Study of Oxirane Photochemistry. *J. Chem. Phys.*, 129:124108, 2008.

[94] M. van Faassen, P. L. de Boeij, R. van Leeuwen, J. A. Berger, and J. G. Snijders. Application of Time-Dependent Current-Density-Functional Theory to Nonlocal Exchange-Correlation Effects in Polymers. *J. Chem. Phys.*, 118:1044, 2003.

[95] M. J. G. Peach, P. Benfield, T. Helgaker, and D. J. Tozer. Excitation energies in density functional theory: An evaluation and a diagnostic test. *J. Chem. Phys.*, 128:044118, 2008.

[96] R. Ahlrichs, M. Bär, M. Häser, H. Horn, and C. Kölmel. Electronic-Structure Calculations On Workstation Computers – The Program System Turbomole. *Chem. Phys. Lett.*, 162:165, 1989.

[97] R. Gutierrez, M. Haugk, J. Elsner, G. Jungnickel, M. Elstner, A. Sieck, T. Frauenheim, and D. Porezag. Reconstructions of the Si-terminated (100) surface in beta-SiC: A theoretical study. *Phys. Rev. B*, 60:1771, 1999.

[98] M. Elstner, T. Frauenheim, E. Kaxiras, G. Seifert, and S. Suhai. A self-consistent charge density-functional based tight-binding scheme for large biomolecules. *Phys. Status Solidi B*, 217:357, 2000.

[99] E. Malolepsza, H. A. Witek, and K. Morokuma. Accurate vibrational frequencies using the self-consistent-charge density-functional tight-binding method. *Chem. Phys. Lett.*, 412:237, 2005.

[100] J. M. Knaup, B. Hourahine, and T. Frauenheim. Initial steps toward automating the fitting of DFTB E-rep(r). *J. Phys. Chem. A*, 111:5637, 2007.

[101] M. Elstner. SCC-DFTB: What is the proper degree of Self-Consistency? *J. Phys. Chem. A*, 111:5614, 2007.

[102] M. Elstner, P. Hobza, T. Frauenheim, S. Suhai, and E. Kaxiras. Hydrogen bonding and stacking interactions of nucleic acid base pairs: A density-functional-theory based treatment. *J. Chem. Phys.*, 114:5149, 2001.

[103] T. A. Niehaus, S. Suhai, F. D. Sala, P. Lugli, M. Elstner, G. Seifert, and T. Frauenheim. Tight-binding approach to time-dependent density-functional response theory. *Phys. Rev. B*, 63:085108, 2001.

[104] B. T. Sutcliffe. The Nuclear Motion Problem in Molecular Physics. *Adv. Quantum. Chem.*, 28:65, 1997.

[105] N. C. Blais and D. G. Truhlar. Trajectory-surface-hopping study of Na(3p $^2$P) +$H_2$ -> Na(3s $^2$S)+$H_2$(v',j',$\theta$). *J. Chem. Phys.*, 79:1334, 1983.

[106] J. R. Stine and J. T. Muckermann. More on the Multidimensional Surface Intersection Problem and Classical Trajectory Surface Hopping. *J. Chem. Phys.*, 84: 1056, 1986.

[107] G. Parlant and E. A. Gislason. An Exact Trajectory Surface Hopping Procedure – Comparison with Exact Quantal Calculations. *J. Chem. Phys.*, 91:4416, 1989.

[108] P. J. Kuntz. Classical path surface-hopping dynamics. I. General theory and illustrative trajectories. *J. Chem. Phys.*, 95:141, 1991.

[109] F. Webster, P. J. Rossky, and R. A. Friesner. Nonadiabatic Processes in Condensed Matter - Semiclassical Theory and Implementation. *Comput. Phys. Commun.*, 63: 494, 1991.

[110] I. H. Gersonde and H. Gabriel. Molecular-Dynamics of Photodissociation in Matrices Including Nonadiabatic Processes. *J. Chem. Phys.*, 98:2094, 1993.

[111] D. F. Coker and L. Xiao. Methods for Molecular-Dynamics with Nonadiabatic Transitions. *J. Chem. Phys.*, 102:496, 1995.

[112] A. I. Krylov, R. B. Gerber, and R. D. Coalson. Nonadiabatic dynamics and electronic energy relaxation of Cl($^2$P) atoms in solid Ar. *J. Chem. Phys.*, 105: 4626, 1996.

[113] P. V. Parandekar and J. C. Tully. Detailed Balance in Ehrenfest Mixed Quantum-Classical Dynamics. *J. Chem. Theory Comput.*, 2:229, 2006.

[114] H. Lischka, R. Shepard, R. M. Pitzer, I. Shavitt, M. Dallos, Th. Müller, P. G. Szalay, M. Seth, G. S. Kedziora, S. Yabushita, and Z. Zhang. High-level multireference methods in the quantum-chemistry program system COLUMBUS: Analytic MR-CISD and MR-AQCC gradients and MR-AQCC-LRT for excited states, GUGA spin-orbit CI and parallel CI density. *Phys. Chem. Chem. Phys.*, 3:664, 2001.

[115] M. F. Herman. Nonadiabatic semiclassical scattering. I. Analysis of generalized surface hopping procedures. *J. Chem. Phys.*, 81:754, 1984.

[116] D. Kohen, F. H. Stillinger, and J. C. Tully. Model studies of nonadiabatic dynamics. *J. Chem. Phys.*, 109:4713, 1998.

[117] S. Hammes-Schiffer. Mixed Quantum/Classical Dynamics of Hydrogen Transfer Reactions. *J. Phys. Chem. A*, 102:10443, 1998.

[118] U. Müller and G. Stock. Surface-hopping modeling of photoinduced relaxation dynamics on coupled potential-energy surfaces. *J. Chem. Phys.*, 107:6230, 1997.

[119] M. Ben-Nun, J. Quenneville, and T. J. Martinez. Ab Initio Multiple Spawning: Photochemistry from First Principles Quantum Molecular Dynamics. *J. Phys. Chem. A*, 104:5161, 2000.

[120] N. L. Doltsinis and D. Marx. First Principles Molecular Dynamics Involving Excited States and Nonadiabatic Transitions. *J. Theor. Comp. Chem.*, 1:319, 2002.

[121] N. L. Doltsinis and D. S. Kosov. Plane wave/pseudopotential implementation of excited state gradients in density functional linear response theory: A new route via implicit differentiation. *J. Chem. Phys.*, 122:144101, 2005.

[122] I. Tavernelli, E. Tapavicza, and U. Rothlisberger. Nonadiabatic Coupling Vectors Within Linear Response Time-Dependent Density Functional Theory. *J. Chem. Phys.*, 130:124107, 2009.

[123] R. Baer. Non-adiabatic couplings by time-dependent density functional theory. *Chem. Phys. Lett.*, 364:75, 2002.

[124] S. R. Billeter and A. Curioni. Calculation of nonadiabatic couplings in density-functional theory. *J. Chem. Phys.*, 122:034105, 2005.

[125] C. P. Hu, H. Hirai, and O. Sugino. Nonadiabatic couplings from time-dependent density functional theory: Formulation in the Casida formalism and practical scheme within modified linear response. *J. Chem. Phys.*, 127:064103, 2007.

[126] K. Yabana, T. Nakatsukasa, J. I. Iwata, and G. F. Bertsch. Real-time, real-space implementation of the linear response time-dependent density-functional theory. *Phys. Status Solidi B*, 243:1121, 2006.

[127] E. P. Wigner. On the quantum correction for thermodynamic equilibrium. *Phys. Rev.*, 40:0749, 1932.

[128] M. Hillery, R. F. O'Connel, M. O. Scully, and E. P. Wigner. Distribution-Functions in Physics: Fundamentals. *Phys. Rep.*, 106:121, 1984.

[129] Z. M. Li, J. Y. Fang, and C. C. Martens. Simulation of ultrafast dynamics and pump-probe spectroscopy using classical trajectories. *J. Chem. Phys.*, 104:6919, 1996.

[130] M. Hartmann, J. Pittner, V. Bonačić-Koutecký, A. Heidenreich, and J. Jortner. Theoretical exploration of femtosecond multi-state nuclear dynamics of small clusters. *J. Chem. Phys.*, 108:3096, 1998.

[131] M. Hartmann, J. Pittner, V. Bonačić-Koutecký, A. Heidenreich, and J. Jortner. Ultrafast dynamics of small clusters on the time scale of nuclear motion. *J. Phys. Chem. A*, 102:4069, 1998.

[132] M. Hartmann, J. Pittner, and V. Bonačić-Koutecký. Ab initio adiabatic dynamics involving excited states combined with Wigner distribution approach to ultrafast spectroscopy illustrated on alkali halide clusters. *J. Chem. Phys.*, 114:2106, 2001.

[133] V. Bonačić-Koutecký and R. Mitrić. Theoretical Exploration of Ultrafast Dynamics in Atomic Clusters: Analysis and Control. *Chem. Rev.*, 105:11, 2005.

[134] L. Verlet. Computer Experiments on Classical Fluids. I. Thermodynamical Properties of Lennard-Jones Molecules. *Phys. Rev.*, 159:98, 1967.

[135] V. Bonačić-Koutecký, K. Schöffel, and J. Michl. Critically Heterosymmetric Biradicaloid Geometries of Protonated Schiff-Bases – Possible Consequences for Photochemistry and Photobiology. *Theor. Chim. Acta*, 72:459, 1987.

[136] M. Barbatti, J. Pittner, M. Pederzoli, U. Werner, R. Mitrić, V. Bonačić-Koutecký, and H. Lischka. Non-adiabatic dynamics of pyrrole: Dependence of deactivation mechanisms on the excitation energy. *Chem. Phys.*, 375:26, 2010.

[137] T. S. Rose, M. J. Rosker, and A. Zewail. Femtosecond Real-Time Observation Of Wave Packet Oscillations (Resonance) in Dissociation Reactions. *J. Chem. Phys.*, 88:6672, 1988.

[138] J. H. D. Eland. *Photoelectron Spectroscopy, 2nd edition.* Butterworths, London, 1984.

[139] V. Blanchet, M. Z. Zgierski, T. Seideman, and A. Stolow. Discerning vibronic molecular dynamics using time-resolved photoelectron spectroscopy. *Nature*, 401: 52, 1999.

[140] R. Haight, J. Bokor, J. Stark, R. H. Storz, R. R. Freeman, and P. H. Bucksbaum. Picosecond Time-Resolved Photoemission Study of the InP(110) Surface. *Phys. Rev. Lett.*, 54:1302, 1985.

[141] C. Meier and V. Engel. Electron kinetic energy distributions from multiphoton ionization of $Na_2$ with femtosecond laser pulses. *Chem. Phys. Lett.*, 212:691, 1993.

[142] M. Seel and W. Domcke. Femtosecond time-resolved ionization spectroscopy of ultrafast internal-conversion dynamics in polyatomic molecules: Theory and computational studies. *J. Chem. Phys.*, 95:7806, 1991.

[143] M. Braun, C. Meier, and V. Engel. Approximative Calculation of Short-Pulse Pump-Probe Ionization Signals. *J. Chem. Phys.*, 103:7907, 1995.

[144] S. Dilthey, S. Hahn, and G. Stock. Approximate Calculation of Femtosecond Pump-Probe Spectra Monitoring Nonadiabatic Excited-State Dynamics. *J. Chem. Phys.*, 112:4910, 2000.

[145] Y. Arasaki, K. Takatsuka, K. H. Wang, and V. McKoy. Femtosecond Energy- and Angle-Resolved Photoelectron Spectroscopy. *J. Chem. Phys.*, 112:8871, 2000.

[146] S. Hahn and G. Stock. Efficient calculation of femtosecond time-resolved photoelectron spectra : method and application to the ionization of pyrazine. *Phys. Chem. Chem. Phys.*, 3:2331, 2001.

[147] Y. Suzuki, M. Stener, and T. Seideman. Multidimensional calculation of time-resolved photoelectron angular distributions: The internal conversion dynamics of pyrazine. *J. Chem. Phys.*, 118:4432, 2003.

[148] H. R. Hudock, B. G. Levine, A. L. Thompson, H. Satzger, D. Tonwnsend, N. Gador, S. Ullrich, A. Stolow, and T. J. Martinez. Ab initio molecular dynamics and time-resolved photoelectron spectroscopy of electronically excited uracil and thymine. *J. Phys. Chem. A*, 111:8500, 2007.

[149] H. R. Hudock and T. J. Martinez. Excited-State Dynamics of Cytosine Reveal Multiple Intrinsic Subpicosecond Pathways. *Chem. Phys. Chem.*, 9:2486, 2008.

[150] Y. Arasaki and K. Takatsuka. Quantum Wavepacket Dynamics for Time-Resolved Photoelectron Spectroscopy of the NO_2 Conical Intersection. *Chem. Phys.*, 338: 175, 2007.

[151] M. T. D. Varella, Y. Arasaki, H. Ushiyama, K. Takatsuka, K. S. Wang, and V. McKoy. Real-time Observation of Intramolecular Proton Transfer in the Electronic Ground State of Chloromalonaldehyde: An Ab Initio Study of Time-Resolved Photoelectron Spectra. *J. Chem. Phys.*, 126:054303, 2007.

[152] R. Mitrić, J. Petersen, M. Wohlgemuth, U. Werner, V. Bonačić-Koutecký, L. Wöste, and J. Jortner. Time-Resolved Femtosecond Photoelectron Spectroscopy by Field-Induced Surface Hopping. *J. Phys. Chem. A*, 115:3755, 2011.

[153] C. M. Oana and A. I. Krylov. Dyson orbitals for ionization from the ground and electronically excited states within equation-of-motion coupled-cluster formalism: Theory, implementation, and examples. *J. Chem. Phys.*, 127:234106, 2007.

[154] I. Cacelli, V. Carravetta, A. Rizzo, and R. Moccia. The Calculation of Photoionization Cross-Sections of Simple Polyatomic-Molecules by $L^2$ Methods. *Phys. Rep.*, 205:283, 1991.

[155] A. Szabo and N. Ostlund. *Modern Quantum Chemistry.* McGraw-Hill, New York, 1989.

[156] D. L. Yeager, M. A. C. Nascimento, and V. McKoy. Some Applications of Excited-State Excited-State Transition Densities. *Phys. Rev. A*, 11:1168, 1975.

[157] P. W. Langhoff. Stieltjes Imaging of Atomic and Molecular Photoabsorption Profiles. *Chem. Phys. Lett.*, 22:60, 1973.

[158] P. W. Langhoff and C. T. Corcoran. Stieltjes Imaging of Photoabsorption and Dispersion Profiles. *J. Chem. Phys.*, 61:146, 1974.

[159] K. Gokhberg, V. Vysotskiy, L. S. Cederbaum, L. Storchi, F. Tarantelli, and V. Averbukh. Molecular photoionization cross sections by Stieltjes-Chebyshev moment theory applied to Lanczos pseudospectra. *J. Chem. Phys*, 130:064104, 2009.

[160] H. A. Kramers and V. Heisenberg. Über die Streuung von Strahlung durch Atome. *ZS. f. Phys.*, 31:681, 1925.

[161] P. A. M. Dirac. The Quantum Theory of the Emission and Absorption of Radiation. *Proc. R. Soc. Lond. A*, 114:243, 1927.

[162] P. A. M. Dirac. The Quantum Theory of Dispersion. *Proc. R. Soc. Lond. A*, 114: 710, 1927.

[163] J. A. Shohat and J. D. Tamarkin. *The problem of moments. Mathematical Surveys, Vol. 1.* American Mathematical Society, New York, 1943.

[164] J. C. Wheeler and R. G. Gordon. *The Pade Approximant in Theoretical Physics*, pages 99–128. Academic, New York, 1970.

[165] P. W. Langhoff, C. T. Corcoran, J. S. Sims, F. Weinhold, and R. M. Glover. Moment-Theory Investigations of Photoabsorption and Dispersion Profiles in Atoms and Ions. *Phys. Rev. A*, 14:1042, 1976.

[166] B. H. Armstrong. Empirical Analysis of $H^-$ Photodetachment Cross Section. *Phys. Rev.*, 131:1132, 1963.

[167] M. Inokuti and Y. K. Kim. Total Cross Sections for Inelastic Scattering of Charged Particles by Atoms and Molecules. II. Negative Hydrogen Ion. *Phys. Rev.*, 173: 154, 1968.

[168] R. Feng, G. Cooper, and C. E. Brion. Dipole (e,e) spectroscopic studies of benzene: quantitative photoabsorption in the UV, VUV and soft X-ray regions. *J. Electron Spectrosc. Relat. Phenom.*, 123:199, 2002.

[169] A. D. Becke. Density-functional thermochemistry. V. Systematic optimization of exchange-correlation functionals. *J. Chem. Phys.*, 107:8554, 1997.

[170] R. Henderson, J. M. Baldwind, T. A. Ceska, F. Zemline, E. Beckmann, and K. H. Downing. Model for the Structure of Bacteriorhodopsin Based on High-resolution Electron Cryomicroscopy. *J. Mol. Biol.*, 213:899, 1990.

[171] A. K. Singh and N. Majumder. Bathochromicity of Retinal Schiff-bases In Cellulose Matrix. *Photochem. Photobiol.*, 60:510, 1994.

[172] I. Conti and M. Garavelli. Substituent-Controlled Photoisomerization in Retinal Chromophore Models: Fluorinated and Methoxy-Cubstituted Protonated Schiff bases. *J. Photochem. Photobiol. A*, 190:258, 2007.

[173] M. A. Elsayer. On the Molecular Mechanisms of the Solar To Electric Energy-Conversion By the Other Photosynthetic System In Nature, Bacteriorhodopsin. *Acc. Chem. Res.*, 25:279, 1992.

[174] A. Padwa. Photochemistry of Carbon-Nitrogen Double-Bond. *Chem. Rev.*, 77:37, 1977.

[175] P. Brocklehurst. Ultra-Violet Spectra of Azomethines and Related Compounds. *Tetrahedron*, 18:299, 1962.

[176] H. B. Burgi and J. D. Dunitz. Crystal and Molecular Structures of Benzylideneaniline, Benzylideneaniline Para Carboxylic Acid and Para Methylbenzylidene Para Nitroaniline. *Helv. Chim. Acta.*, 53:1747, 1970.

[177] M. A. El-Bayoumi, M. El-Aasser, and F. Abdel-Halim. Electronic spectra and structures of Schiff's bases. I. Benzanils. *J. Am. Chem. Soc.*, 93:586, 1971.

[178] M. Traetteberg, I. Hilmo, R. J. Abraham, and S. Ljunggren. Molecular-Structure Of N-Benzylidene-Aniline. *J. Mol. Struc.*, 48:395, 1978.

[179] J. Bernstein, Y. M. Engel, and A. T. Hagler. An ab initio study of the conformational energetics of N-benzylideneaniline. *J. Chem. Phys.*, 75:2346, 1981.

[180] L. N. Patnaik and S. Das. Conformation of Para-dimethylaminobenzylidene-para-nitroaniline, Para-nitrobenzylidene-para-dimethylaminoaniline, their Stilbene and Azobenzene Derivatives. *Int. J. Quant. Chem.*, 27:135, 1985.

[181] H. Rau and E. Lüddecke. On the Rotation-Inversion Controversy on Photo-Isomerization of Azobenzenes – Experimental Proof of Inversion. *J. Am. Chem. Soc.*, 104:1616, 1982.

[182] D. H. Waldeck. Photoisomerization Dynamics of Stilbenes. *Chem. Rev.*, 91:415, 1991.

[183] T. Arai and K. Tokumaru. Photochemical One-Way Adiabatic Isomerization of Aromatic Olefins. *Chem. Rev.*, 93:23, 1993.

[184] N. Tamai and H. Miyasaka. Ultrafast dynamics of photochromic systems. *Chem. Rev.*, 100:1875, 2000.

[185] A. Toniolo, C. Ciminelli, M. Persico, and T. J. Martinez. Simulation of the photodynamics of azobenzene on its first excited state: Comparison of full multiple spawning and surface hopping treatments. *J. Chem. Phys.*, 123:234308, 2005.

[186] G. Granucci and M. Persico. Critical appraisal of the fewest switches algorithm for surface hopping. *J. Chem. Phys.*, 126:134114, 2007.

[187] M. J. Comstock, N. Levy, A. Kirakosian, J. W. Cho, F. Lauterwasser, J. H. Harvey, D. A. Strubbe, J. M. J. Frechet, D. Trauner, S. G. Louie, and M. F. Crommie. Reversible Photomechanical Switching of Individual Engineered Molecules at a Metallic Surface. *Phys. Rev. Lett.*, 99:038301, 2007.

[188] I. Conti, M. Garavelli, and G. Orlandi. The different photoisomerization efficiency of azobenzene in the lowest n$\pi$* and $\pi\pi$* singlets: The role of a phantom state. *J. Am. Chem. Soc.*, 130:5216, 2008.

[189] J. P. Perdew, K. Burke, and M. Ernzerhof. Generalized Gradient Approximation Made Simple. *Phys. Rev. Lett.*, 77:3865, 1996.

[190] A. Schäfer, C. Huber, and R. Ahlrichs. Fully Optimized Contracted Gaussian-Basis Sets of Triple Zeta Valence Quality for Atoms Li to Kr. *J. Chem. Phys.*, 100:5829, 1994.

[191] B. I. Dunlap, J. W. D. Connolly, and J. R. Sabin. Some Approximations in Applications of X-Alpha Theory. *J. Chem. Phys.*, 71:3396, 1979.

[192] K. Eichkorn, O. Treutler, H. Öhm, M. Häser, and R. Ahlrichs. Auxiliary Basis-Sets To Approximate Coulomb Potentials. *Chem. Phys. Lett.*, 240:283, 1995.

[193] H. H. Jaffe, S. J. Yeh, and R. W. Gardner. The Electronic Spectra Of Azobenzene Derivatives And Their Conjugate Acids. *J. Mol. Spectrosc.*, 2:120, 1958.

[194] E. Haselbach and E. Heilbronner. Electron Structure And Physical-Chemical Properties Of Azo Compounds. XIV. Conformation of Benzalaniline. *Helv. Chim. Acta*, 51:16, 1968.

[195] T. Bally, E. Haselbach, S. Lanyiova, F. Marschner, and M. Rossi. Concerning Conformation of Isolated Benzylideneaniline. *Helv. Chim. Acta*, 59:486, 1976.

[196] J. O. Morley. Theoretical-Studies on the Structure and Electronic-Properties of 3-(4-Tolyl)Sydnone. *J. Chem. Soc. Perkin Trans. 2*, 4:253, 1995.

[197] P. Bao and Z. H. Yu. Theoretical studies on the role of $\pi$-electron delocalization in determining the conformation of N-benzylideneaniline with three types of LMO basis sets. *J. Comput. Chem.*, 27:809, 2006.

[198] A. V. Gaenko, A. Devarajan, L. Gagliardi, R. Lindh, and G. Orlandi. Ab initio DFT study of Z-E isomerization pathways of N-benzylideneaniline. *Theo. Chem. Acc.*, 118:271, 2007.

[199] L. Óvári, Y. Luo, F. Leyssner, R. Haag, M. Wolf, and P. Tegeder. Adsorption and switching properties of a N-benzylideneaniline based molecular switch on a Au(111) surface. *J. Chem. Phys.*, 133:044707, 2010.

[200] L. Serrano-Andrés, M. Merchán, I. Nebot-Gil, B. O. Roos, and M. Fülscher. Theoretical Study of the Electronic Spectra of Cyclopentadiene, Pyrrole, and Furan. *J. Am. Chem. Soc.*, 115:6184, 1993.

[201] S. Wilsey, M. J. Bearpark, F. Bernardi, M. Olivucci, and M. A. Robb. The Role of Degenerate Biradicals in the Photorearrangement of Acylcyclopropenes to Furans. *J. Am. Chem. Soc.*, 118:4469, 1996.

[202] M. D'Auria. Ab Initio Study on the Photochemical Isomerization of Furan Derivatives. *J. Org. Chem.*, 65:2494, 2000.

[203] D. M. P. Holland, L. Karlsson, and W. von Niessen. The identification of the outer valence shell p-photoelectron bands in furan, pyrrole and thiophene. *J. Electron Spectrosc. Relat. Phenom.*, 113:221, 2001.

[204] R. Burcl, R. D. Amos, and N. C. Handy. Study of excited states of furan and pyrrole by time-dependent density functional theory. *Chem. Phys. Lett.*, 355:8, 2002.

[205] E. V. Gromov, A. B. Trofimov, N. M. Vitkovskaya, J. Schirmer, and H. Köppel. Theoretical study of the low-lying excited singlet states of furan. *J. Chem. Phys.*, 119:737, 2003.

[206] E. V. Gromov, A. B. Trofimov, N. M. Vitkovskaya, H. Köppel, J. Schirmer, H. D. Meyer, and L. S. Cederbaum. Theoretical study of excitations in furan: Spectra and molecular dynamics. *J. Chem. Phys.*, 121:4585, 2004.

[207] H. Köppel, E. V. Gromov, and A. B. Trofimov. Multi-mode-multi-state quantum dynamics of key five-membered heterocycles: spectroscopy and ultrafast internal conversion. *Chem. Phys.*, 304:35, 2004.

[208] J. Yang, J. Li, and Y. Mo. The vibrational structures of furan, pyrrole, and thiophene cations studied by zero kinetic energy photoelectron spectroscopy. *J. Chem. Phys.*, 125:174313, 2006.

[209] N. Gavrilov, S. Salzmann, and C. M. Marian. Deactivation via ring opening: A quantum chemical study of the excited states of furan and comparison to thiophene. *Chem. Phys.*, 349:269, 2008.

[210] E. V. Gromov, A. B. Trofimov, F. Gatti, and H. Köppel. Theoretical study of photoinduced ring-opening in furan. *J. Chem. Phys.*, 133:164309, 2010.

[211] A. B. Trofimov, I. L. Zaitseva, T. E. Moskovskaya, and N. M. Vitkovskaya. Theoretical investigation of photoelectron spectra of furan, pyrrole, thiophene, and selenole. *Chem. Heterocycl. Compd.*, 44:1101, 2008.

[212] R. Weinkauf, L. Lehr, E. W. Schlag, S. Salzmann, and C. M. Marian. Ultrafast dynamics in thiophene investigated by femtosecond pump probe photoelectron spectroscopy and theory. *Phys. Chem. Chem. Phys.*, 10:393, 2008.

[213] J. L. Roebber, D. P. Gerrity, H. R. Hemley, and V. Vaida. Electronic spectrum of furan from 2200 to 1950 Å. *Chem. Phys. Lett.*, 75:104, 1980.

[214] M. Palmer, I. Walker, C. Ballard, and M. Guest. The electronic states of furan studied by VUV absorption, near-threshold electron energy-loss spectroscopy and ab initio multi-reference configuration interaction calculations. *Chem. Phys.*, 192: 111, 1995.

[215] C. Adamo and V. Barone. Toward reliable density functional methods without adjustable parameters: The PBE0 model. *J. Chem. Phys.*, 110:6158, 1999.

[216] R. Krishnan, J. S. Binkley, R. Seeger, and J. A. Pople. Self-Consistent Molecular-Orbital Methods. XX. Basis Set for Correlated Wave-Functions. *J. Chem. Phys.*, 72:650, 1980.

[217] T. Fuji, T. Horio and T. Suzuki. Generation of sub-two-cycle mid-infrared pulses by four-wave mixing through filamentation in air. *Opt. Lett.*, 32:2481, 2007.

[218] T. Fuji, T. Suzuki, E. E. Serebryannikov, and A. Zheltikov. Experimental and theoretical investigation of a multicolor filament. *Phys. Rev. A*, 80:063822, 2009.

[219] G. A. Garcia, L. Nahon, and I. Powis. Two-dimensional charged particle image inversion using a polar basis function expansion. *Rev. Sci. Instrum.*, 75:4989, 2004.

[220] E. E. Rennie, L. Cooper, C. A. F. Johnson, J. E. Parker, R. A. Mackie, L. G. Shpinkova, D. M. P. Holland, D. A. Shaw, and M. A. Hayes. A study of the unimolecular decomposition of internal-energyselected furan molecular ions by threshold-photoelectron-photoion coincidence spectroscopy. *Chem. Phys.*, 263:149, 2001.

[221] P. Derrick, L. Asbrink, O. Edqvist, and E. Lindholm. Photoelectron-Spectroscopical Study of Vibrations of Furan, Thiophene, Pyrrole and Cyclopentadiene. *Spectrochim. Acta*, A 27:2525, 1971.

[222] M. Tsubouchi and T. Suzuki. Femtosecond photoelectron imaging on pyridine: Ultrafast electronic dephasing from the $S_1(n\pi^*)$ state and Rydberg state energetics. *J. Phys. Chem. A*, 107:10897, 2003.

[223] R. Schneider and W. Domcke. $S_1$-$S_2$ Conical intersection and ultrafast $S_2$-$S_1$ Internal conversion in pyrazine. *Chem. Phys. Lett.*, 150:235, 1988.

[224] R. Schneider, W. Domcke, and H. Köppel. Aspects of dissipative electronic and vibrational dynamics of strongly vibronically coupled systems. *J. Chem. Phys.*, 92:1045, 1990.

[225] L. Seidner, G. Stock, A. L. Sobolewski, and W. Domcke. Ab initio characterization of the $S_1$-$S_2$ conical intersection in pyrazine and calculation of spectra. *J. Chem. Phys.*, 96:5298, 1992.

[226] G. Stock and W. Domcke. Femtosecond spectroscopy of ultrafast nonadiabatic excited-state dynamics on the basis of ab initio potential-energy surfaces: the $S_2$ state of pyrazine. *J. Phys. Chem.*, 97:12466, 1993.

[227] C. Woywod, W. Domcke, A. L. Sobolewski, and H.-J. Werner. Characterization of the $S_1$-$S_2$ conical intersection in pyrazine using ab initio multiconfiguration self-consistent-field and multireference configuration-interaction methods. *J. Chem. Phys.*, 100:1400, 1994.

[228] S. Krempl, M. Winterstetter, H. Plöhn, and W. Domcke. Path-integral treatment of multi-mode vibronic coupling. *J. Chem. Phys.*, 100:926, 1994.

[229] G. A. Worth, H.-D. Meyer, and L. S. Cederbaum. The effect of a model environment on the $S_2$ absorption spectrum of pyrazine: A wave packet study treating all 24 vibrational modes. *J. Chem. Phys.*, 105:4412, 1996.

[230] G. A. Worth, H.-D. Meyer, and L. S. Cederbaum. Relaxation of a system with a conical intersection coupled to a bath: A benchmark 24-dimensional wave packet study treating the environment explicitly. *J. Chem. Phys.*, 109:3518, 1998.

[231] A. Raab, G. A. Worth, H.-D. Meyer, and L. S. Cederbaum. Molecular dynamics of pyrazine after excitation to the $S_2$ electronic state using a realistic 24-mode model Hamiltonian. *J. Chem. Phys.*, 110:936, 1999.

[232] V. Stert, P. Farmanara, and W. Radloff. Electron configuration changes in excited pyrazine molecules analyzed by femtosecond time-resolved photoelectron spectroscopy. *J. Chem. Phys.*, 112:4460, 2000.

[233] C. Coletti and G. D. Billing. Quantum Dressed Classical Mechanics: Application to the Photo-Absorption of Pyrazine. *Chem. Phys. Lett.*, 368:289, 2003.

[234] P. Puzari, B. Sarkar, and A. Satrajit. A quantum-classical approach to the molecular dynamics of pyrazine with a realistic model Hamiltonian. *J. Chem. Phys.*, 125:194316, 2006.

[235] I. Yamazaki, T. Murao, T. Yamanaka, and K. Yoshihara. Intramolecular Electronic Relaxation and Photoisomerization Processes in the Isolated Azabenzene Molecules Pyridine, Pyrazine and Pyrimidine. *Faraday Discuss.*, 75:395, 1983.

[236] K. K. Innes, I. G. Ross, and W. R. Moomaw. Electronic states of azabenzenes and azanaphthalenes: A revised and extended critical review. *J. Mol. Struc.*, 132:492, 1988.

[237] J. E. Del Bene, J. D. Watts, and J. Bartlett. Coupled-cluster calculations of the excitation energies of benzene and the azabenzenes. *J. Chem. Phys.*, 106:6051, 1997.

[238] A. Bolovinos, P. Tsekeris, J. Philis, E. Pantos, and G. Andritsopoulos. Absolute Vacuum Ultraviolet Absorption Spectra of Some Gaseous Azabenzenes. *J. Mol. Spec*, 103:240, 1984.

[239] I. C. Walker and M. H. Palmer. The electronic states of the azines. IV. Pyrazine, studied by VUV absorption, near-threshold electron energy-loss spectroscopy and ab initio multi-reference configuration interaction calculations. *Chem. Phys.*, 153: 169, 1991.

[240] P. R. Callis. Electronic States and Luminescence of Nucleic-Acid Systems. *Ann. Rev. Phys. Chem.*, 34:329, 1983.

[241] A. L. Sobolewski, W. Domcke, C. Dedonder-Lardeux, and C. Jouvet. Excited-state hydrogen detachment and hydrogen transfer driven by repulsive $^1\pi\sigma^*$ states: A new paradigm for nonradiative decay in aromatic biomolecules. *Phys. Chem. Chem. Phys.*, 4:1093, 2002.

[242] C. E. Crespo-Hernandez, B. Cohen, P. M. Hare, and B. Kohler. Ultrafast excited-state dynamics in nucleic acids. *Chem. Rev.*, 104:1977, 2004.

[243] C. T. Middleton, K. de La Harpe, C. Su, Y. K. Law, C. E. Crespo-Hernandez, and B. Kohler. DNA Excited-State Dynamics: From Single Bases to the Double Helix. *Ann. Rev. Phys. Chem.*, 60:217, 2009.

[244] L. Serrano-Andrés and M. Merchán. Are the five natural DNA/RNA base monomers a good choice from natural selection? A photochemical perspective. *J. Photochem. Photobiol. C*, 10:21, 2009.

[245] H. Kang, K. T. Lee, B. Jung, Y. J. Ko, and S. K. Kim. Intrinsic lifetimes of the excited state of DNA and RNA bases. *J. Am. Chem. Soc.*, 124:12958, 2002.

[246] E. Samoylova, H. Lippert, S. Ullrich, I. V. Hertel, W. Radloff, and T. Schultz. Dynamics of photoinduced processes in adenine and thymine base pairs. *J. Am. Chem. Soc.*, 127:1782, 2005.

[247] S. Perun, A. L. Sobolewski, and W. Domcke. Ab initio studies on the radiationless decay mechanisms of the lowest excited singlet states of 9H-adenine. *J. Am. Chem. Soc.*, 127:6257, 2005.

[248] S. Perun, A. L. Sobolewski, and W. Domcke. Photostability of 9H-adenine: mechanisms of the radiationless deactivation of the lowest excited singlet states. *Chem. Phys.*, 313:107, 2005.

[249] L. Blancafort, B. Cohen, P. M. Hare, B. Kohler, and M. A. Robb. Singlet Excited-State Dynamics of 5-fluorocytosine and Cytosine: An Experimental and Computational Study. *J. Phys. Chem. A*, 109:4431, 2005.

[250] C. M. Marian. A new pathway for the rapid decay of electronically excited adenine. *J. Chem. Phys.*, 122:104314, 2005.

[251] L. Serrano-Andrés, M. Merchán, and A. C. Borin. Adenine and 2-aminopurine: Paradigms of modern theoretical photochemistry. *Proc. Natl. Acad. Sci. U.S.A.*, 103:8691, 2006.

[252] L. Blancafort. Excited-state potential energy surface for the photophysics of adenine. *J. Am. Chem. Soc.*, 128:210, 2006.

[253] Y. B. Lei, S. A. Yuan, Y. S. Dou, Y. B. Wang, and Z. Y. Wen. Detailed dynamics of the nonradiative deactivation of adenine: A semiclassical dynamics study. *J. Phys. Chem. A*, 112:8497, 2008.

[254] M. Barbatti and H. Lischka. Nonadiabatic Deactivation of 9H-Adenine: A Comprehensive Picture Based on Mixed Quantum-Classical Dynamics. *J. Am. Chem. Soc.*, 130:6831, 2008.

[255] M. G. D. Nix, A. L. Devine, B. Cronin, and M. N. R. Ashfold. Ultraviolet photolysis of adenine: Dissociation via the $^1\pi\sigma^*$ state. *J. Chem. Phys.*, 126:124312, 2007.

[256] B. Cohen, P. M. Hare, and B. Kohler. Ultrafast excited-state dynamics of adenine and monomethylated adenines in solution: Implications for the nonradiative decay mechanism. *J. Am. Chem. Soc.*, 125:13594, 2003.

[257] R. D. Brown, P. D. Godfrey, D. McNaughton, and A. P. Pierlot. A Study of the Major Gas-phase Tautomer of Adenine By Microwave Spectroscopy. *Chem. Phys. Lett.*, 156:61, 1989.

[258] L. B. Clark, G. G. Peschel, and I. Tinoco Jr. Vapor Spectra and Heats of Vaporization of Some Purine and Pyrimidine Bases. *J. Phys. Chem.*, 69:3615, 1965.

[259] B. Mennucci, A. Toniolo, and J. Tomasi. Theoretical study of the photophysics of adenine in solution: Tautomerism, deactivation mechanisms, and comparison with the 2-aminopurine fluorescent isomer. *J. Phys. Chem. A*, 105:4749, 2001.

[260] R. Mitrić, J. Petersen, and V. Bonačić-Koutecký. Laser-field-induced surface-hopping method for the simulation and control of ultrafast photodynamics. *Phys. Rev. A*, 79:053416, 2009.

[261] M. Wohlgemuth, R. Mitrić, and V. Bonačić-Koutecký. TDDFT excited state nonadiabatic dynamics combined with QM/MM approach: Photodynamics of indole in water. *J. Chem. Phys.*, page submitted, 2010.

[262] J. Petersen, R. Mitrić, V. Bonačić-Koutecký, J. P. Wolf, J. Roslund, and H. Rabitz. How Shaped Light Discriminates Nearly Identical Biochromophores. *Phys. Rev. Lett.*, 105:073003, 2010.

# List of Abbreviations

| | |
|---|---|
| ADC | algebraic diagrammatic constructions |
| AIMS | ab initio multiple spawning |
| a. u. | atomic units |
| arb. u. | arbitrary units |
| B3LYP | (Becke, three-parameter, Lee-Yang-Parr) exchange-correlation functional |
| BAN | benzylideneaniline |
| CAS-SCF | complete active space self-consistent field |
| CI | configuration interaction |
| CSF | configuration state function |
| CT | charge-transfer |
| DC | discredited description of the electronic continuum |
| DFT | density functional theory |
| DFTB | density functional tight binding |
| DNA | deoxyribonucleic acid |
| EOM-CC | equation-of-motion coupled cluster |
| EOM-CCSD | equation-of-motion coupled cluster restricted to single and double excitations |
| EOM-CCSD(T) | EOM-CCSD including perturbative contributions of connected triple excitations |
| Eq. | Equation |
| Fig. | Figure |
| FWHM | full width at half maximum |
| fs | femtosecond |
| GGA | general gradient approximation |
| HF | Hartree-Fock |
| HK | Hohenberg-Kohn |
| IC | internal conversion |
| IE | ionization energy |
| KS | Kohn-Sham |
| LSDA | Local Spin Density Approximation |
| LR | linear response |
| LR-TDDFT | linear response time-dependent density functional theory |
| MCTDH | multiconfigurational time-dependent Hartree |
| MD | molecular dynamics |

| | |
|---|---|
| MRCI | multi-reference configuration interaction |
| osc. | oscillator |
| PAD | photoelectron angular distribution |
| PBE | Perdew-Burke-Ernzerhof functional |
| PBE0 | hybrid functional based on Perdew-Burke-Ernzerhof functional |
| PES | potential energy surface |
| PKE | photoelectron kinetic energy |
| ps | picosecond |
| QM | quantum mechanical |
| RI | Resolution-of-the-Identity |
| RPA | random phase approximation |
| SCC | self-consistent charge |
| SI | Stieltjes imaging |
| TDDFT | time-dependent density functional theory |
| TDDFTB | time-dependent density functional theory tight binding |
| TDDVR | time-dependent discrete variable representation |
| TE | transition energy |
| TRPEI | time-resolved photoelectron imaging |
| TRPES | time-resolved photoelectron spectroscopy |
| TSH | Tully's surface hopping |
| TZVP | triple-$\zeta$ valence plus polarization |
| UV | ultraviolet |
| XC | exchange-correlation |
| ZEKE | zero kinetic energy |

# Publikationsliste – Ute Werner

1. U. Werner. Simulation und Analyse zeitaufgelöster NeNePo-Pump-Probe-Spektren von Silberoxidclustern. *Diplomarbeit, Humboldt-Universität zu Berlin,* 2006.
2. V. Bonačić-Koutecký, R. Mitrić, U. Werner, L. Wöste, and R. S. Berry. Ultrafast dynamics in atomic clusters: Analysis and control. *Proc. Natl. Acad. Sci. U.S.A.*, 103:10594, 2006.
3. R. Mitrić, U. Werner, C. Bürgel, and V. Bonačić-Koutecký. Dynamical aspects and the role of IVR for the reactivity of noble metal clusters towards molecular oxygen. *Eur. Phys. J. D*, 43:201, 2007.
4. U. Werner, R. Mitrić, T. Suzuki, and V. Bonačić-Koutecký. Nonadiabatic dynamics within the time dependent density functional theory: Ultrafast photodynamics in pyrazine. *Chem. Phys.*, 349:319, 2008.
5. R. Mitrić, U. Werner, and V. Bonačić-Koutecký. Nonadiabatic dynamics and simulation of time resolved photoelectron spectra within time-dependent density functional theory: Ultrafast photoswitching in benzylideneaniline. *J. Chem. Phys.*, 129:164118, 2008.
6. R. Mitrić, U. Werner, M. Wohlgemuth, G. Seifert, and V. Bonačić-Koutecký. Nonadiabatic dynamics within time-dependent density functional tight binding method. *J. Phys. Chem. A*, 113:12700, 2009.
7. U. Werner, R. Mitrić, and V. Bonačić-Koutecký. Simulation of time resolved photoelectron spectra with Stieltjes imaging illustrated on ultrafast internal conversion in pyrazine. *J. Chem. Phys.*, 132:174301, 2010.
8. T. Fuji, Y.-I. Suzuki, T. Horio, T. Suzuki, R. Mitrić, U. Werner, and V. Bonačić-Koutecký. Ultrafast photodynamics of furan. *J. Chem. Phys.*, 133:234303, 2010.
9. M. Barbatti, J. Pittner, M. Pederzoli, U. Werner, R. Mitrić, V. Bonačić-Koutecký, and H. Lischka. Non-adiabatic dynamics of pyrrole: Dependence of deactivation mechanisms on the excitation energy. *Chem. Phys.*, 375:26, 2010.
10. R. Mitrić, J. Petersen, M. Wohlgemuth, U. Werner, V. Bonačić-Koutecký, L. Wöste, and J. Jortner. Time-resolved femtosecond photoelectron spectroscopy by field-induced surface hopping. *J. Phys. Chem. A*, 115:3755, 2011.

11. R. Mitrić, J. Petersen, M. Wohlgemuth, U. Werner, and V. Bonačić-Koutecký. Field-induced surface hopping method for probing transition state nonadiabatic dynamics of $Ag_3$. *Phys. Chem. Chem. Phys.*, 13:8690, 2011.

12. R. Mitrić, J. Petersen, U. Werner, and V. Bonačić-Koutecký. Theoretical Methods for Nonadiabatic Dynamics "on the fly" in Complex Systems and its Control by Laser Fields. *Prog. Theor. Chem. Phys.*, in press.

# Selbständigkeitserklärung

Hiermit erkläre ich, Ute Werner, die Dissertation selbständig und nur unter Verwendung der angegebenen Hilfen und Hilfsmittel angefertigt zu haben. Ich habe mich anderweitig nicht um einen Doktorgrad beworben und besitze einen entsprechenden Doktorgrad nicht. Ich erkläre die Kenntnisnahme der dem Verfahren zugrunde liegenden Promotionsordnung der Mathematisch-Naturwissenschaftlichen Fakultät I der Humboldt-Universität zu Berlin vom 01. September 2005.

Berlin, 17.05.2011